THE THESIS COMMITTEE FOR HE SUN
CERTIFIES THAT THIS IS THE APPROVED VERSION OF THE FOLLOWING THESIS:

IMPLEMENTATION AND APPLICATION OF FRACTURE DIAGNOSTIC TOOLS: FIBER OPTIC SENSING AND DIAGNOSTIC FRACTURE INJECTION TEST (DFIT)

APPROVED BY
SUPERVISING COMMITTEE:

Supervisor:

Kamy Sepehrnoori

Wei Yu

Implementation and Application of Fracture Diagnostic Tools: Fiber Optic Sensing and Diagnostic Fracture Injection Test (DFIT)

by

HE SUN

THESIS

Presented to the Faculty of the Graduate School of

The University of Texas at Austin

in Partial Fulfillment

of the Requirements

for the Degree of

MASTER OF SCIENCE IN ENGINEERING

THE UNIVERSITY OF TEXAS AT AUSTIN

DECEMBER 2017

Dedication

To my beloved parents

Shiping Sun and **Jifen Wang**

Acknowledgements

I would like to express my deepest gratitude to my supervisor, Dr. Kamy Sepehrnoori. During my master study at The University of Texas at Austin, I have continuously received help from Dr. Sepehrnoori either in academic area or career development. His excellent idea and consistent support in reservoir simulation and numerical method help me achieve a deeper understanding in my area. No word can express my gratefulness for him.

I would like to thank Dr. Wei Yu, from Texas A&M University, for his kind help and strong support in unconventional reservoir simulation area. Through the almost every week discussion with Dr. Yu, I pinpointed the right path to approach my research topic, fracture diagnosis. I would like to thank Dr. Abdoljalil Varavei for technical support in UTCOMP. He is always patient to solve my question in reservoir simulation and PVT calculation. With his instructions and suggestions, I enhance my understanding in my research area.

I would like to thank Yifei Xu for his helpful discussions with me regarding fracture model and programing skills. The technical discussions with him broaden my view of the complex fracture network simulation. I would like to thank Ali Abouie for his technical support in wellbore model. Through the discussions with him, I have a better understanding in wellbore simulation and wellbore-reservoir coupling scheme. I would like to thank Dr. Hamidreza Lashgari for his support in thermal modelling.

I would like to thank my officemates for their help and support: Reza Ganjdenesh, Mahmound Shakiba, Jose Sergio, Wensi Fu, Yuan Zhang, Ruiyue Yang, Wenda Wang,

Xianchao Chen, Zhiming Chen, Xiaojiang Li, Weitong Sun, Youguang Chen, Hector Emilio Barrios Molano.

I express my appreciation to the finical support from the members of Reservoir Simulation Joint Industry Project (RSJIP) at the Center for Petroleum and Geosystems Engineering at The University of Texas at Austin.

Finally, I would like to thank my parents, Shiping Sun, and Jifen Wang, for their endless love, understanding and support. They make it all worthwhile.

Abstract

Implementation and Application of Fracture Diagnostic Tools: Fiber Optic Sensing and Diagnostic Fracture Injection Test (DFIT)

He Sun, M.S.E

The University of Texas at Austin, 2017

Supervisor: Kamy Sepehrnoori

Shale reservoirs have drawn much attention in recent years in the oil and gas industry. Hydraulic fracturing is a key technology to extract the trapped hydrocarbon in the shale reservoirs. The complex hydraulic and natural fracture networks enable large contact area between fracture and low-permeability reservoir to enhance the production. The characterization of complex fracture geometry and evaluation of fracture properties are crucial to the fracturing operation design and fractured reservoir simulation. The main approach to a better understanding of fracture and shale reservoir matrix is fracture diagnosis. There are mainly five fracture diagnostic technologies: Distributed Temperature Sensing (DTS), Distributed Acoustic Sensing (DAS), Diagnostic Fracture Injection Test (DFIT), microseismic, and tracer flow-back test. In this study, we mainly focus on the data interpretation model of DTS and DFIT.

The current interpretation of DTS data is mostly limited to the qualitative analysis. To enable the quantitative interpretation of DTS data, an in-house comprehensive model is developed to evaluate the fracture properties and geometry. Our model couples fracture,

wellbore, and reservoir domain together to capture the full physical process during the production stage. The effects of reservoir parameters, fracture parameters, and fracture geometries on temperature profiling along the wellbore are analyzed with our model. Our forward model could be potentially used to characterize fracture parameters or fracture geometry with history matching.

DFIT is consisted of before closure analysis and after closure analysis. The leak-off coefficient, injection efficiency, reservoir matrix permeability, and initial pore pressure can be obtained from DFIT data analysis. In this study, several models for DFIT data interpretation were integrated. A Marcellus shale gas DFIT data is successfully analyzed with our workflow.

Table of Contents

List of Tables

List of Figures

Chapter 1: Introduction

1.1 Fracture Diagnosis for Unconventional Reservoirs

Unconventional reservoirs, including shale gas, shale oil, and heavy oil, hold a major share in the global oil and gas production. According to U.S. Energy Information Administration (EIA 2013), the technically recoverable shale gas reserves have reached 7299 trillion cubic feet in 2013. The major shale gas resources holders are China, U.S., Argentina, Mexico, and Argentina as shown in **Fig. 1.1**.

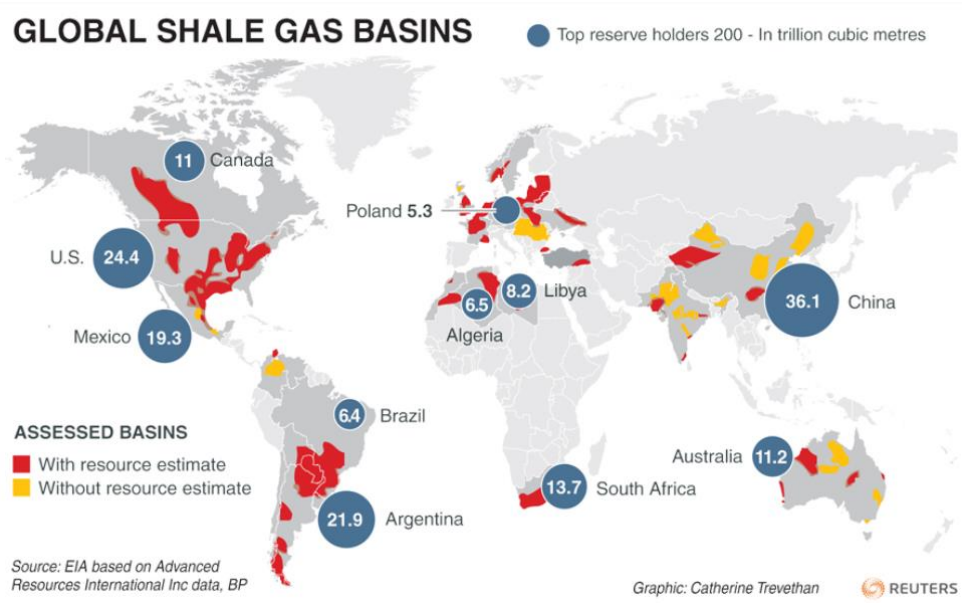

Figure 1.1: Global shale gas reserves distribution in 2012 (EIA 2012).

In U.S, the proved shale gas reserve has 324.3 trillion cubic feet in 2015. More than 30 U.S. states have shale formation. Five states accounted for about 65% total U.S. dry natural gas production in 2016: Texas (24%), Pennsylvania (20%), Oklahoma (9%), Louisiana (6%), and Wyoming (5%) (EIA 2017). The shale gas production from major

shale gas reserves in U.S. between 2003 and 2017 is shown in **Fig. 1.2**. The Marcellus shale gas holds the highest share.

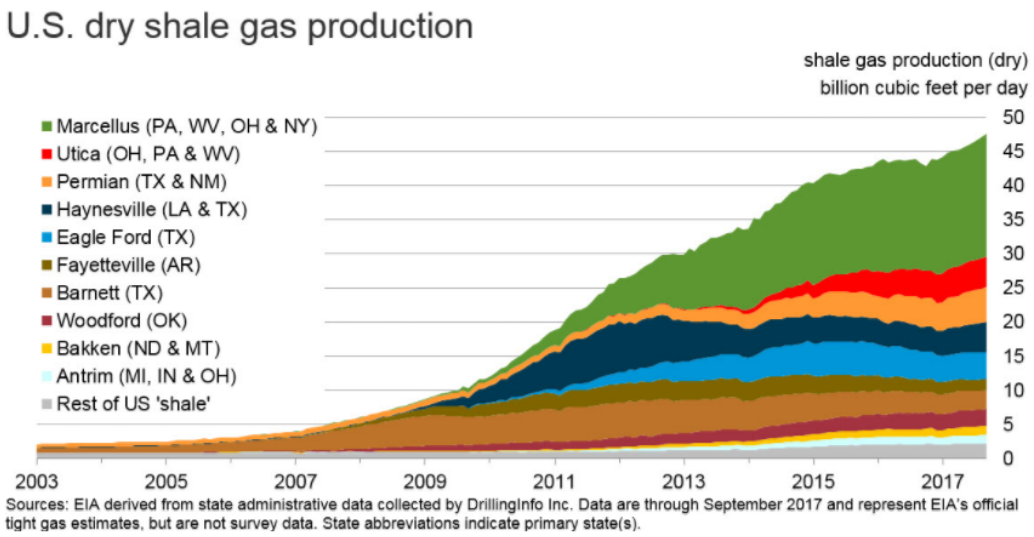

Figure 1.2: U.S dry shale gas production for major shale gas reserves between 2003 and 2017 (EIA 2017).

The key technology for shale gas reservoir is hydraulic fracturing: pressurized fracturing fluid containing water, sand, and other proppants is injected into a wellbore to create cracks in the formation. The high contact area of fracture surface enables high oil and gas production. However, in the field applications, usually 20 percent of fractures contributes to 80 percent of production. Due to the pre-existing natural fractures, the complex fracture network maybe generated during the hydraulic fracturing operations. (Maxwell et al. 2002; Fisher et al. 2004; Cipolla et al. 2010; Cipolla et al 2011) A deeper understanding of fracture geometry and fracture properties may shed light on the fracture design and enhance the fracture performace.

Fracture diagnosis is an enabling tool to characterize the fracture geometry and properties. Generally, fracture diagnosis tools collect the pressure, temperature, and acoustic energy from fractures to diagnose the symptom of fractures. The remedy plan will be made after the diagnosis.

In recent years, many fracture diagnostic tools have been developed including DFIT (diagnostic fracture injection test) (Nolte 1979), DTS (distributed temperature sensing), DAS (distributed acoustic sensing), Microseismic, tracer, and magnetic. These fracture diagnostic tools enhance our understanding in hydraulic fractures. For example, the DFIT can obtain the important fracture deign parameters such as leak-off coefficient, matrix permeability, and injection efficiency (Barree et al. 2009, Barree et al. 2015). Fiber optical sensing can monitor the hydraulic fracturing operation and production stage in real-time. Microseismic can map the complex fracture network (Far et al. 2013).

The deeper understanding of fracture geometry and properties is beneficial to the fracture design such as injection rate and pressure, proppant type, and fracture spacing. Meanwhile, the main method for determining future field development program is reservoir simulation. Reservoir simulation for unconventional reservoirs is challenging since not only the formation characterization but also the fracture characterization is required in comparison with reservoir simulation for conventional reservoirs. Many novel models and methods such as embedded discrete fracture model (EDFM) (Lee et al 2001; Li et al. 2008; Hajibeygi et al. 2011; Xu et al. 2017; Yu et al. 2017) and unstructured grid (Karimi-Fard et al. 2003; Hoteit et al. 2006; Hui et al. 2013) are developed to simulate the complex fracture network and heterogeneous fracture properties. The reasonable fracture properties and geometry estimation is crucial to the accurate production predication and effective field development plan improvement. Therefore, it is important to integrate

different fracture diagnostic tools to improve our understanding in both hydraulic fractures and natural fractures.

Fiber optical sensing has been applied to unconventional reservoirs in recent years. Previously, it is mainly applied to military, city construction, and geophysics. The qualitative study of hydraulic fracturing performance can be successfully conducted with fiber optical sensing. For example, with direct visualization of fiber optical sensing data, we can diagnose which stage contributes to most of the production and other abnormal downhole activity such as leak-off and cross flow. The fiber optical sensing can be further extended to perform the quantitative production profiling and characterize the fracture properties such as conductivity and fracture half-length. There is a demand for a comprehensive model to combine the reservoir, fracture, and wellbore together to conduct an integrated analysis of fiber optical sensing data. With a comprehensive model, the applications of fiber optical sensing can be greatly expanded to fracturing fluid lateral expansion evaluation and fracture geometry characterization.

1.2 Objective of This Research

Based on the problems described above, the objectives of this research are

1. Develop an in-house, multiphase and multi-component numerical simulator for distributed temperature sensing data interpretation. The Joule-Thomson effect needs to be considered in the PVT calculations.
2. Couple the wellbore model, reservoir model, and fracture model together to simulate the full DTS system. The pressure field and temperature field need to be interacted between reservoir domain and wellbore domain. Hence, this DTS

forward model could be potentially used to infer the fracture or reservoir properties through the inverse problem.

3. Several newly developed methods to analyze DFIT data will be introduced. These methods will be integrated together to construct a more general approach for the DFIT data analysis.

1.3 Brief Description of Chapters

In Chapter 2, we present a literature review of several novel fracture diagnostic technologies including DFIT, DTS, DAS, Microseismic, and tracer. The newly developed fracture diagnosis integration approach will be introduced. In Chapter 3, we firstly introduce the composition and mechanism of the fiber optical sensing system. Subsequently, the challenging of interpret fiber optical sensing data is illustrated. A field fiber optical sensing data analysis example is also given. In Chapter 4, we introduce our comprehensive model. The governing equation and solution scheme of wellbore and reservoir model are explained. Several case studies were performed to analyze the impacts of fracture geometry and properties on temperature profiling along the wellbore. In Chapter 5, the general workflow for DFIT data analysis including before closure analysis and after closure analysis. A field DFIT data from Marcellus shale was analyzed with the general workflow.

Chapter 2: Literature Review

The reasonable estimations of the complexity of fracture network and the heterogeneous properties are crucial to the design of the further fracturing operations and field development plan. Different fracture diagnosis technology can enable the evaluation of the different parameters during fracture initiation, fracture propagation, and production stages. In this chapter, the recent detailed developments of fiber optical sensing and diagnostic fracture injection test (DFIT) are first discussed. The novel applications and interpretation model for these two fracture diagnostic tools are explained. Subsequently, an overview of other fracture technology, including microseismic and tracer flow-back test, will be illustrated. Recently, people pay more attention to the integrations of different fracture diagnosis technology to obtain an optimal solution. Several newly developed fracture diagnosis technology integration applications will be explained.

2.1 Fiber Optical Sensing

Fiber optical sensing is mainly applied to capture the downhole temperature, acoustic energy and strain information along the wellbore. The corresponding sensing tools are named as distributed temperature sensing (DTS), distributed acoustic sensing (DAS), distributed strain sensing (DSS). The recent developments of DTS and DAS are introduced in the following sessions.

2.1.1 Distributed Temperature Sensing

Downhole temperature measurement embraces plenty of applications. DTS can be employed to monitor heavy oil thermal recovery such as steam assisted gravity drainage (SAGD) (Wang et al. 2011; Zaini et al 2017), flow assurance (Denniel et al. 2004), acidizing monitoring (Grayson et al. 2015), downhole fluid distribution, and effectiveness

of staged hydraulic fracturing (Sookorasong et al. 2014). In this study, we focus on the application of DTS to deliver a better understanding of formation and hydraulic fractures. The thermal properties of fluids and the flow of paths of fluids contain information of interest to the wellbore, which can be used to locate fractures or fluid entries, identify fluid types, and predict flow rate distribution around the fractures. Hence, fracture geometry could be predicted based upon the interpretation of the changing temperature profile. The mechanism of the DTS technology lies in the relation between temperature distribution and fluid properties. The dominant contribution to the temperature distribution is Joule-Thomson expansion of flowing fluid due to the pressure drawdown. The considerable temperature changes only occur in small vicinity of wellbore. **Fig. 2.1** presents the mechanism of downhole fiber optics to detect temperature and acoustic energy.

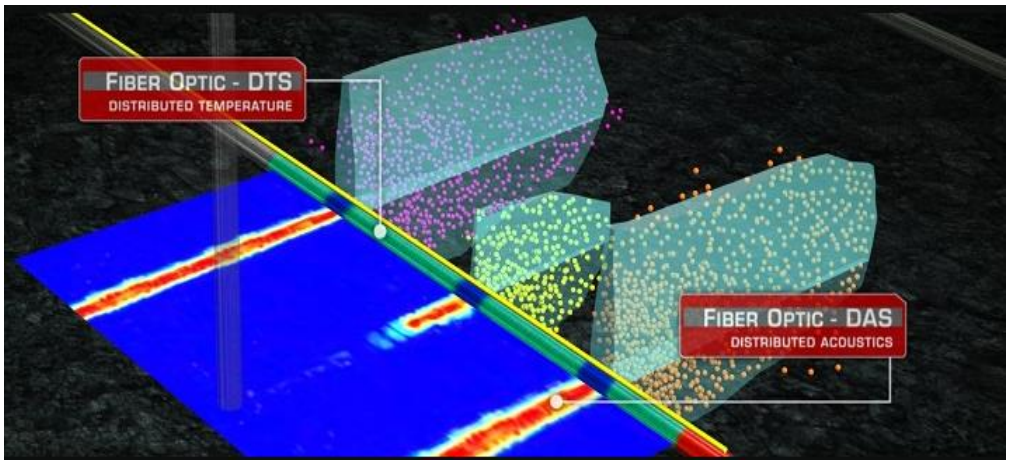

Figure 2.1: Schematic view of DTS and DAS fiber optics deployment.
(http://www.halliburton.com/en-US/ps/pinnacle/fiber-optic-monitoring/default.page)

Significant efforts have been made in DTS in the past. Chen et al. (2008) developed an accurate single-ended (ASE) system to compensate the differential loss caused by the

change of attenuation of the fiber optic. The automatic improvement in accuracy in ASE DTS instrument was verified with laboratory tests and field data. Wang and Bussear (2011) qualitatively analyzed the DTS data during SAGD process to monitor the effectiveness of zonal isolation, pumping fluid movement within the target fracture, integrity of isolation packers, and temperature distribution along the well path. Several suggestions were made that if the further understanding of the formation of steam chamber and its growth with time is required, we should utilize the steam flood simulator to acquire the information. Annulus fluid level around the tubing is an important factor when producing methane hydrate. If the annulus fluid level is high, methane hydrate can be formed inside the tubing due to the low temperature. Sakiyama et al. (2013) dynamically measured the annulus fluid level with the interpretation of DTS data. The DTS analysis model includes the effect of fluid slippage with drift-flux model. Their work enabled the near-real-time monitoring of dynamic fluid levels during production. Foo et al. (2014) measured the injection profile in water flooding with DTS with multiple methods. It is found that with the knowledge of the injection profile, workover is conducted correctly to improve producing water-cut and ultimate recovery. The injection profile should be monitored with time to perform different strategies to improve the water flooding performance. Carbonate formations are commonly stimulated with acidizing treatment to enhance the matrix permeability and remove the near-wellbore damage such as the accumulation of asphaltine. Medina et al. (2015) employed the DTS in a coiled tubing to identify the zones with higher or lower admission and modify the pumping volume and rate of acidizing agents in order to enhance the treatment performance. This workflow was successfully applied to well Bricol 2DL. DTS during the acidizing treatment enables the real-time monitoring and optimization of stimulation operation with the more even distribution of fluid into each interval.

Recently, many DTS simulators have been developed to provide more detailed interpretation of downhole temperature data. Kumar et al. (2012) developed an analytical model to include the frictional heating effect and predicted the downhole temperature during the drilling operation. Steady state solution of heat transfer was presented. The simple analytical model can handle the vertical well and deviated well. The frictional heating caused by wellbore and the rotation of drilling string are captured. With DTS interpretation, the drilling operational parameters are modified to avoid the undesired downhole temperature. Wang et al. (2012) developed a numerical model to simulate the downhole temperature in conventional reservoir. The numerical model coupled the reservoir and wellbore model by iterations method. Slippage in multiphase flow and Joule-Thompson effect are considered in their model. Fluid PVT calculation are performed with Equation of State (EOS). Wavelet transform algorithm is used to de-noise the downhole temperature data. Least square method is employed to perform history matching. With the interpretation of DTS data, formation properties and damaged zone evaluation can be obtained. Cui et al. (2016) developed a semi-analytical model to analyze the DTS data in unconventional reservoirs. The model can handle the single-phase flow with homogenous formation. Operator splitting is employed in the combined solution scheme. With the history matching, fracture half-length and conductivity can be obtained. Furthermore, Fast marching method is used to enhance the computational performance in their model.

2.1.2 Distributed Acoustic Sensing

Distributed acoustic sensing employs the acoustic data from fiber optic to determine which stages are taking most fluid and which stages are taking least fluid and distinguish whether there is leak-off occurring in the hydraulic fracturing process. Injection rate can

also be obtained with the same method. The main mechanism of DAS lies in the relation between the acoustic energy and flow rate. The louder the sound, the higher the flow rate. However, the explicit relationship between them still remains unclear.

Molenaar et al. (2012) conducted the first downhole application of distributed acoustic sensing for hydraulic-fracturing monitoring and diagnostics during the completion of a tight gas well in February 2009. With a combination of the measurement of backscattered light and advanced signal processing, discrimination of which stage is taking most of the fluid and proppant throughout the job can be determined.

Cannon et al. (2013) discussed the DAS's functionality including the factors that influence its frequency response and spatial resolution and the method to calculate the parameters directly. The current valid application of DAS is near well-bore optimization, sand detection, and electric submarine pump (ESP) monitoring.

The previous DAS systems have been limited to qualitative analyses that pinpoint noise sources including injection into formation and production from a fracture. Martinez et al. (2013) employed the signal processing techniques and quantitative analysis to measure the flow rates in a fractured well. Fast Fourier transform is utilized to transform the acoustic signal from the time domain to the frequency domain. As a result, the sound level of the peak frequencies is linearly related to the flow rate. The current DAS system can provide a real-time value for injection rates during hydraulic fracture treatments and values for production rates from post treatment measure.

2.2 Diagnostic Fracture Injection Tests

DFIT, also known as minifrac, is a small pump-in treatment which is popularly employed in characterizing reservoir properties and optimizing the following hydraulic

fracture treatment to be performed. Over 20 years, minifrac has extended its role of characterization of the treatment parameters from conventional fracture treatment to unconventional fracture treatment (Barree et al. 2015). Minifrac involves small pump-in treatment in a short-duration for fracture initiation and subsequent well shut-in, pressure fall off test. With the analysis of the transient pressure behavior, we can obtain the closure pressure, formation permeability, leak-off coefficient, and initial formation pressure (Barree et al. 2009).

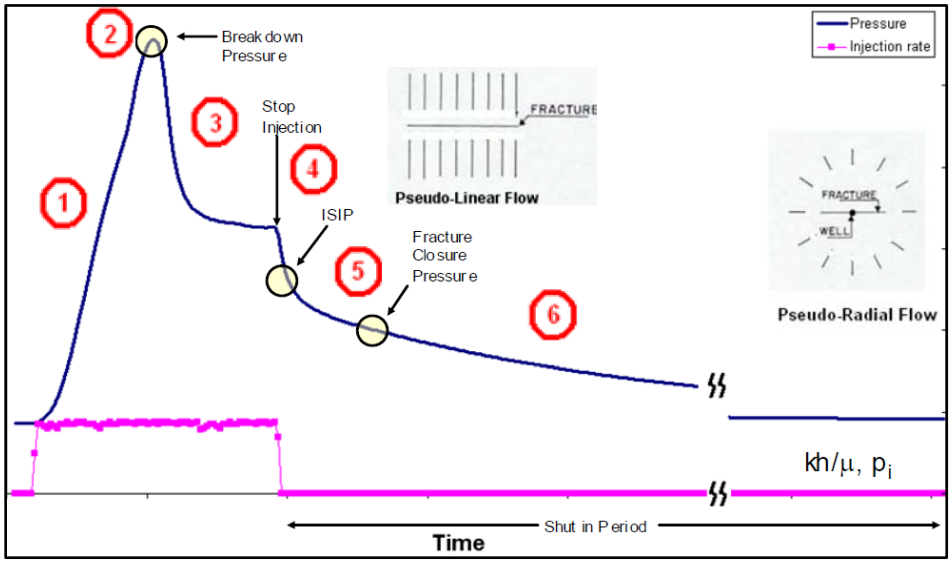

Figure 2.2: Pressure transient behavior during the injection and shut-in stage of DFIT process (Cramer et al. 2013).

The typical DFIT curve is shown in **Fig. 2.2**. The minifrac pressure transient analysis is classified into two major parts, namely, before-closure analysis and after-closure analysis. Different parameters can be inferred from these two analyses. Meanwhile, before-closure analysis and after-closure analysis provide valuable verification for each other.

Based on the PKN fracture geometry model by Perkins and Kern and extended work by Nordgren (Perkins et al. 1961; Nordgren 1979), Nolte (1979) performed several derivations for the fluid loss coefficient, the fracture length and width, fluid efficiency, and closure time for the fracture. Particularly, Nolte derived the G-time function and correlated the G function with pressure and flow rate. With G function, the closure time and closure pressure can be easily distinguished on the plot of pressure and G function. Besides, Nolte presented field applications to verify the feasibility of DFIT. Nolte's original work is primarily based on the before-closure stage and is limited to the PKN model.

In order to generalize the original work, Nolte (1986) extended his analysis to other standard models- the KGD model and penny or radial model. Theoretical relationships for average width, closure time of fracture, leak-off coefficient and fluid efficiency were derived based on the pressure decline after fracturing. Nolte concluded that fluid efficiency can be obtained without assuming a particular fracture model. The theoretical relationships are expressed in terms of upper and lower bound on the rate of fracture growth. The result indicates that either bound can be used within reasonable accuracy.

Nolte (1997) added the DFIT after-closure analysis to the pre-treatment calibration testing sequence from which the fracture geometry, leak-off coefficient and fluid efficiency can be obtained. After-closure includes pseudo-linear flow, transition flow and pseudo-radial flow. These three flow regimes complete the chain of unique characterization features for the fracturing pressure which provides feedback to the validation of prior information. Particularly, the pseudo-linear flow provides the distinct indication of the closure time and pressure, the validation of the fluid-loss analysis by the reservoir analysis and prospect for quantification of spurt-loss. After-closure analysis also sheds light on the characteristics of the fluid-loss behavior.

Without taking the effects of compressibility and temperature change into consideration, the error as much as 75% in the parameter estimation can be produced. Soliman (1986) examined the effects that fluid compressibility and changing temperature have on DFIT with Perkins and Kern, and Christianovich and Zheltov models. The approach is analogous to pseudo pressure in well testing with effective pressure drop. Soliman concluded that with single consideration of compressibility, the magnitude but not the shape of ΔP versus dimensionless time plot changes. The correction for both compressibility and temperature will render the magnitude and the shape of the plot changed. Several examples are conducted to verify the important effect of compressibility and temperature on calculated fluid loss coefficient and fracture length.

Soliman et al. (2005) conducted the extended work on after-closure DFIT analysis. They employed the after-closure stage pressure decline data to determine the formation permeability and reservoir pressure. Based on the transient pressure analysis for the fractured well, Soliman completed the derivation for the quantification of reservoir pressure and formation permeability of each flow regime, namely, linear flow, bilinear flow and radial flow.

Previous works on DFIT interpretation are based on the homogenous formation and an ideal formation-fluid system, which leads to leak-off coefficient is inversely proportionally to square root of time. However, in real cases the formation is heterogeneous. To counteract the impact of heterogeneity in real reservoir conditions, Soliman et al. (1990) defined a new parameter for the time in G function which is called leak-off exponent. They obtained the leak-off exponent by calculating the exponent that produces the least deviation in the plot of pressure and G function. In addition, Soliman took the effect of spurt loss into consideration and concluded that the higher spurt loss is, the shorter the actual closure real time will be.

Conventional fracture pressure decline analysis cannot predict the exponential increase in the leak-off coefficient when treating pressure approaches the maximum horizontal stress. Barree et al. (1996) performed five non-ideal leak-off case studies with numerical simulation (GOHFER simulator). Three pressure function P, $\frac{dP}{dG}$, and $G\frac{dP}{dG}$ are used to uniquely obtain the existence and magnitude of pressure dependent leak-off behavior and eliminate the ambiguity between pressure dependent leak-off, fracture height changes, and tip extension and recession. Also, the effect of pressure dependent fracture compliance was first described.

Later, Barree et al. (1998) conducted extension of work based on previous paper. The field case of G-function and derivative analysis verify that pressure dependent leak-off through secondary fractures exists in many formations. This kind of leak-off can be caused by pre-existing natural fracture or tensile or shear fractures during the fracturing process. The result of derivative analysis can shed light on the prediction of treatment behavior and improvement of fracture design. Barree also stressed the importance of the simulator which can model the pressure dependent leak-off and modules in the real field.

In the later work, Barree et al. (2007) clarified the method of determining parameters such as fracture closure pressure, flow regimes identification. Barree helped avoid the wrong pick of fracture closure point with modified $\sqrt{t}$ analysis. Different flow regimes can be identified using specific slope line on the log-log $\Delta P_{wf} - \Delta t$ plot. Barree et al. (2015) concluded the usual mistakes we made in field application and illustrated how to avoid these mistakes and improve data acquisition and analysis.

The Nolte-Smith (Nolte 1979) method for DFIT data provides highly reliable interpretation of fracturing event. However, in the field applications, this method is limited to long duration to detect a change in fracture behavior, the assumption of continuous

fracture propagation and fixed injection rate, and the requirement of prior knowledge of closure pressure of the formation. Pirayesh et al. (2013) created an innovative numerical procedure to analyze the fracturing pressure using moving-reference-point concept assembled with a mathematical manipulation of the power-law fracture propagation theory. This new method permits quick and accurate interpretation of fracturing data and no need of knowledge of formation in-situ stresses.

Lamei et al. (2014) introduced a new before closure model based on rigorous treatment of the fluid flow equations in the fracture and the formation. This new model requires linear leak-off and short injection time which are generally true in real cases. Fracture stiffness has been taken into consideration in this model. Formation permeability can be obtained with the interpretation of the slope of straight line using before closure data. Lamei also concluded that solutions for linear and radial flow regimes are similar with the neglected skin factor and long-term assumption.

McClure et al. (2014) interpreted the G-function derivative plots with changing fracture compliance during closure. In low permeability formations, it is not necessary to explain the concave up deviation with height recession or transverse storage. The factors contributing to the shape of the after closure curve include fracture height, closure stress and residual aperture percentage. Wellbore storage broadens the post-closure peak. However, in high permeability formations, the effect of fracture compliance becomes less important. In all cases, the most accurate determination for the minimum principal stress is at the deviation form linearity on the $G\frac{dP}{dG}$ plot.

Wang et al. (2017) examined the assumption inherent in the Nolte's original G-function model and presented a new global pressure transient model for pressure decline after shut-in. This model not only preserves the physics of unsteady state flow behavior,

fracture mechanics but also considers the changes of fracture stiffness due to the contact of rough fracture walls during closure. The results also showed that the Carter leak-off model is an over simplification which could lead to noticeable errors in the data interpretation. The pressure dependent leak-off coefficient should be employed. This research also showed that the early and late deviation point in the G-function plot indicates the lower bound and upper bound for the closure point. The average between these two bounds is suggested to use.

2.3 Microseismic Monitoring

Microseismic has been widely used in measuring fracture geometry and fracture propagation especially in unconventional reservoir due to the complete picturing hydraulic fracture growth. Microseismic monitoring provides the detection, location and further analysis of extremely small seismic events induced by the fracturing process. Microseismic data can reveal a comprehensive variation in hydraulic fracture growth from relatively simple planar fractures to very complex fracture networks. **Fig. 2.3** shows the typical microseismic cloud signal. Each dot represents a microseismic event. However, not all microseismic event represents the fracture initiation or fracture propagation. It is crucial for us to develop an effective algorithm to inverse the microseismic signal to map the complex fracture network.

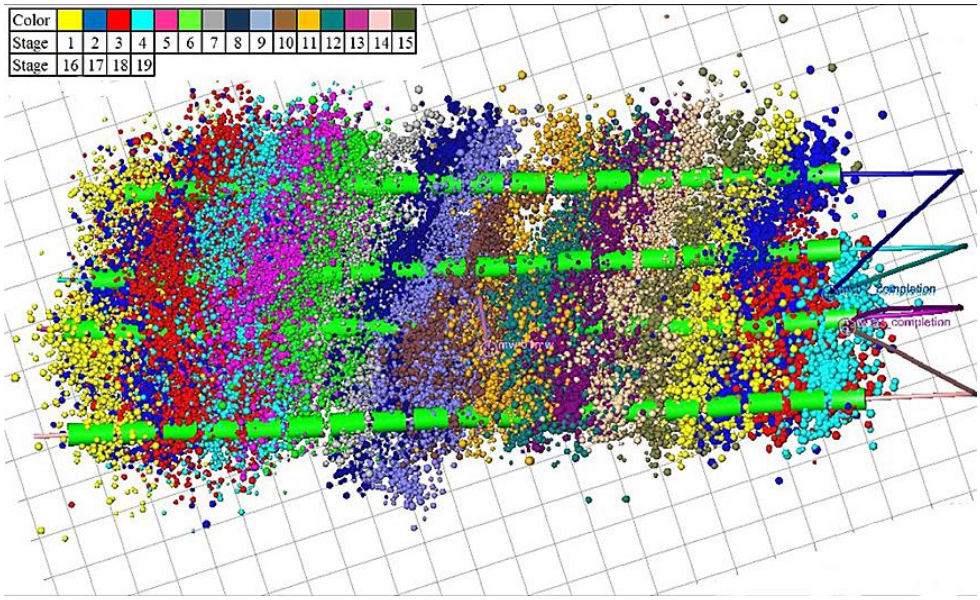

Figure 2.3: The typical microseismic signal in the unconventional reservoir. (https://www.terpconnect.umd.edu/~wjiao/page1.html)

Talebi et al. (1991) analyzed the microseismic data from Inglenook oil field near Kindersley Saskatchewan. With the microseismic signals recorded during the fracturing treatment, the orientation and geometry of the fracture are determined.

Cipolla et al. (2011) illustrated the application of two complex fracture modeling techniques, the semi-analytical model and gridded numerical model, in conjunction with microseismic mapping to characterize fracture complexity and evaluate the performance. Quantification of the impact of changes in fracture design using complex fracture model still remains unclear due to the inherent uncertainties in both the Earth Model and real fracture growth. With more than 50 simulation cases, the following conclusions are obtained: when fracture growth is complex, the minimum level of net pressure maybe dictated by the stress bias. Net pressures may be similar for a wide range of fracture complexity and rock properties. The description of the natural fracture system can largely

influence complex fracture geometry. Fracture complexity may be characterized by integrating microseismic measurements with complex hydraulic fracture models. Proppant transport in complex fracture networks may be restricted to a very limited area.

Maxwell et al. (2011) integrated the microseismic measurement, seismic reservoir characterization and injection data to study the variability in the hydraulic fracture response between horizontal wells in the Montney shale in NE British Columbia. A pre-existing fault usually leaves a relatively large magnitude microseismicity in NE edge. In cases relatively simple planar hydraulic fractures were observed in the expected NE-SW direction, even though the fractures tend to preferentially grow towards the SW in the direction of lower Poisson's ratio. The tendency for the hydraulic fractures to be asymmetric and grow preferentially towards the low Poisson's ratio region is attributed to material property changes and associated lower stresses in these regions.

Previous interpretation is limited to the noise caused by the reactivation of natural fractures or faults, previous hydraulic fracture, stratigraphic boundaries. Liu et al. (2016) developed an optimizing method to better characterize the hydraulic fracture geometry with the Pad Window, the Proppant Window, and the Closure Window. Closure Window includes the events from the end of pumping to shut-in of the current stage. Through the extraction of microseismic events in the Closure Window and the elimination of those events induced by the noises described above, the overlap of different stages is reduced and the accuracy of the inferred fracture geometry and stimulated reservoir volume is increased.

2.4 Tracer Flow-back Test

Tracer technology has been widely used in the petroleum industry since 1950s. Existing tracer techniques are mainly divided into two categories, i.e., inter-well tracer technology (Nelson 1985) and single well tracer technology (Zeng et al. 2010). Inter-well tracer technology is mainly applied to inter-well connectivity test, advantage channel identification and residual saturation monitoring. Single well tracer technology is used to evaluate the remaining oil saturation at first, and then gradually is applied to evaluate diffusion coefficient, etc. Tracer flowback after hydraulic fracturing belongs to single well tracer technology. **Fig 2.4** shows the typical tracer flow-back test procedure and tracer concentration responses. Through the tracer concentration information, the fracture geometry may be inferred.

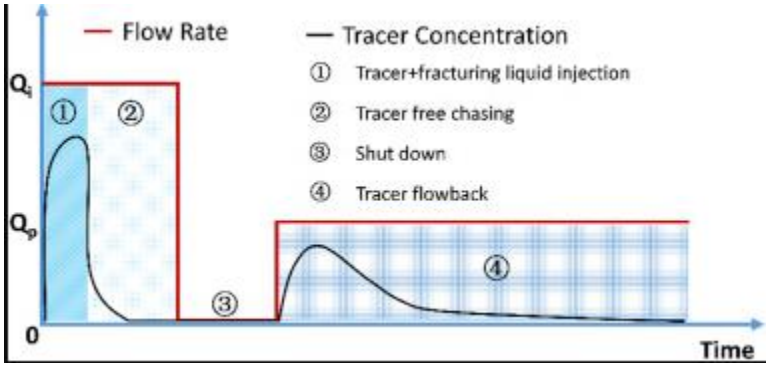

Figure 2.4: Typical tracer flow back concentration response (Li et al. 2017).

Birkholzer and Karasakika (1996) developed software TRIPOLY to simulate the tracer flow and mass transfer phenomenon in the fracture network. Through the combination of TRINET and numerical method, the interaction between fracture and matrix was described

Tsang (2010) conducted single well tracer injection-withdrawal experiments in both simple and complex fractures. Analysis indicates that peak concentration is not sensitive to fracture permeability heterogeneity while it is mainly related to the operation time.

Cotte et al. (2010) modified the single well tracer injection-withdrawal program based on TRIPOLY and studied the influence of matrix porosity, diffusion coefficient, retardation coefficient, fracture aperture, and density on the tracer breakthrough curve. Results show that a larger fracture aperture will result in a weaker tracer diffusion effect on matrix while a longer fracture length will lead to a lower tracer flowback concentration. However, this method does not consider the fracture network generated in multistage horizontal well fracturing.

Ghergut et al. (2014) examined the influence of porosity, permeability, fracture length, height and aperture on tracer breakthrough curves in N-German Basin. Results show that the tailings of tracer signals are highly sensitive to local discharge values; peak concentration exhibits slight ‘acceleration’ and ‘damping’ with increasing matrix porosity or increasing fracture aperture; the effects of matrix and fracture factors are not unambiguously discernible from each other.

2.5 Fracture Diagnosis Tools Integration

In the field application of hydraulic fracturing monitoring and evaluation, the integration of different fracture diagnosis tools is demonstrated recently. If a fracture property can be evaluated by different fracture diagnostic tools, the evaluation of this fracture parameter can be optimized by coupling of these fracture diagnostic tools as shown

in **Fig. 2.5**. Meanwhile, the integration of different fracture diagnostic technology is able to complete the input parameter for each other and deliver a comprehensive fracture characterization.

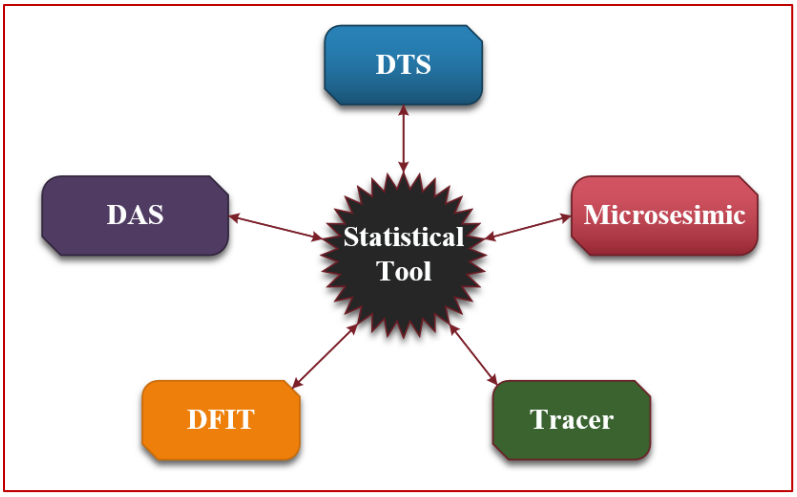

Figure 2.5: Schematic view of comprehensive fracture diagnosis workflow.

Holley et al. (2013) combined the miscroseismic mapping and DTS to diagnose hydraulic fracture network. Microseismic usually fails to capture the near-wellbore fracture and reservoir condition while DTS can only obtain the near-wellbore formation information. The integration of these two methods could deliver a comprehensive real-time hydraulic fracturing operation monitoring and post-fracture interpretation and analysis. Furthermore, these two fracture diagnosis tools are linked with production logging data to obtain an accurate flow rate distribution result.

Haustveit et al. (2017) integrated fiber optic sensing (DTS and DAS), borehole microseismic, electromagnetic imaging, offset well pressure monitoring with IMAGE frac technology, water hammer analysis, and fracture modelling to perform fracturing mapping in Sonner Trend Anadarko Basin Canadian and Kingfisher Counties. A comprehensive

evaluation of cluster efficiency, fluid and sand distribution, fracture half-length, heights, and fracture azimuth is constructed. The agreement between multiple diagnostic tools increased the confidence in the fracture geometry characterization and fracture properties evaluations.

Chapter 3: Overview of Distributed Temperature Sensing

3.1 Mechanism of Distributed Temperature Sensing

Downhole temperature measurement embraces plenty of applications. DTS can be employed to monitor heavy oil thermal recovery such as steam assisted gravity drainage (SAGD), flow assurance, downhole fluid distribution, acidizing efficiency monitoring, and effectiveness of staged hydraulic fracturing.

In this study, we focus on the application of DTS to deliver a better understanding of formation and hydraulic fractures. The thermal properties of fluids and the flow of paths of fluids contain information of interest to the wellbore, which can be used to locate fractures or fluid entries, identify fluid types, and predict flow rate distribution around the fractures. Hence, fracture geometry could be predicted based upon the interpretation of the changing temperature profile. The mechanism of the DTS technology lies in the relation between temperature distribution and fluid properties. The dominant contribution to the temperature distribution is Joule-Thomson expansion of flowing fluid due to the pressure drawdown. The considerable temperature changes only occur in small vicinity of wellbore.

Fig. 3.1 presents the mechanism of the interpretation and signal processing of the light source in the fiber. The hardware of the general fiber optical sensing mainly includes the surface box and downhole optical fiber. A laser-light pulse is sent out continuously from a DTS interrogator in surface box. This light pulse travels at a relatively known speed with a known wavelength (Medina et al. 2015). Subsequently, fiber optic imparts a backscatter effect to the laser light signal.

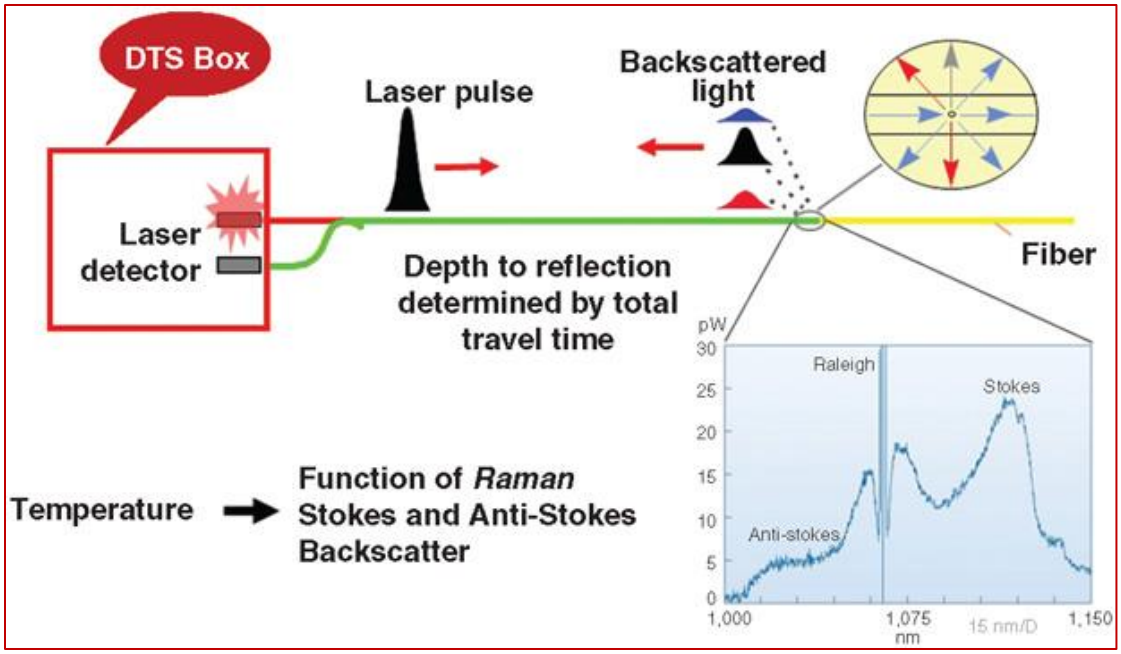

Figure 3.1: Mechanism of temperature sensing from optical fiber signal (Holly et al. 2013).

The backscatter signal contains antistokes and stokes components as shown in **Fig. 3.2.** There are one Rayleigh peak, two Brillouin peaks, and two Raman peaks on the either side of Rayleigh peak. The downhole fluid movement or hydraulic fracturing operations can change the strain of the fiber optics, which affects the shape of the light pulse signal. Consequently, the temperature, acoustic energy, and strain can be inferred with signal processing technique. DTS uses the ratio of two Raman peaks since they are sensitive to temperature. The Brillouin peaks are sensitive to a combination of strain and temperature and so can be used for the Distributed Strain Sensing (DSS) (Dickenson et al. 2016). DAS uses the Rayleigh peak since it is sensitive to dynamic strain, a proxy for vibration in the local environment.

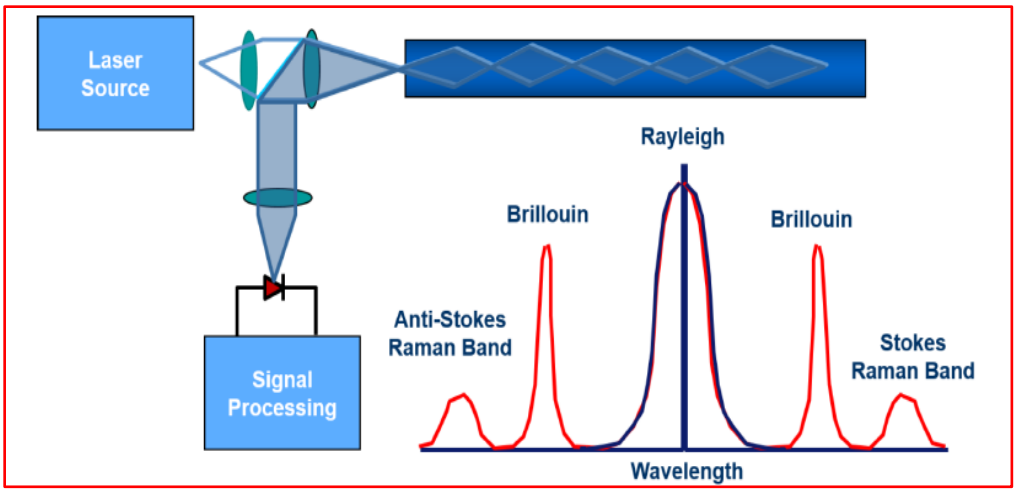

Figure 3.2: Schematic principal of optical time domain reflectometry (Medina et al. 2015).

3.2 Down Fiber Optics Installation

There are three ways to install the fiber optics into the downhole environment, namely temporary installation, semi-permanent installation, and permanent installation. The schematic view of these three installation methods is shown in **Fig. 3.3.**

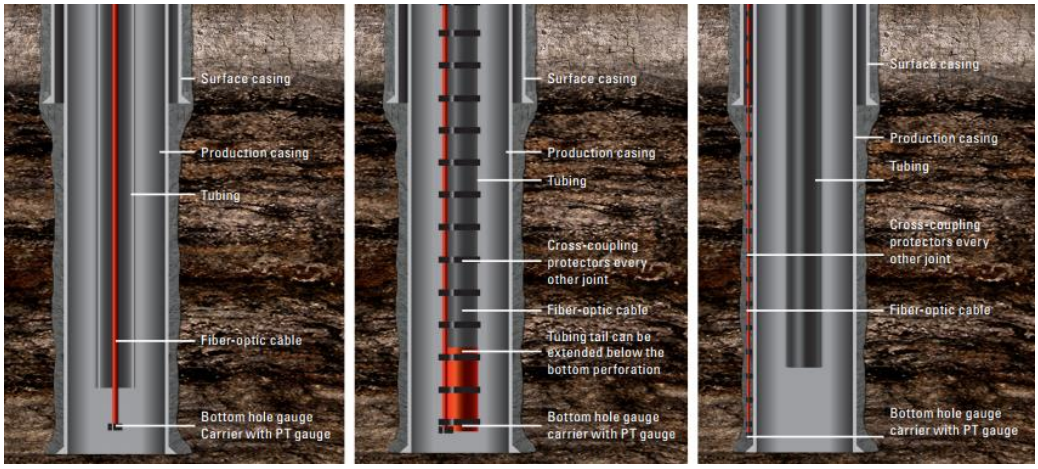

Figure 3.3: Three common fiber optic installation methods (left: temporary installation; middle: semi- permanent installation, right: permanent installation) (Pinnacle fiber optics brochures 2012).

The temporary installation of fiber optics usually comes with coiled tubing or wireline conveyed. The advantage of temporary installation is that the fiber optics can be retrieved at any time. The temperature measured with temporary installation is the fluid temperature inside the wellbore. The semi-permanent installation fiber optics measures the tubing temperature while the permanent installation fiber optics measures the casing temperature.

When it comes to post DTS data interpretation, the temporary installation data is usually easy to deal with since it directly measures the fluid temperature which can be calculated by the wellbore thermal model. However, when simulating the semi-permanent or permanent installation data, the thermal coupling effect should be considered as shown in **Fig. 3.4**. Temperature transient behavior happens in near-wellbore formation which caused the temperature variation at different position inside the cement. The tubing and casing temperature are different from fluid temperature inside wellbore. The post-process is required to infer the tubing temperature and casing temperature which are related to fluid temperature inside the wellbore and formation temperature.

Most of the time, the strong oscillations will be observed in the permanent installation DTS data. There are two contributors accounting for these oscillations, heterogeneous cement thickness and varied fiber optics positions (red line in Fig. 3.4). Both two factors will lead to the different position of fiber optics inside the cement, which causes the temperature oscillation. The heterogeneous cement thickness can be calibrated with the caliper logs. The fiber optics can be pinpoint through optimization tools.

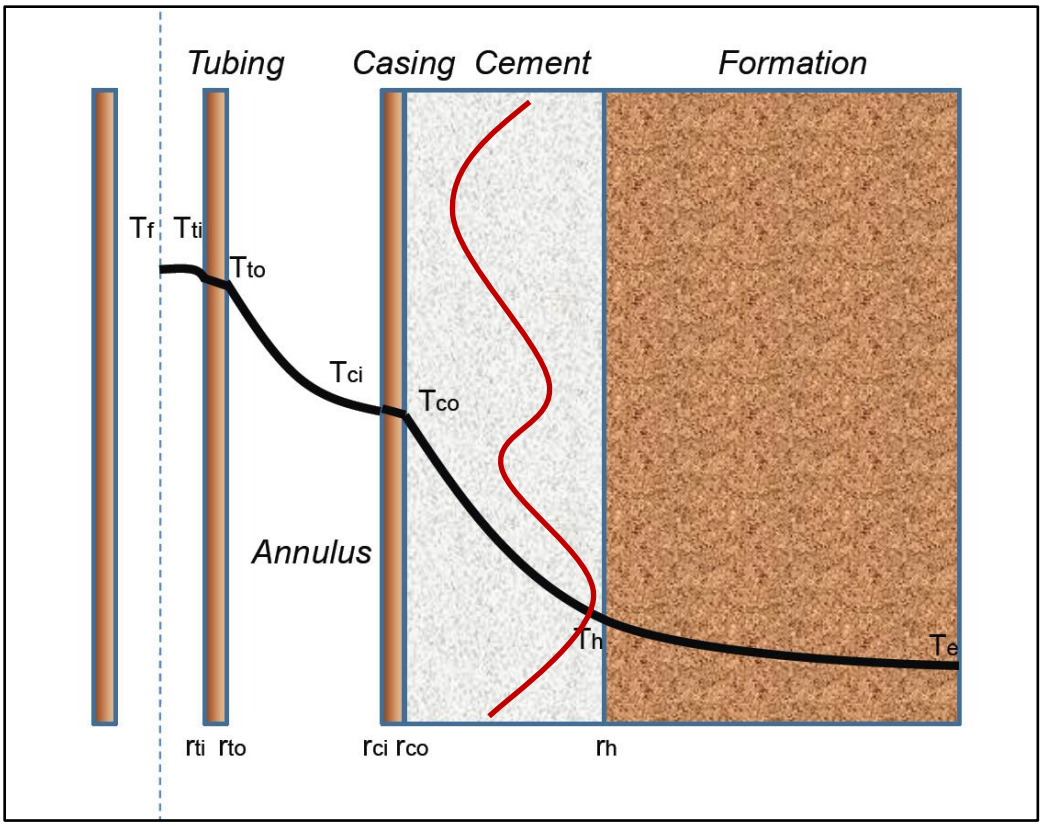

Figure 3.4: The schematic view of thermal coupling effect caused by the fiber optic position variations.

3.3 Applications of DTS

The DTS data interpretation can be classified into qualitative analysis with direct visualization and quantitative interpretation with physical model. The direct visualization mainly focuses on the real-time monitoring of well integrity, sand detection, and multiphase flow. Nowadays, DTS is increasingly applied to the evaluation of the effectiveness of staged fracturing operations. A field DTS data during hydraulic fracturing operations shown in **Fig. 3.5** is employed to illustrate the mechanism of real-time monitoring in shale gas reservoir.

Fig. 3.5 shows the DTS data (upper), DAS data (middle), and injection rate profile (lower) during one stage of hydraulic fracturing operation. The y axial of DTS and DAS data indicates the well depth. In this case, the y axial interval represents one stage of fracturing operation with five clusters marked by the black arrows. The clusters are indexed from 1 to 5 with well depth from top to bottom. The x axial of DTS and DAS data indicates the time domain. The color of DTS and DAS data indicates the temperature and acoustic energy at a certain well depth at a specific time, respectively. The injection rate profile presents the injection rate (thick blue line) with time.

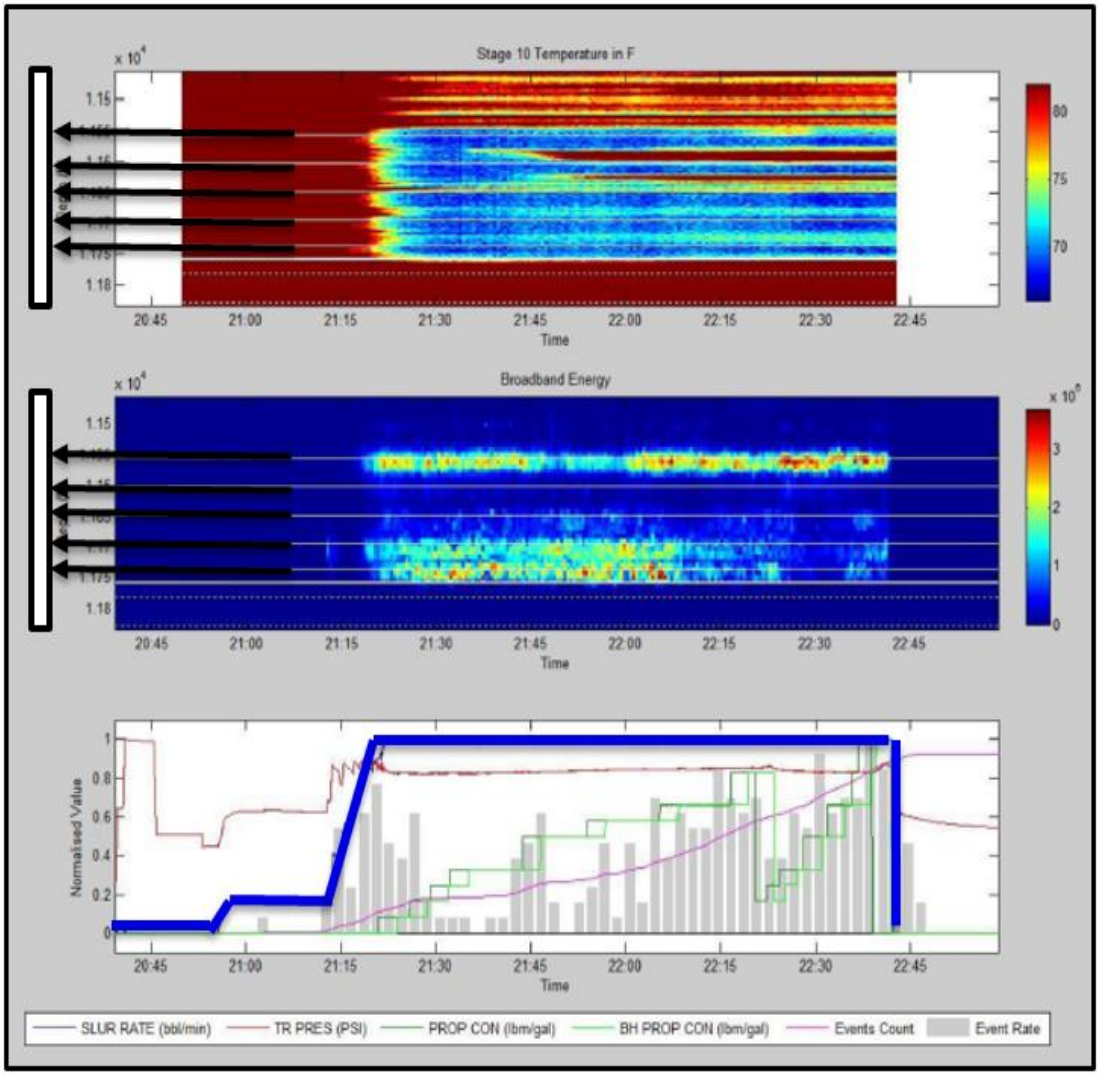

Figure 3.5: Field DTS data qualitative study-one stage fracturing operation with five clusters (Dickenson et al. 2016).

From the injection rate profile, we can clearly see that at around 21:15, there is a fluid injection event indicating the start of a stage of hydraulic fracturing operation. After a short time, the obvious cooling effects (blue color regions) are observed along this stage well interval. The cooling effects are caused by the injected fracturing fluid with lower

temperature. The more obvious cooling effects are, the more fracturing fluid are taken by that perforation. However, the cooling effects of cluster 2 and 3 are disappearing with time, which indicates cluster 2 and 3 did not take much fracturing fluids. Similarly, the acoustic energy of cluster 2 and 3 are almost trivial even at the start of the injection event. The fluids movement will generate acoustic energy. The low acoustic energy is symbol of low fracturing fluids intake. The coincidence between DTS and DAS data analysis increases our confidence in the conclusion of cluster efficiency.

Therefore, DTS and DAS, as doctors, diagnosed the low performance of cluster 2 and 3, as patients. The low performance of cluster 2 and 3 can be contributed by the low fracture conductivity or poor fracture geometry, which is required to further diagnosed with the quantitative interpretation of DTS data. The cure might be the re-fracturing operation of cluster 2 and 3 to extract the potential of cluster 2 and 3.

3.4 Summary

- Major applications of distributed temperature sensing such as steam flooding, flow assurance, acidizing, and downhole fluid distribution monitoring are introduced.
- The mechanism of how fiber optics work is illustrated. The fiber optical sensing signal and how it is related to the temperature, acoustic energy, and strain are explained.
- Three ways, temporary installation, semi-permanent installation, permeant installation of implement fiber optics in the downhole system are illustrated. When dealing with the permanent installation DTS data, the thermal coupling effect should be considered.

- A stage with five clusters of real field DTS data is analyzed. Through the qualitative analysis, the poor performance of cluster 2 and 3 is diagnosed. The good match with DAS data qualitative analysis increases our confidence in our result.

Chapter 4: A Comprehensive Model for DTS Data Interpretation

From the above DTS real-time monitoring analysis, we can already extract much valuable information. However, the DTS qualitative analysis may restrict our understanding of hydraulic fracture only within wellbore domain. But what if we want to know about the exact flowrate coming from each cluster, the fracture properties, and fracture geometry? This time, we need a comprehensive model to handle the wellbore, reservoir, and fracture domain together.

To my knowledge, the current commercial software for DTS data interpretation only considers the wellbore domain. That is to say, there is no way for commercial software to infer any information of reservoir or fracture. To overcome the limitations of the current DTS data interpretation, we constructed an in-house developed comprehensive model for DTS data interpretation.

Our model is a fully numerical model which couples the reservoir, fracture, and wellbore together as shown in **Fig. 4.1**. The pressure and temperature field of reservoir or wellbore domain can be simulated with our comprehensive model. In the following sessions, the detailed feature of our comprehensive model will be discussed.

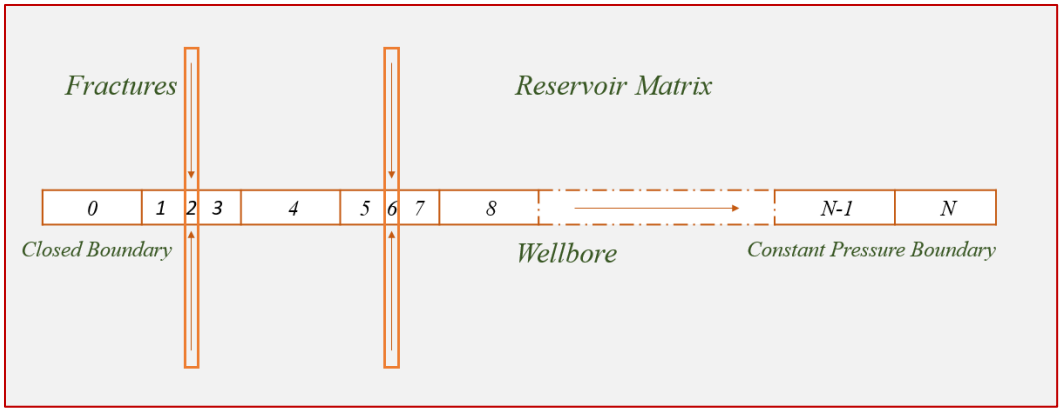

Figure 4.1: Schematic view of the comprehensive system including fracture, reservoir, and wellbore.

4.1 Model Description

4.1.1 Reservoir Model

The reservoir model is a non-isothermal, equation-of-state (EOS) IMPEC (Implicit Pressure and Explicit Compositions) compositional model (Change 1990). The material balance equation is discretized with finite-difference scheme. The general mass conservation equation for each component *i* can be represented as follows:

$$\frac{\partial}{\partial t}\left[\phi\sum_{j=1}^{N_p} S_j \xi_j x_{ij}\right] - \vec{\nabla}\cdot\left[\sum_{j=1}^{N_p} \xi_j x_{ij} \frac{\vec{k}k_{rj}}{\mu_j}\left(\nabla p_j - \gamma_j \nabla D\right)\right] - \frac{q_i}{V_b} = 0, \qquad (4.1)$$

where t is time, ϕ is porosity, N_p denotes the number of phases (our model can handle up to three phases flow), V_b is bulk volume, subscript j refers to fluid phases, S is fluid phase saturation, ξ is molar density, x is mole fraction of component in

phase, $\vec{\vec{k}}$ is permeability tensor, k_r is relative permeability; μ is phase viscosity, D is depth, γ is specific gravity, p is pressure, q is molar injection or production rate (positive for injection, negative for production).

Since the IMPEC solution scheme is employed in our reservoir model, the pressure in each grid block is solved in advance. We assume that the pore volume is filled with the fluid completely and formation rock is slightly compressible:

$$V_t(\mathrm{P},\vec{N}) = V_p(P), \tag{4.2}$$

where V_t denotes total fluid volume, and V_p refers to pore volume. With differentiating both volumes with respect to time and chain rule to expand both terms against their independent variables, the final form of pressure equation is rearranged as follows:

$$\begin{aligned}&\left(V_P^0 c_f - \frac{\partial V_t}{\partial p}\right)\frac{\partial p}{\partial t} - V_b \sum_{i=1}^{N_c+1} \vec{V}_{ti}\vec{\nabla}\cdot\sum_{j=1}^{N_p}\xi_j x_{ij}\frac{\vec{\vec{k}}k_{rj}}{\mu_j}\nabla p \\ &= V_b \sum_{i=1}^{N_c+1}\vec{V}_{ti}\vec{\nabla}\cdot\sum_{j=1}^{N_p}\xi_j x_{ij}\frac{\vec{\vec{k}}k_{rj}}{\mu_j}\left(\nabla p_{cj} - \gamma_j \nabla D\right) + \sum_{i=1}^{N_c+1}\vec{V}_{ti}q_i,\end{aligned} \tag{4.3}$$

where N_c refers to number of hydrocarbon components; V_P^0 is pore volume at reference pressure; p is pressure of reference phase (oleic phase); $\vec{V}_t$ is partial molar volume; p_{cj} is capillary pressure between phase j and reference phase.

The energy conservation equation is expressed in enthalpy formation. By solving the enthalpy of each grid block, the temperature profile of reservoir is obtained. The thermal balance is shown below:

$$V_b \frac{\partial U^T}{\partial t} + V_b \nabla \sum_{j-a,v,o} (\zeta_j h_j \vec{v}_j) - V_b \nabla \cdot (\lambda_T \nabla T) = -\dot{Q}_L + q_H + \dot{H}_r, \qquad (4.4)$$

where U^T is the sum of internal energy of rock and total fluid per bulk volume.

$$U^T = (1-\Phi)\zeta_r u_r + \Phi \sum_{j=a,v,o} \zeta_j S_j u_j, \qquad (4.5)$$

In Eq. 4.4 and Eq. 4.5, λ_T is the effective conductive coefficient, h_j is the phase molar enthalpy, ζ_j is the phase fluid density, ζ_r is the rock density, ϕ is porosity, T is temperature, u_j is the internal energy of phase j, u_r is the internal energy of the rock, S_j is the saturation of the phase j, $\vec{v}_j$ is the phase flux, $\dot{Q}_L$ is the heat loss, q_H is the enthalpy of the injection fluid, $\dot{H}_r$ is the heat of reaction, and the dot in the equation stands for rate. In Eq. 4.4, the first term in the left side is the accumulation term, the second one is the heat convection term, and the third one is the heat conduction term. On the right side of Eq. 4.4, the first term is the heat-loss term, the second one is the source/sink term, and the third one is the heat of reaction term.

At each time step the pressure is solved implicitly with Eq. 4.3 first. Subsequently we calculate the overall number of moles for each component with mass conservation Eq. 4.1. Finally, the temperature is solved implicitly with energy balance equation. During the solution procedure, saturation of each phase can be acquired with flash calculation (Mehra et al. 1983; Perschke et al. 1989) and fluid properties are obtained with Peng-Robinson equation of state (Lohrenz et al. 1964; Peng and Robinson 1976).

4.1.2 Wellbore Model

Our wellbore model is capable of simulating multiphase flow with interphase mass transfer, friction with flow regime detection, and slippage with drift-flux model or two-fluid model (Shirdel 2013). The Equation-of State compositional model and black oil model are employed to update the fluid properties and the equilibrium calculation among all phases. The governing equations for wellbore model includes mass conservation of each phase and each component, momentum conservation of liquid and gas phase, energy conservation of mixture fluid. The finite-difference method is employed to solve the equations.

The mass conservation of the hydrocarbon component in the gas and oil phases is shown as follows:

$$\frac{\partial(\rho_o\alpha_o x_k+\rho_g\alpha_g y_k)}{\partial t}+\frac{1}{A}\frac{\partial(\rho_o\alpha_o u_o x_k+\rho_g\alpha_g u_g y_k)}{\partial x}=\dot{\Psi}_{ok}+\dot{\Psi}_{gk},\quad k=1,...,n_c, \quad (4.6)$$

where ρ_o and ρ_g are the molar density of oil and gas phases, α_o and α_g are the volume fractions of oil and gas, x_k and y_k are the compositions of component k in the oil and gas phases, u_o and u_g are the phases actual velocities and $\dot{\Psi}_{ok}$ and $\dot{\Psi}_{gk}$ are the molar influxes of component k in oil and gas phases. The component based mass conservation equation can be converted to phase based mass conservation as follow:

$$\begin{aligned}\frac{\partial(\rho_o\alpha_o)}{\partial t}+\frac{1}{A}\frac{\partial(A\rho_o\alpha_o u_o)}{\partial x}&=\dot{\Psi}_o-\Gamma_g,\\ \frac{\partial(\rho_g\alpha_g)}{\partial t}+\frac{1}{A}\frac{\partial(A\rho_g\alpha_g u_g)}{\partial x}&=\dot{\Psi}_g+\Gamma_g,\end{aligned} \quad (4.7)$$

where Γ_g is the interphase mass transfer term between oil and gas, $\dot{\Psi}_o$ and $\dot{\Psi}_g$ are oil and gas mass influx terms, and ρ_o and ρ_g are oil and gas mass density.

The mass conservation of water can be expressed as

$$\frac{\partial(\rho_w \alpha_w)}{\partial t} + \frac{1}{A}\frac{\partial(A\rho_w \alpha_w u_w)}{\partial x} = \dot{\Psi}_w, \tag{4.8}$$

where α_w is the water volume fraction, u_w is the water velocity, and $\dot{\Psi}_w$ is the mass influx term which is calculated from productivity indices of reservoir and wellbore.

We employ drift-flux model to describe the multiphase flow slippage in the momentum conservation equation. The drift-flux model proposed by Ishii (1997) is utilized as

$$u_g = C_0 J + V_d, \tag{4.9}$$

where J is volumetric average velocity of the bulk, V_d is the drift velocity and C_0 is the profile parameter.

The momentum conservation with the consideration of slippage can be expressed as follow:

$$\frac{\partial(\rho_m u_m)}{\partial t} + \frac{\partial(\rho_o \alpha_o u_o^2 + (\rho_g \alpha_g u_g^2 + \rho_w \alpha_w u_w^2)}{\partial x} + 144.0 g_c \frac{\partial P}{\partial x} + \rho_m g \sin\theta + \frac{\tau_m \pi D}{A} = 0, \tag{4.10}$$

where $u_m = \frac{\rho_o \alpha_o u_0 + \rho_g \alpha_g u_g + \rho_w \alpha_w u_w}{\rho_m}$, the mixture average velocity is used to calculate each phase velocity.

The velocity of gas, liquid, oil, and water can be expressed as follow:

$$
\begin{aligned}
u_g &= C_1^{gl} u_m + v d_1^{gl}, \\
u_l &= C_2^{gl} u_m + v d_2^{gl}, \\
u_o &= C_1^{ow} u_m + v d_1^{ow}, \\
u_w &= C_2^{ow} u_m + v d_2^{ow}.
\end{aligned} \tag{4.11}
$$

We assume the temperature of gas and liquid are equal. The energy conservation can be obtained as follows:

$$
\begin{aligned}
&\frac{\partial\left[\alpha_o\rho_o(\bar{h}_o+\frac{u_o^2}{2g_cJ_c})\right]}{\partial t}+\frac{\partial\left[\alpha_g\rho_g(\bar{h}_g+\frac{u_g^2}{2g_cJ_c})\right]}{\partial t}+\frac{\partial\left[\alpha_w\rho_w(\bar{h}_w+\frac{u_w^2}{2g_cJ_c})\right]}{\partial t}+\frac{1}{A}\frac{\partial\left[A\alpha_o\rho_o u_o(\bar{h}_o+\frac{u_o^2}{2g_cJ_c})\right]}{\partial x} \\
&+\frac{1}{A}\frac{\partial\left[A\alpha_g\rho_g u_g(\bar{h}_g+\frac{u_g^2}{2g_cJ_c})\right]}{\partial x}+\frac{1}{A}\frac{\partial\left[A\alpha_o\rho_w u_w(\bar{h}_w+\frac{u_w^2}{2g_cJ_c})\right]}{\partial x}-\dot{H}_w-\dot{H}_o-\dot{H}_g+\alpha_w\rho_w\frac{u_w}{g_cJ_c}g\sin\theta+ \\
&\alpha_o\rho_o\frac{u_o}{g_cJ_c}g\sin\theta+\alpha_g\rho_g\frac{u_g}{g_cJ_c}g\sin\theta+\frac{\dot{Q}_{loss}}{A}=0,
\end{aligned} \tag{4.12}
$$

where $\bar{h}_o$, $\bar{h}_g$, $\bar{h}_w$ are oil, gas and water enthalpies per unit mass, g_c and J_c are the unit conversion factors, $\dot{H}_o$, $\dot{H}_g$, and $\dot{H}_w$ are the oil, gas and water enthalpy influxes per unit well grid block volume.

The enthalpy can be calculated with heat capacity and Joule Thompson coefficient:

$$
d\bar{h}_j = C_{pj}dT - (\frac{144}{J_c})\eta_j C_{pj}dP,\ j = o, \mathrm{g}, \mathrm{w}, \tag{4.13}
$$

where C_{pj} and η_j are heat capacity and Joule Thompson coefficient of each phase *j*.

4.1.3 Flow Regime for Horizontal Well

In our horizontal wellbore model, the flow regime is mainly classified into four flow configurations, namely, stratified, bubbly, intermittent, and annular flows as shown in **Fig. 4.2**

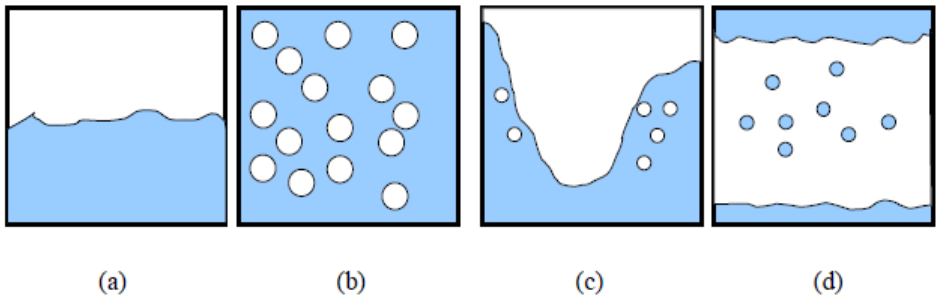

Figure 4.2: Four flow regime of horizontal well (a: stratified, b: bubbly, c: intermittent, c: annular) (Shirdel 2013).

The horizontal flow regime detection algorithm in our model follows Shoham's method (Shoham 2005). The stratified flow regime is first tested with our method with Kelvin-Helmholtz constraint. When the gas velocity exceeds a critical velocity, the flow regime will no longer be stratified flow regime. The flow regime is stratified when the dimensionless parameter fulfills:

$$F_0 < F\,, \tag{4.14}$$

where

$$F = \left(\frac{(1-h_l)^2 A_g}{u_g^2 S_i} \right)^{0.5}, \tag{4.15}$$

$$F_0 = u_{sg}\left(\frac{\rho_g}{Dg\cos\theta(\rho_l - \rho_g)}\right)^{0.5}. \quad (4.16)$$

where u_{sg} is superficial velocity for gas, D is wellbore diameter,

To solve this transition criteria, it is crucial to calculate since other parameters can be calculated with h_l. h_l can be calculated with momentum equations of liquid and gas in stratified regime without axial holdup gradient and momentum acceleration terms.

When h_l fulfills the criteria in Eq. 4.14. the system has stratified flow; otherwise, the system has non-stratified flow. If the flow regime is non-stratified flow and the dimensionless liquid level is less than 0.35, system flow regime is detected as bubbly flow, otherwise, the intermittent flow or annular flow would be testified with the following constrain:

$$T_0 < T, \quad (4.17)$$

where

$$T = \left(\frac{8A_g}{u_l^2 S_i (u_l d_l)^{-0.2}}\right)^{0.5}, \quad (4.18)$$

$$T_0 = \left(\frac{-(dP/dl)_{SL}}{g\cos\theta(\rho_l - \rho_g)}\right)^{0.5}. \quad (4.19)$$

If the criteria in Eq. 4.17 is satisfied, the system has intermittent flow; otherwise, the flow regime is annular flow. The final flow regime detection diagram is shown in **Fig. 4.3**.

The holdup and pressure gradient can be calculated according to the system flow regime. The discontinuity between different flow regime usually causes the convergence

problem. Therefore, the transition criteria are slightly modified with RELAP5 (RELAP 2012) to achieve a stable system.

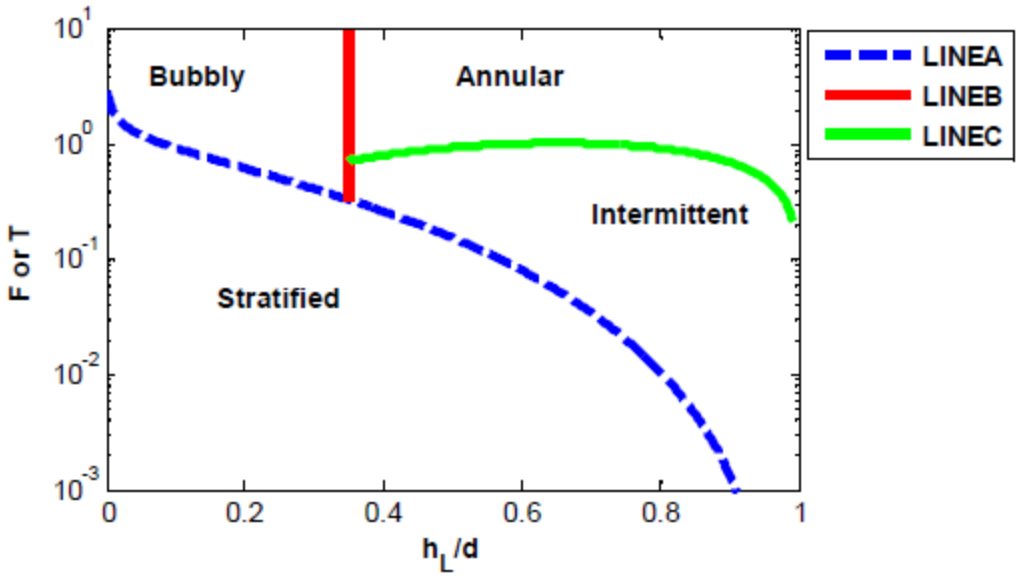

Figure 4.3: Flow regime detection diagram in horizontal well (Shirdel 2013).

4.1.4 Joule-Thomson Effect

In thermodynamics, the Joule-Thomson (JT) effect describes the temperature change of a real gas or liquid when it is forced through a valve or porous plug while kept insulated so that no heat is exchanged with environment (Perry and Green 1984, Roy 2002, Edmister and Lee 1984). JT effects is crucial to DTS since it builds a relation between temperature drop and pressure drop. Based on the pressure drop, the flow rate can be inferred with our model.

JT process happens with constant specific enthalpy. Assume that a certain amount of real gas with initial pressure P_1, temperature T_1, and volume V_1, was forced to go through a valve. There is no heat transfer between valve and surrounding environment. The real gas comes out with pressure P_2, temperature T_2, and volume V_2. The enthalpy change can be expressed as:

$$\Delta H = \Delta U + \Delta(PV). \tag{4.20}$$

Since there is no heat transfer between valve system and surrounding environment, $q = 0$ in the internal energy calculation:

$$\Delta U = q + w = P_1V_1 - P_2V_2 = -\Delta(PV). \tag{4.21}$$

Therefore, JT process is a constant enthalpy process.

JT effect can be quantified with JT coefficient μ_{JT}. JT coefficient is related to the pressure, temperature, and the physical property of the specific fluid. **Fig. 4.4** shows the JT diagram for Nitrogen. The positive JT coefficient indicates the cooling effect while the negative JT coefficient indicates the warming effect. The phase status of nitrogen may vary with pressure and temperature. Generally, gas phases will experience JT cooling effect while liquid phase will experience JT warming effect.

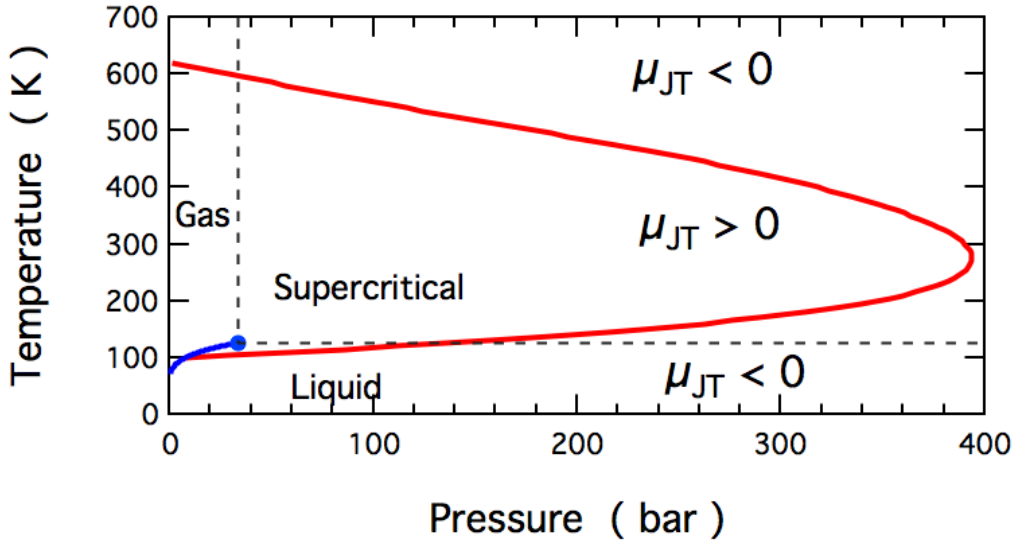

Figure 4.4 The Joule Thomson coefficient diagram of Nitrogen (Webbook Chemistry).

JT coefficient is the gradient of temperature with respect to pressure:

$$\mu_{JT} = -(\frac{\partial P}{\partial T})_H = -\frac{\left(\frac{\partial H}{\partial P}\right)_T}{\left(\frac{\partial H}{\partial T}\right)_P} = -\frac{\left(\frac{\partial H}{\partial P}\right)_T}{C_p}, \tag{4.22}$$

where C_p is heat capacity at constant pressure.

$$\left(\frac{\partial H}{\partial P}\right)_T = T\left(\frac{\partial S}{\partial P}\right)_T + V, \tag{4.23}$$

where S is entropy.

$$\left(\frac{\partial S}{\partial P}\right)_T = -\left(\frac{\partial V}{\partial T}\right)_P . \tag{4.24}$$

Therefore, the JT coefficient can be rewritten as:

$$\mu_{JT} = \frac{T\left(\frac{\partial V}{\partial T}\right)_P - V}{C_P} . \tag{4.25}$$

The term $\left(\frac{\partial V}{\partial T}\right)_P$ is calculated based on the equation of state that we choose.

JT coefficient is calculated with the temperature and pressure before the the JT process. The sign of JT coefficient could change during the process depended on the pressure and temperature. **Fig. 4.5** shows the several fluids JT coefficient at atmosphere pressure with different temperature. At certain temperature, the sign of JT coefficient becomes negative. Meanwhile different fluid has different inversion temperature.

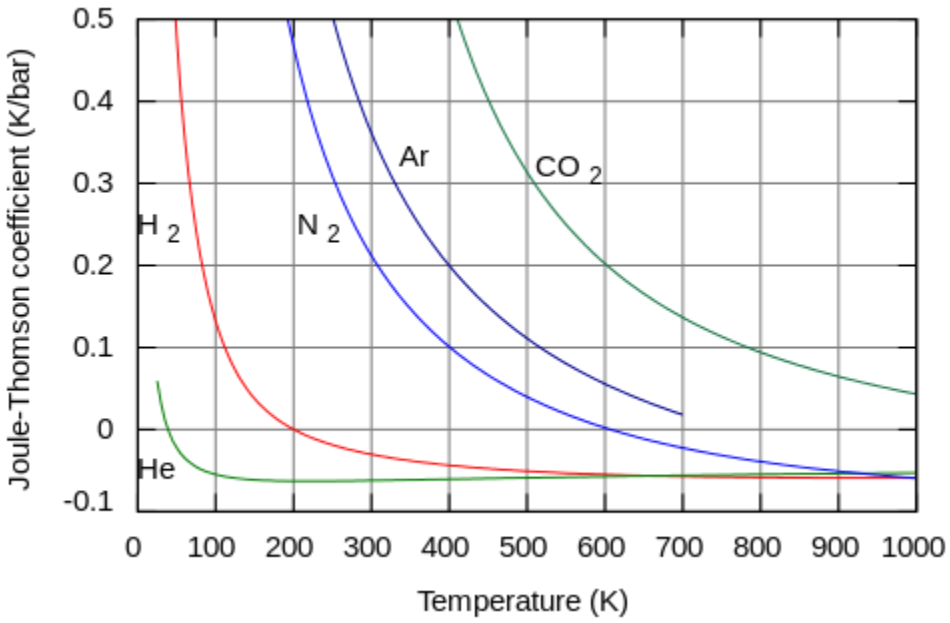

Figure 4.5: Joule Thomson coefficient diagram at various temperature for different gas fluid (Zemansky 1968).

4.1.5 Wellbore-Reservoir Coupling Scheme

In our comprehensive model, the transient pressure and temperature distribution are coupled together between wellbore and reservoir. The reservoir pressure field is solved using IMPEC scheme while the wellbore pressure field is solved using fully implicit scheme. The coupling scheme is mainly divided to two major parts, the pressure coupling and temperature coupling. The detailed the coupling scheme is shown in **Fig. 4.6.**

Firstly, the comprehensive model is initialized with the original input data. The reservoir pressure field including fractures and matrix is solved with the initial wellbore pressure. The solution provides the reservoir fluid pressure and productivity index as

boundary conditions for the wellbore pressure field. Subsequently, the wellbore pressure field is solved, which provides flowing bottom-hole pressure for reservoir field. Now the updated reservoir fluid pressure and flowing bottom-hole pressure are obtained. The convergence of old and updated pressure is checked. If the updated pressure fulfills the convergence criteria, the calculation will move on to temperature coupling. If not converged, the pressure field calculation will be iterated until the required convergence is satisfied. After the pressure field is coupled through iteration method between wellbore and reservoir, the temperature distribution in reservoir domain is solved. The reservoir temperature field provides the ambient temperature and reservoir fluid temperature at perforation for the wellbore temperature model. Finally, the wellbore temperature distribution is obtained with the boundary condition by reservoir temperature model. During the whole process, both reservoir model and wellbore model are solved numerically.

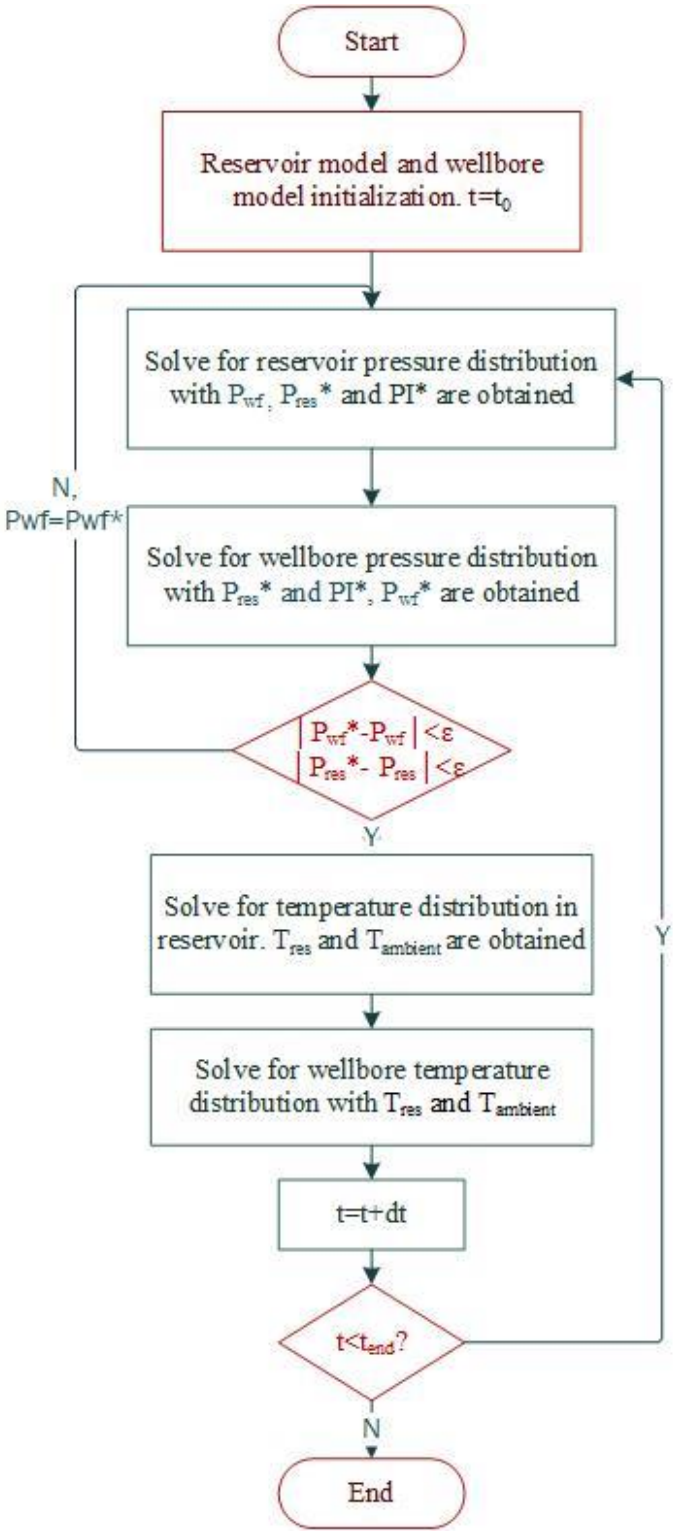

Figure 4.6: Coupling scheme between reservoir model and wellbore model.

4.2 Model Verification

In this session, the reservoir model and wellbore model are verified with commercial software CMG and OLGA respectively.

4.2.1 Model Verification of Transient Wellbore Model

A case with two-phase flow of water and gas is selected to benchmark our wellbore model with commercial transient wellbore simulator OLGA (Bendiksen et al. 1991, Shirdel 2013). The pressure and temperature are compared at the end of the simulation time. The input data for the benchmark case is shown in Tables 4.1 and 4.2. **Fig. 4.7** compares the simulation results of pressure and temperature between our transient wellbore model and OLGA simulator. It can be seen that a reasonable match is obtained.

Wellbore Parameters	**Value**	
Well MD	5000	ft
Well TVD	5000	ft
Max grid size	50	ft
Ambient temperature at top	71	°F
Ambient temperature at bottom	141	°F
Total heat transfer coefficient	0.5	Btu/ft²-hr-°F
Tubing ID	0.25	ft
Water mass injection	1	lb/sec
Gas mass injection	1	lb/sec
Wellhead pressure	500	psi

Table 4.1: Wellbore parameters for the wellbore model verification case.

Fluid Parameters	Value	
Gas specific gravity	0.7	
Water specific gravity	0.98	
Gas heat capacity	0.55	Btu/ft²-hr-°F
Water heat capacity	1	Btu/ft²-hr-°F

Table 4.2: Fluid parameters for the wellbore model verification case.

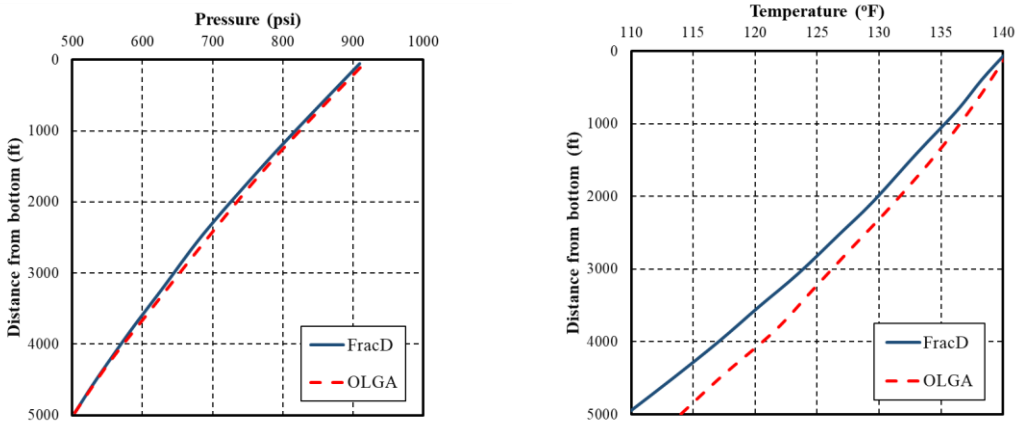

Figure 4.7: Pressure and temperature result comparison with software OLGA.

4.2.2 Model Verification of Reservoir Model

Next, a hot-water injection case with three-phase flow is designed to verify our reservoir model with GEM module of CMG simulator (GEM 2011, Darabi 2014). The components of oil phase are C1 and C20. Initial temperature and pressure of the reservoir are 120 °F and 1500 psi, respectively. Hot water is injected into the reservoir with a constant pressure of 2200 psi and temperature of 180 °F. The detailed input parameters are shown in the Tables 4.3 and 4.4. **Fig. 4.8** (c) compares oil flow rate profile between our reservoir model and CMG. Figs. 4.8 (a), (b), and (d) compare the temperature, pressure,

and water saturation profile with time of top-left grid block between our reservoir model and CMG. The results show a good agreement with CMG is achieved.

Parameters	**Value**	
Number of grid blocks (x×y×z)	50×50×1	
Grid-block size	20×20×20	ft^3
Reservoir temperature	120	°F
Injection temperature	180	°F
Water viscosity	1	cp
Water density	62.4	lb/ ft^3
Reservoir rock thermal conductivity	67.2	Btu/(ft^2-day-°R)
Reservoir rock density	171.36	lb/ ft^3
Reservoir rock heat capacity	0.18	Btu/(lb-°R)
Porosity	0.3	
Horizontal permeability	100	md
Vertical permeability	10	md
Initial water saturation	0.3	
Initial reservoir pressure	1500	psi
Bottom-hole injector pressure	2200	psi
Bottom-hole producer pressure	1500	psi
C_1 composition	0.1	
C_{20} composition	0.9	

Table 4.3: Input parameters for our reservoir model verification case.

	Water	**Oil**	**Gas**
Residual saturation	0	0	0
End point	1	1	1
Exponent	2	2	2

Table 4.4: Relative permeability parameters for our reservoir model verification.

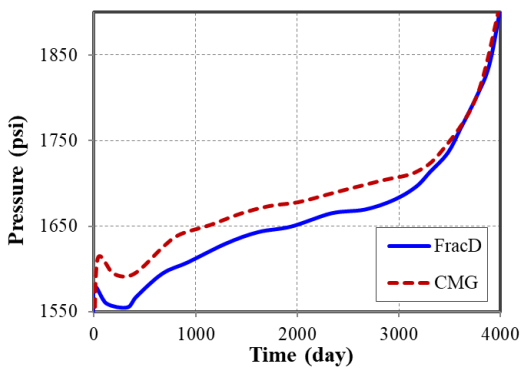

(a) Pressure Comparison

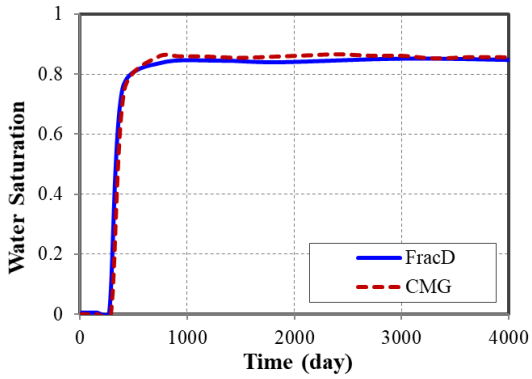

(b) Temperature Comparison

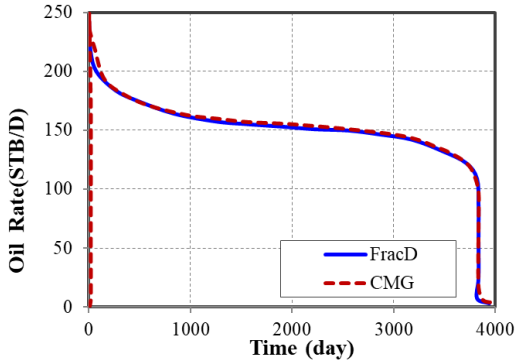

(c) Oil Rate Comparison

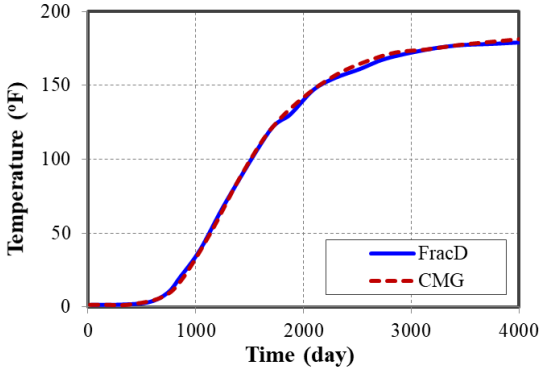

(d) Water Saturation Comparison

Figure 4.8: Comparisons of simulated pressure, temperature, oil rate, and water saturation between our model and a commercial simulator.

4.3 Case Study

In this section, we discuss the thermal behavior during the production period of single fracture and a reservoir with five fractures. For the single fracture case study, the impacts of several parameters including fracture conductivity (fracture permeability multiplied by fracture width), matrix permeability, rock thermal conductivity, and heat

transfer coefficient on temperature profiling along the wellbore are analyzed. As for the five fractures case, the equal-spaced symmetric fractures with equal conductivity and half-length are discussed. Finally, the unequal-spaced asymmetric fractures with unequal conductivity and half-length case are solved and discussed.

4.3.1 Single Fracture Study

4.3.1.1 Single Gas Phase Base Case

To begin with, we set up a base case for the sensitivity analysis. The base case is a single symmetric fracture with homogenous low matrix permeability reservoir matrix. The entire fracture domain is 1302×1525×99 ft. A single fracture is located at the center of the reservoir with 0.02 ft width and 365 ft half-length. There is a horizontal wellbore with 300 ft length connected to the fracture. The schematic view of the fracture geometry, wellbore, and reservoir domain is shown in **Fig. 4.9**. The blue line refers to wellbore while red area represents the fracture.

Since the finite-difference method is employed to solve the governing equation, the reservoir and wellbore grid discretization around the fracture is crucial to the numerical stability and result accuracy. In the following cases, we use the global grid refinement to obtain an accurate estimation for the pressure and temperature profile in wellbore and reservoir domain. The global grid refinement for the base case is shown in Fig. 4.9.

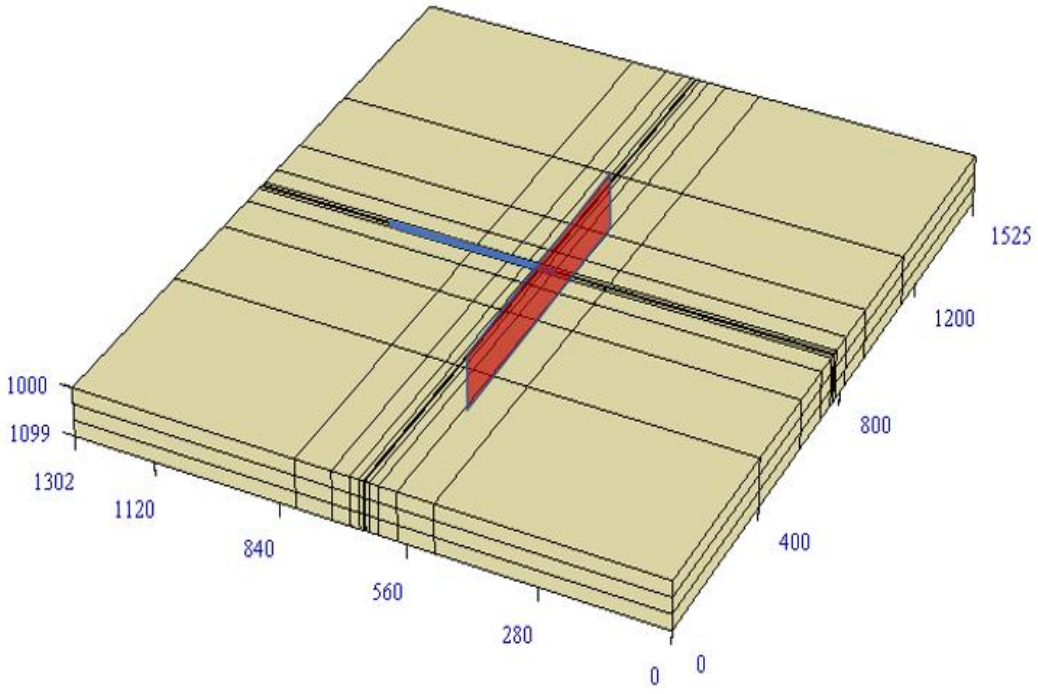

Figure 4.9: Schematic view of fracture geometry and numerical discretization

In the base case, we set the producing pressure of 2000 psi at the wellbore heel. The reservoir contains single component hydrocarbon phase, methane, with initial pressure of 4000 psi and temperature of 250 °F. The initial water saturation is near the irreducible water saturation. Therefore, the water productivity is extremely low. The flow regime during the production is stratified flow. The detailed input parameters for the reservoir and wellbore, composition model calculation, and thermal properties are shown in Tables 4.5-4.8.

Reservoir Parameters	Value	
Reservoir domain	1500*1300*100	ft
Hydrocarbon component	Methane	
Fracture half-length	365	ft
Fracture width	0.02	ft
Fracture height	100	ft
Reservoir permeability	0.1	mD
Fracture conductivity	40	mD
Initial reservoir temperature	250	°F
Initial reservoir pressure	4000	psi
Initial water saturation	0.2	
Reservoir porosity	0.1	
Total compressibility	5×10^{-4}	psi^{-1}
Rock conductivity	67.2	Btu/day-ft-°F
Rock heat capacity	0.18	Btu/lb-°F

Table 4.5: Input parameters for the reservoir in base single fracture case.

Wellbore Parameters	Value	
Wellbore radius	0.1145	ft
Wellbore length	300	ft
Heat transfer coefficient	5.0	Btu/hr-°F
Wellbore inclination	0	°
Roughness	0.0008	
Constant pressure	2000	psi

Table 4.6: Input parameters for the wellbore in base single fracture case.

Critical pressure (atm)	Critical temperature (K)	Critical volume (L/mol)	Molar weight (g/gmol)	Acentric factor	Parachor coefficient
45.4	190.6	0.099	16.043	0.008	77

Table 4.7: Methane PVT Properties.

H_a	H_b	H_c	H_d	H_e	H_f
-2.83857	0.538285	-0.000211409	3.39276×10^{-7}	-1.164322×10^{-10}	1.389612×10^{-14}

Table 4.8: Methane Thermal Properties.

In most situations, the time range for DTS data acquisition is from hours to months. In this study, since our model is solved fully implicitly which enables the capture of fast change in early time, we mainly focus on the early transient period. Therefore, the simulation time for all cases is set to one day.

Fig. 4.10 (a) shows the gas flow rate change with time along the wellbore. The flow rate decreases rapidly within a short time because of the quick pressure depletion in the reservoir. As the result shows, the flow rate becomes half of the initial value over 1 day. Fig. 4.10 (b) shows cumulative gas production from reservoir model of the base case. The dash line describes the early time production gradient. The production gradient is proportional to the flow rate. The increasing deviation from the dash line over time indicates the decreasing flow rate, which confirms our previous flow rate analysis. Fig. 4.10 (c) presents the pressure profile change along the wellbore with time. Since this is a horizontal well, there is no pressure gradient caused by the gravity. The only factor that controls the pressure profile is friction. This well is a merely single gas phase producer. The friction factor calculated with the flow regime is small. The pressure change along the wellbore is only within around 1 psi. Even though the flow rate decreases dramatically, its influence on pressure profile is neglectable due to the low friction factor.

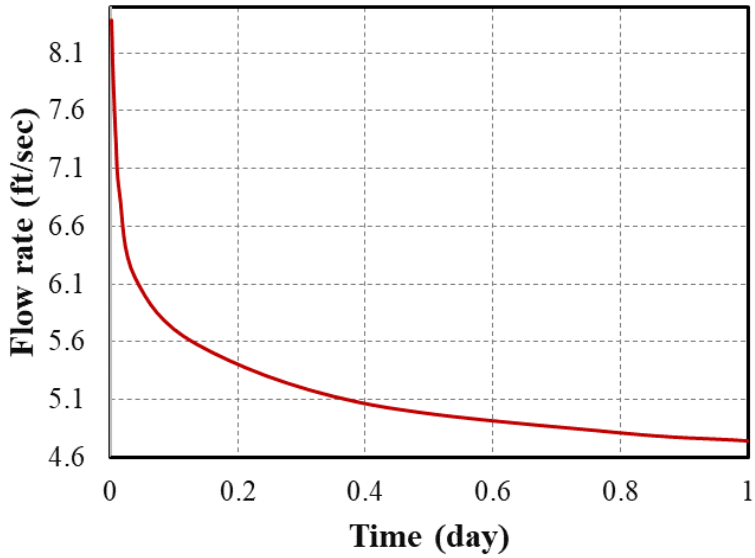

(a) Flow rate

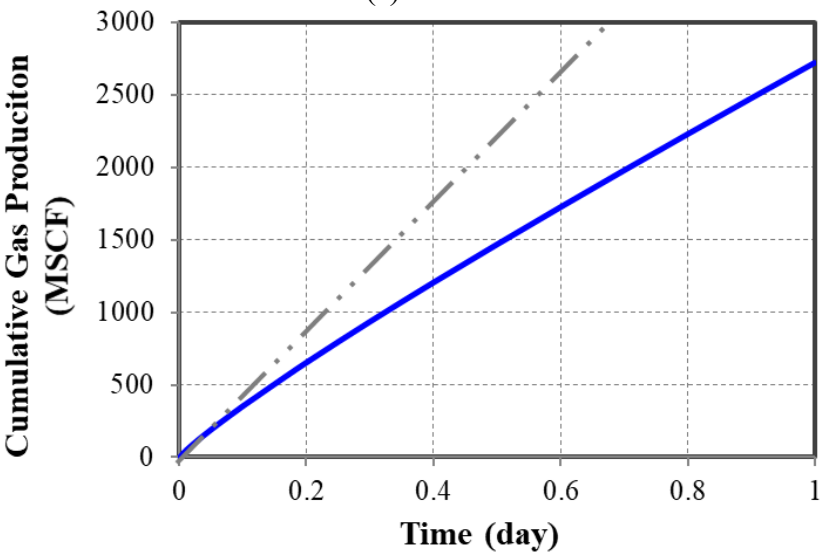

(b) Gas Production

Figure 4.10: Simulation results of flow rate, gas accumulative production, and pressure for base case.

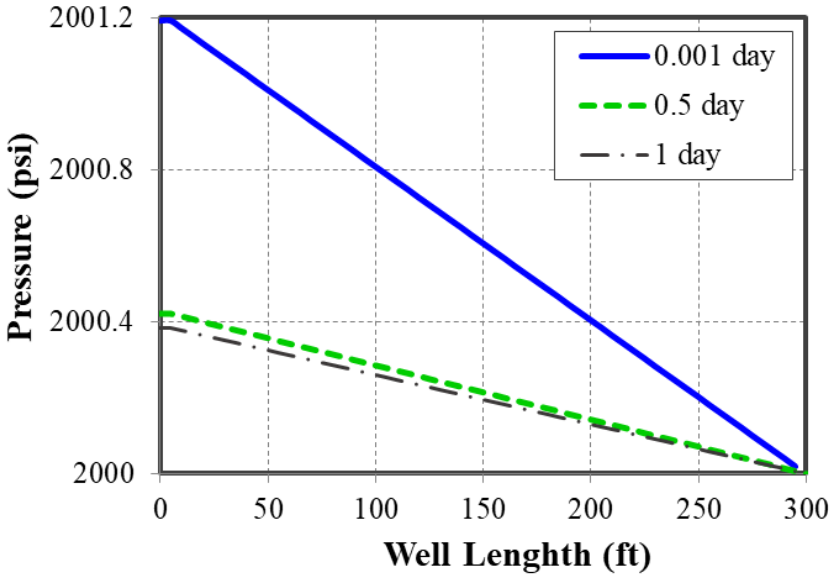

(c) Pressure Profile

Figure 4.10: Simulation results of flow rate, gas accumulative production, and pressure for base case.

Fig. 4.11 illustrates how temperature profile varies along the wellbore with time. Since this is a single fracture reservoir with a single fracture and one perforation at the toe of the wellbore, there is no heat mixing effect inside the wellbore. The wellbore toe (at 0 ft) temperature directly indicates the reservoir inflow temperature. As the results show, the temperature profile along wellbore is mainly controlled by two factors, the reservoir inflow temperature and heat exchange with near-wellbore reservoir rock. The reservoir inflow temperature determines the toe temperature. The heat exchange determines the slope of wellbore flow heating.

The reservoir inflow temperature is affected by the heat conduction and cooling effect as shown in Eq. 4.4. At the beginning of the production, the reservoir depletes rapidly. The enthalpy of gas phase decreases accordingly due to the gas thermal expansion

and Joule-Thompson cooling effect as shown in Eq. 4.13. The reservoir inflow temperature decreases from geothermal 250 °F to 246 °F within 0.001 day. The cooling effect continues until 0.005 day. At that time, the reservoir inflow temperature reaches the lowest point at 241 °F. The heat conduction balances the cooling effect and starts to warm the reservoir fluid back to geothermal temperature. The heat exchange between the inflow and surrounding hot reservoir rock contributes to the heating effect. As shown in Fig. 4.11 the reservoir inflow pressure gradually increases to 247 °F at the end of 1 day.

We notice that at the very beginning, the rate of temperature change is larger than the later time. Because the early-time pressure depletion causes the drop in gas enthalpy. The cooling effect caused by thermal expansion and Joule-Thompson effect can be reflected on the inflow temperature at once. However, it takes much longer time to make the heat conduction effect noticeable. After the reservoir fluid arrives into the wellbore, the temperature profile is mainly controlled by the upstream mixing effect and heat exchange with near-wellbore formation. Since this is single fracture case, there is no upstream mixing effect. We will discuss this effect in the reservoir with five fractures.

The heat exchange with near-wellbore formation is controlled by the heat exchange coefficient and temperature difference between wellbore temperature and near-wellbore temperature. The heat exchange coefficient is determined by the martials of the tubing, casing, and cement, and the reservoir rock conductivity. It remains stable in a short period. The main driving force of the heat exchange is temperature difference. As shown in Fig. 4.11, the gradient of the temperature profile at early time are relatively larger than the later time. This is caused by the reservoir inflow temperature is lower which leads to larger temperature difference. The rate of heat exchange increases accordingly. Meanwhile, the gradient of temperature profile decreases as the wellbore length increases. This is

caused by the up-flow temperature increasing by the heat exchange, which makes the driving force small.

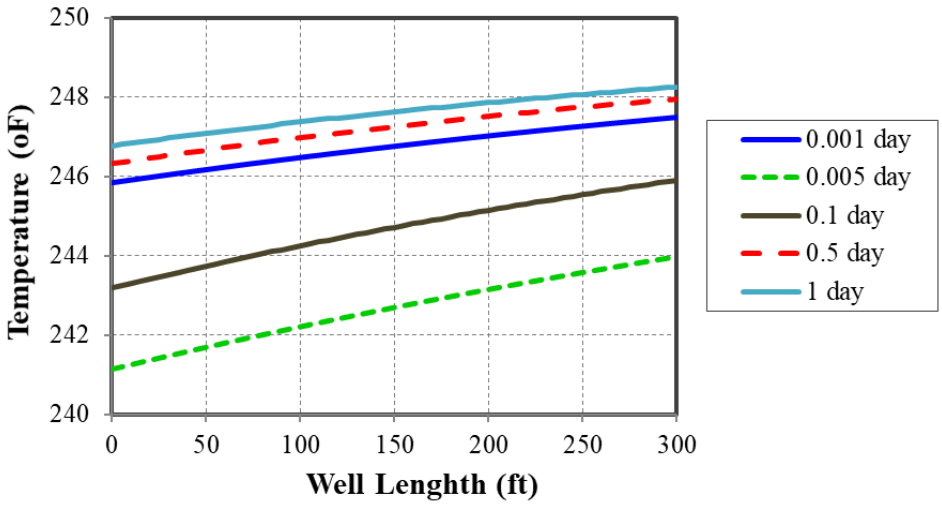

Figure 4.11: Temperature profile at different times for base case.

4.3.1.2 Water and Gas Two Phase Case

Subsequently, a two-phase, water and gas phase, case is constructed to analyze the multiphase flow temperature behavior in the DTS system.

The reservoir parameters, fracture properties, and fracture geometry are similar to the single-phase, single-fracture case except the initial water saturation. For the compositional flash calculation, the irreducible water saturation is set as 20%. Therefore, in order to initiate the water and gas two-phase flow, the initial water saturation is set as 60%.

Fig. 4.12 (a) shows the how flow rate inside the wellbore changes with time. The water flow rate is almost two order less than the gas flow rate. From our flow regime detection algorithm, the horizontal stratified flow is identified for this water and gas phase

system. Even though there is large difference between water and gas flow rate, the decline patterns are almost the same, Fig. 4.12 (b) presents the cumulative production of water and gas. Similar to the flow rate profile, the cumulative production increasing patterns are almost the same even with the actual value in different order. The dotted line in Fig. 4.12 (b) indicates the virtual linear cumulative production increasing behavior. The production increasing rate collapse in a short time due to the early time pressure collapse near the wellbore.

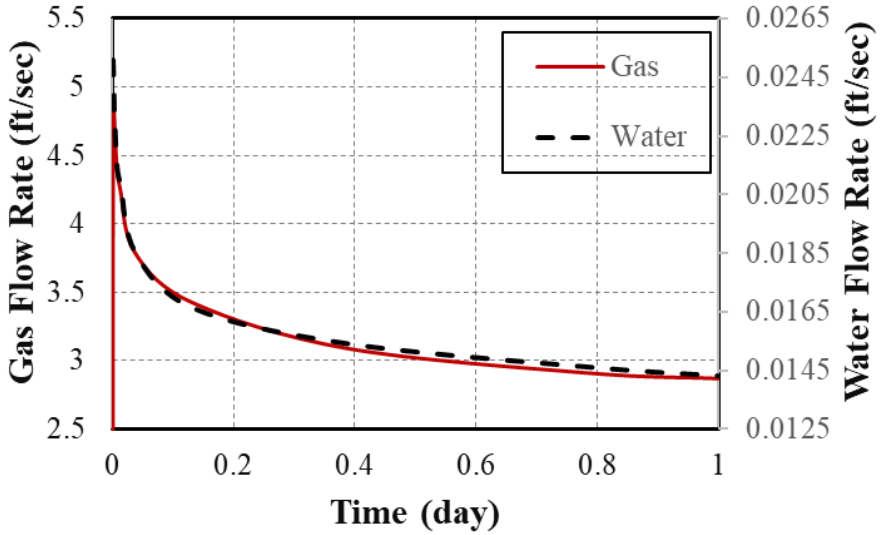

(a) Water and gas flow rate

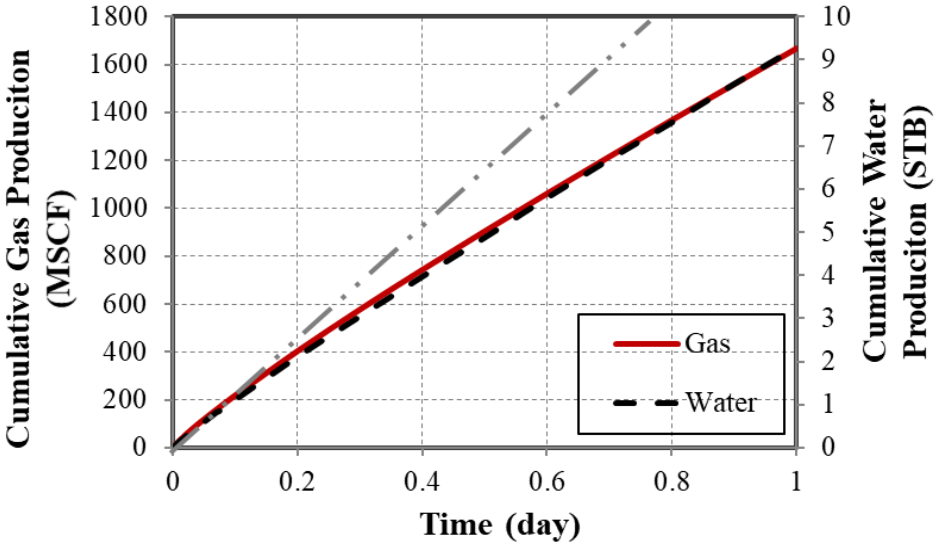

(b) Water and gas cumulative production

Figure 4.12: Simulation results of flow rate and cumulative production for water and gas phase single fracture case.

Fig. 4.13 shows the temperature profile along the wellbore with time for water and gas phase case. Similar to the single phase case, the temperature collapse in a very short time due to the Joule-Tomson effect with large convention. The late time warm-back is dominated by the heat conduction due to the hot reservoir rock. However, an overall higher temperature is observed compared to the single phase case. The flow rate of gas is lower compared to the single phase case. Therefore, the cooling effect by JT effect is more likely compensated by the heat conduction with hot reservoir rock. Moreover, the heat capacity of water is much higher than methane. Consequently, the cooling effect could be countered by the mixing between water and gas phase.

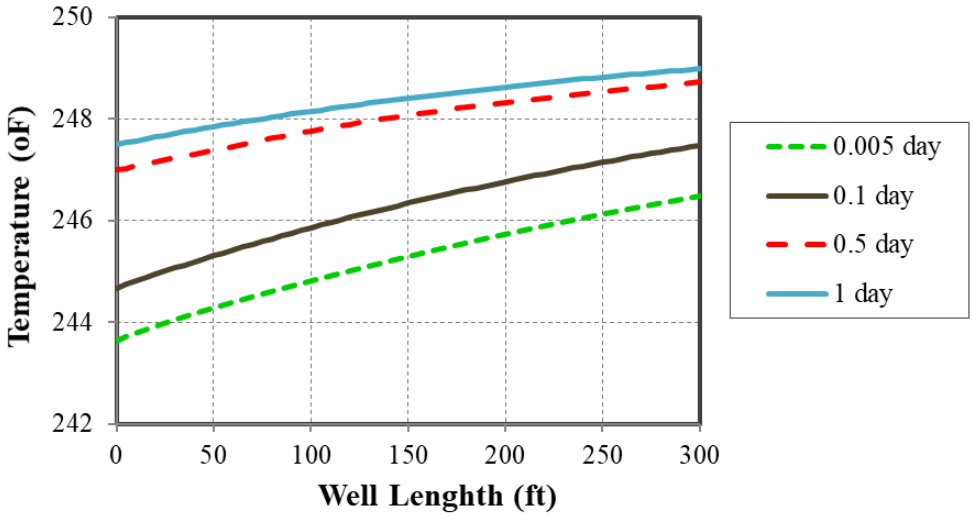

Figure 4.13: Temperature profile along the wellbore for water and gas two phase case.

4.3.1.3 Effect of Reservoir Matrix Permeability

Fig. 4.14 presents the effect of the reservoir matrix permeability on temperature profile along the wellbore. From the comparison between the 0.001 md reservoir matrix permeability case, 0.05 md reservoir matrix permeability case, and 0.1 md reservoir matrix permeability case, we observe that the temperature profile of 0.001 md permeability case remains high and stable while the 0.05 md, and 0.1 md permeability case experiences obvious temperature drop and warm back. The reasons behind it is that the 0.001 md reservoir matrix permeability is extra low, the reservoir matrix cannot support the large inflow. Therefore, the cooling caused by the thermal expansion and Joule-Thompson effect is restricted by the small convection. The heating conduction quickly balances the cooling effect. The temperature profile reaches the relatively stable condition in the early time and gradually warms up to the geothermal temperature. Since reservoir permeability is closely related to the reservoir inflow rate. Therefore, the higher matrix permeability will lead to a lower reservoir inflow temperature.

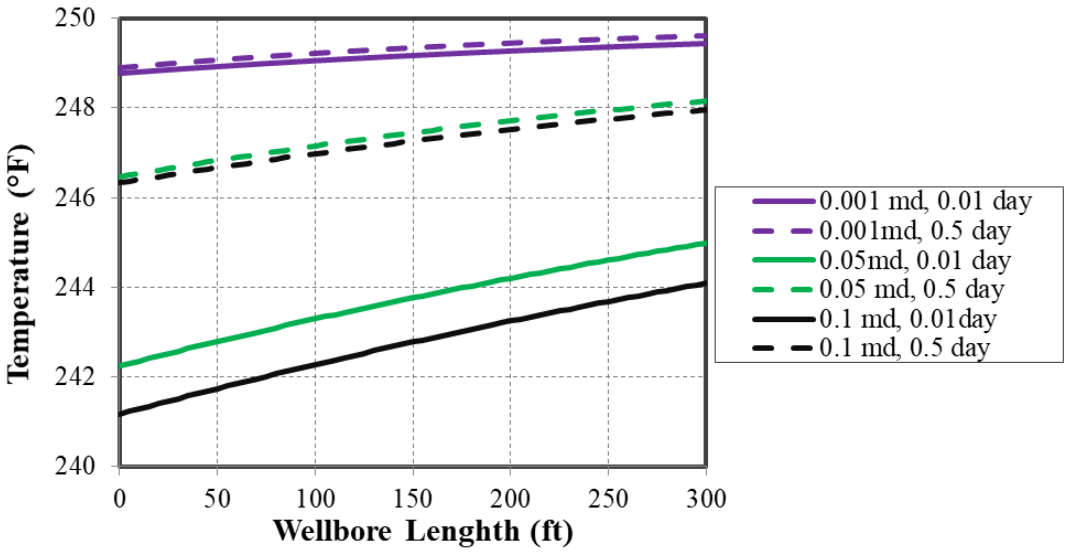

Figure 4.14: Effect of reservoir matrix permeability on temperature profile.

4.3.1.4 Effect of Fracture Conductivity

Fracture conductivity is the product of fracture permeability and fracture width. In the fracture conductivity analysis, we change both the fracture permeability and fracture width to study the impact of fracture conductivity on temperature profile along the wellbore. **Figs. 4.15 and 4.16** show the fracture conductivity sensitivity analysis with fracture width and fracture permeability, respectively. As shown in the results, inflow temperatures are lower with either higher fracture width or fracture permeability. The temperature profile gradients are higher with either lower fracture width or fracture permeability. The high conductivity leads to high inflow and severe pressure depletion. The convection effect is more noticeable. More fluid comes into the wellbore with the thermal expansion and Joule-Thompson effect. An interesting observation is made that even though the toe temperature of 5000 md fracture permeability at 0.5 day case is higher than the 800 md fracture permeability at 0.01 day case, the heel temperature of high fracture permeability case is lower. The large reservoir inflow caused the flow rate inside wellbore is much higher than the low fracture permeability case. The large flow velocity leads to the less time for gas to exchange heat with the near-wellbore formation. Consequently, the heating up effect decreases.

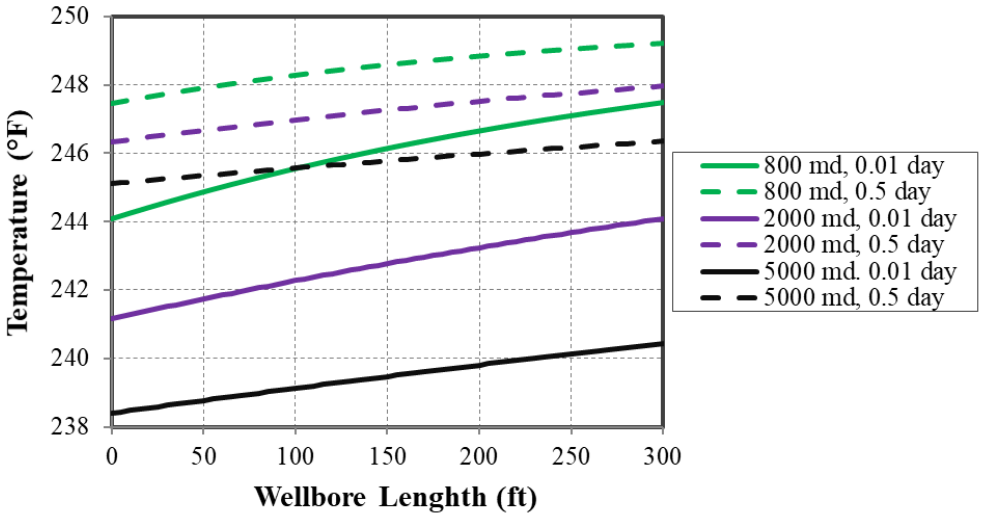

Figure 4.15: Effect of fracture permeability on temperature profile.

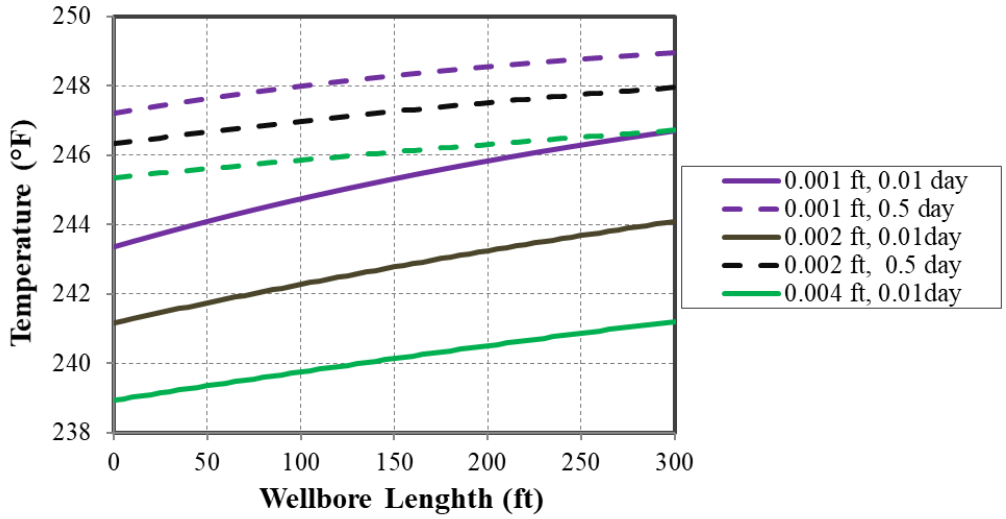

Figure 4.16: Effect of fracture permeability on temperature profile.

4.3.1.5 Effect of Rock Thermal Conductivity

Rock thermal conductivity controls the heat conduction in the reservoir between matrix and hydrocarbon phase. The higher rock heat conductivity, the higher heat exchange. **Fig. 4.17** presents the impact of reservoir rock heat conductivity on temperature profile along the wellbore. The reservoir flow with higher heat conductivity is experienced with more obvious warming up.

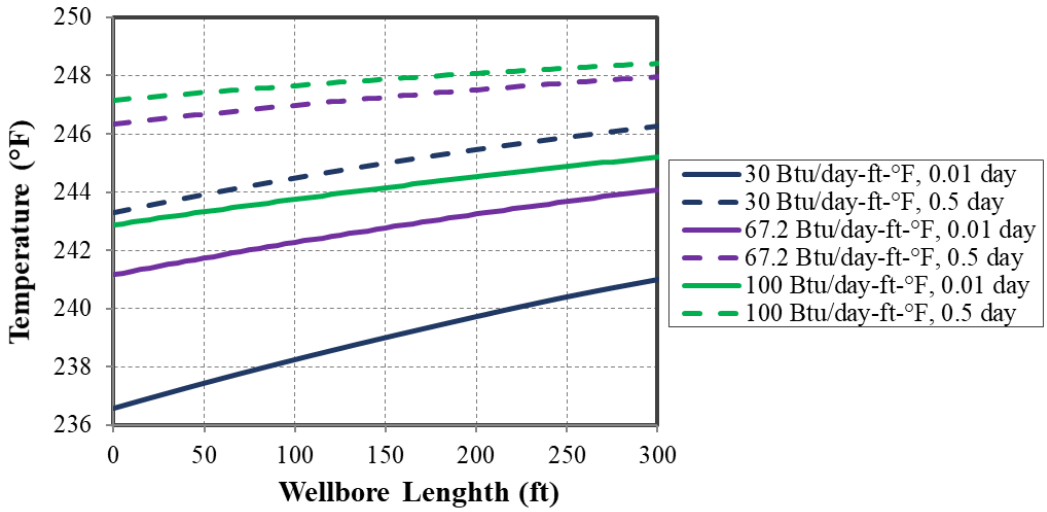

Figure 4.17: Effect of reservoir rock thermal conductivity on temperature profile.

4.3.1.6 Effect of Heat Exchange Coefficient

The heat exchange coefficient controls the gradient of the temperature profile along the wellbore. We set the total heat exchange coefficient to 0.2, 5, and 20 Btu/hr-°F for simplicity. The result is shown in **Fig. 4.18**. As the result shows, toe temperatures are the same at different time since the heat exchange has no impact on reservoir inflow. The temperature gradient with bigger heat exchange coefficient is larger. We notice that the temperature does not change along the wellbore much with the heat exchange coefficient

below 0.2 Btu/hr-°F. The nearly straight-line temperature profile is bad for DTS data interpretation especially the multi-stage fracturing evaluation. The upstream flow temperatures are almost the same at the different perforation since the the heat exchange is low and temperature remains almost constant along the wellbore. We cannot extract effective information from temperature mixing effect at different cluster since the temperature difference is trivial. For the DTS interpretation, we should install a fiber optical in the wellbore with higher heat exchange coefficient. Also, we notice the temperature gradient decreases with time under the same heat exchange coefficient due to the lower temperature difference.

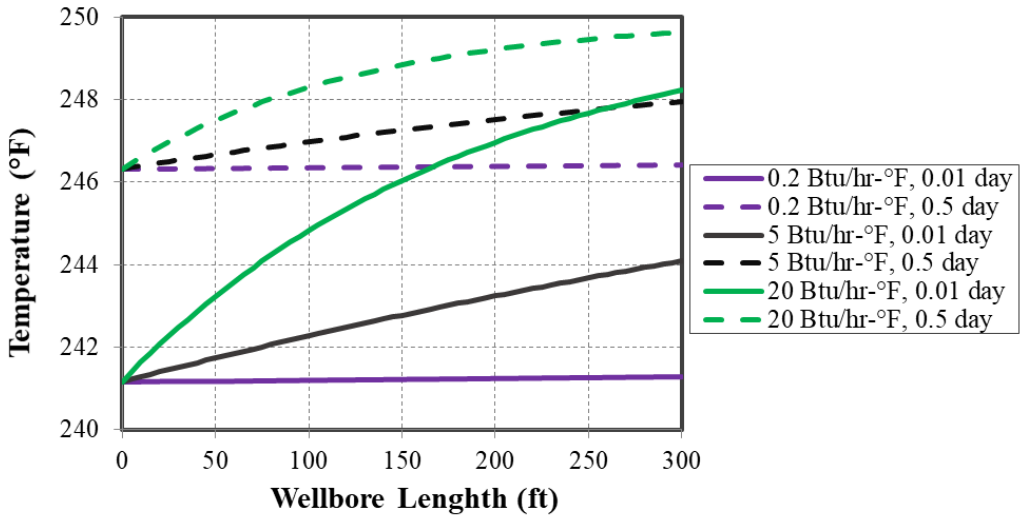

Figure 4.18: Effect of reservoir rock thermal conductivity on temperature profile.

4.3.2 Five Fractures Case study

4.3.2.1 Equal Spacing Five Fractures

The five fractures case involves the temperature mixing effect with upstream flow and the interference among fractures. The reservoir matrix and wellbore properties are the same as shown in Tables 4.5 through 4.8. A horizontal wellbore including five hydraulic fractures with equal fracture spacing of 80 ft is shown in **Fig. 4.19**. In addition, fracture permeability is 1000 md, fracture half-length is 250 ft with fracture width of 0.02 ft, and the wellbore length is 800 ft.

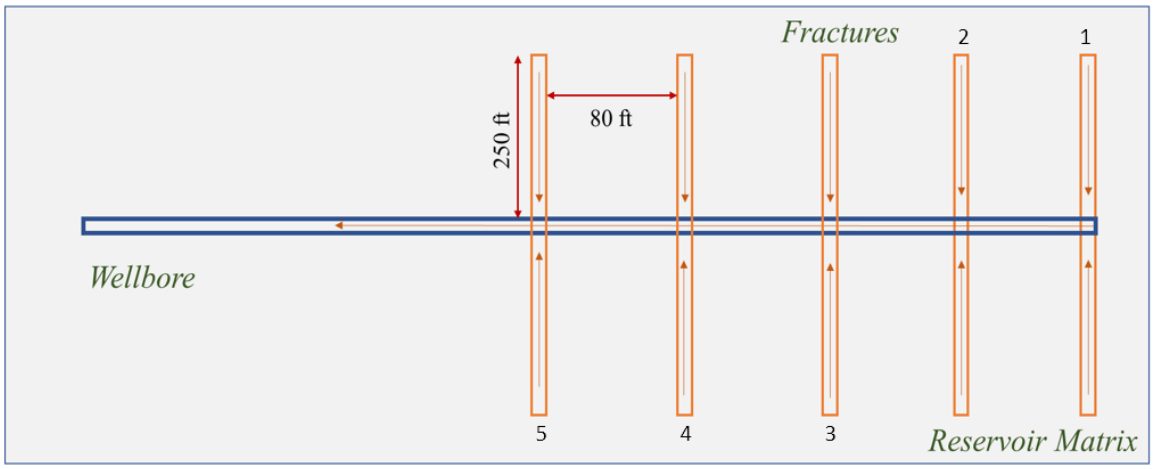

Figure 4.19: Schematic view of a horizontal wellbore with equal spacing five fractures case.

Fig. 4.20 shows the flow rate profile along the wellbore. As the result shows, the flow rate increases at every perforation point with reservoir inflow. The reservoir inflow rates at different perforation points are nearly evenly distributed within 1 day. We can also notice that the flow rate of the five fractures case decreases rapidly within one day as the single fracture case. **Fig. 4.21** shows the temperature profile along the wellbore at different

time. The cooling effect becomes less noticeable from fracture 1 to fracture 5 due to the mixing effect. Even though the differences among reservoir inflow rate and temperature at different perforation points are small, the upstream flow is heated up with the heat exchange with the near-wellbore formation. The higher accumulative upstream flow rate with higher temperature smears the downstream perforation point reservoir inflow cooling effect. The reservoir inflow temperatures at different perforation points are also tracked. Table 4.9 shows the reservoir inflow temperature from fracture 1 to 5 at 1 day. As the result shows, the reservoir inflow temperatures are symmetric at fracture 3. The fracture located at two sides of the stage, fracture 1 and fracture 5, have higher inflow temperature. Because the reservoir rock between the fractures is experienced with more cooling effect. The heating conduction effect inside the cluster is small since the temperature difference between reservoir rock and fracture inflow is small. However, the fractures located at the both sides of the cluster are exposed to the hot surrounding reservoir rock. The heat conduction effect is strong, leading to a higher reservoir inflow temperature.

Fracture Number	**1**	**2**	**3**	**4**	**5**
Temperature (°F)	248.20	247.90	247.89	247.90	248.20

Table 4.9: Reservoir inflow temperature at different perforation at 1 day for equal spacing fractures case.

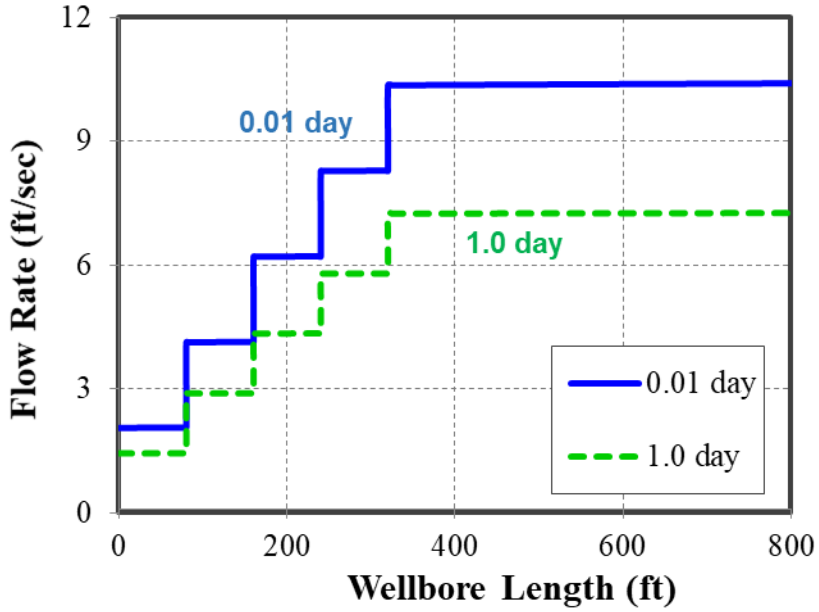

Figure 4.20: Flow rate profile along the wellbore for equal spacing fracture geometry case.

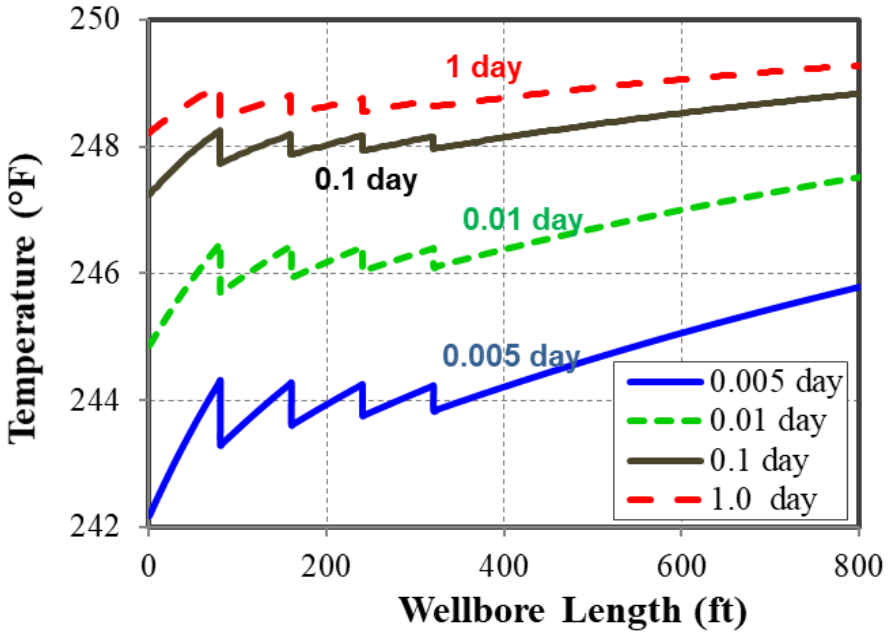

Figure 4.21: Temperature profile along the wellbore for equal spacing fracture geometry case.

4.3.2.2 Complex Five Fractures

In the field fracturing operation, the fractures generated are usually with unequal spacing, complex geometry and heterogenous property. To study the complex subsurface situations, we design a complex five fractures case as shown in **Fig. 4.22**. As the schematic view shows, each fracture has different fracture half-length and permeability and the spacing between fractures is unequal. The reservoir matrix and wellbore properties are the same as the equal spacing five fractures case.

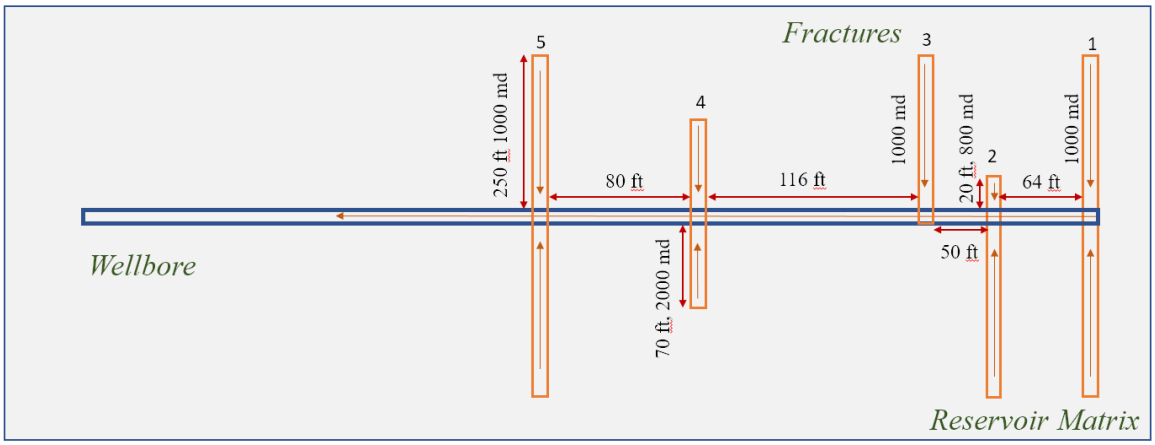

Figure 4.22: Schematic view of a horizontal wellbore with complex five fractures case.

Fig. 4.23 presents the flow rate profile along the wellbore with time. The rapid decreasing trend in flow rate profile still exists as equal spacing five fractures case, which indicates the quick pressure depletion in the reservoir. From Table 4.10, we notice the the most reservoir inflow comes from fracture 4 due to the high fracture conductivity. Therefore, the reservoir inflow from perforation 4 may have an obvious cooling effect. **Fig. 4.24** illustrates the temperature profile along the wellbore with time. There are cooling down and warm back trends as expected. Compared to the equal spacing case, the

temperature drop in fracture 4 is huge while temperature remains almost the same at perforation 5. There are several reasons behind it. As Fig. 4.22 shows, the fracture 4 has the highest fracture conductivity, which leads to a highest flow rate and highest cooling effect as shown in Tables 4.10 and 4.11. Meanwhile the spacing between fracture 3 and fracture 4 is longest to allow more heat exchange. There is enough time for cooler fluid in the wellbore to be heated up before it reaches fracture 4. Consequently, the large low temperature reservoir inflow at fracture 4 and sufficient heat transfer between fracture 3 and 4 contribute to the obvious cooling effect at fracture 4. When the high flow rate upstream flow comes to perforation 5, the temperature difference between upstream flow temperature and reservoir inflow at perforation 5 is very small as shown in Fig. 4.24. Therefore, the mixing effect smears the cooling effect at perforation 5. We can also notice that the temperature at both sides of the stage is higher due to the lower fracture conductivity and exposure to surrounding hot reservoir rock.

Fracture Number	**1**	**2**	**3**	**4**	**5**
Inflow Rate (ft/sec)	2.32	1.95	1.88	3.22	2.32

Table 4.10: Reservoir inflow rate at different perforation at 1 day for complex five fractures case.

Fracture Number	**1**	**2**	**3**	**4**	**5**
Temperature (°F)	246.88	246.62	246.46	245.69	246.56

Table 4.11: Reservoir inflow temperature at different perforation at 1 day for complex five fractures case.

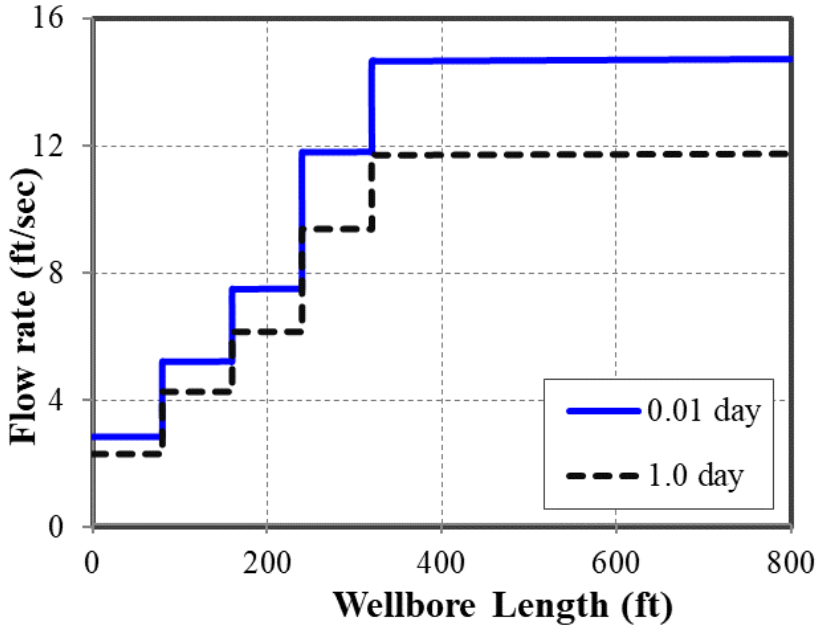

Figure 4.23: Flow rate profile along the wellbore for complex fracture geometry case.

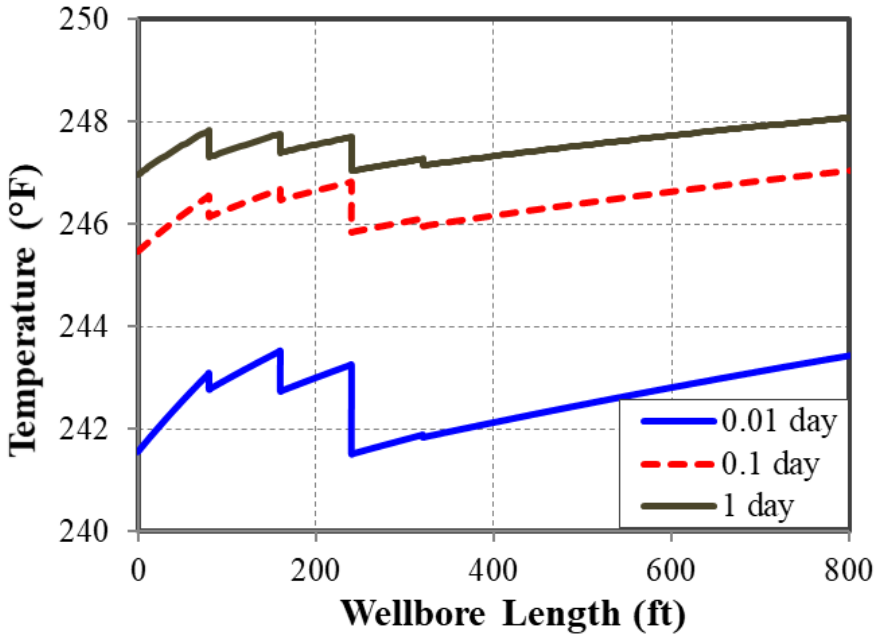

Figure 4.24: Temperature profile along the wellbore for complex fracture geometry case.

4.4 Summary

- A new comprehensive model for the DTS data interpretation is introduced. The governing equations for the pressure and temperature field in reservoir domain and wellbore domain are listed. The fluid properties are calculated with the compositional model.
- The theoretical background for the Joule-Thomson effect and flow regime in horizontal well are introduced.
- The coupling scheme between the wellbore and reservoir model is illustrated.
- Reservoir model is verified with CMG STAR while wellbore model is verified with OLGA.
- A series of sensitivity analysis are conducted on a single fracture production horizontal well.
- An equal spacing five fracture case is simulated to study the temperature mixing effect.
- A complex geometry five fracture case is simulated to analyze the impacts of fracture geometry, fracture properties, and fracture spacing on the temperature profile along the wellbore

Chapter 5: Overview of DFIT Data Interpretation Workflow

DFIT data interpretation is mainly classified into two parts: before closure analysis and after closure analysis. Before closure analysis focuses on the fracture characterization during the fracture initiation and fracture propagation. The geomechanics knowledge is applied to obtain a better understanding of the geometry of mini fracture generated by the DFIT test. The key parameters for fracture design such as closure pressure, leak-off coefficient, and injection efficiency can be contained with before closure analysis. After closure analysis is similar to pressure transient analysis after the fracture is closed. The flow regime is first detected. The well testing knowledge is applied to obtain the initial reservoir pressure and reservoir matrix permeability.

5.1 Before Closure Analysis

5.1.1 Fracture Propagation Pattern Detection

The injection rate used to generate the mini fracture during the DFIT operation is very low. Consequently, it is hard to generate the complex fracture network. Generally, three simple fracture propagation models, Perkins-Kern-Nordgren (PKN) (Perkins and Kern 1961, Nordgren 1972) model, Khristianovic-Geertsma-de Klerk (KGD) (Khristianovich et al. 1955) model, and radial model, are applied to characterize the fracture geometry, particularly the width and length for a specified flow rate.

The original work on fracture propagation model was done by several Russian researchers (Khristianovich et al. 1959). Carter (1957) developed a model that fulfills the volume balance with simple assumption that the fracture width is constant and uniform. The volume balance approach is further developed to KGD and PKN models developed by

Geertsma and de Klerk (1969) and Nordgren (1972), respectively. PKN and KGD models were the first fracture propagation models that include volume balance and geomechanics.

Both PKN and KGD models are applied to the fully confined fractures. The key difference between PKN and KGD models lies in the way they transform the three-dimensional problem into two-dimensional problem. PKN model assumes the vertical cross section acts independently ash shown in **Fig. 5.1**. The pressure at any vertical section is controlled by the height of the section. KGD model, on the other hand, assumes the all horizontal cross sections are identical as shown in **Fig. 5.2**. The fracture width change in vertical section is almost trivial.

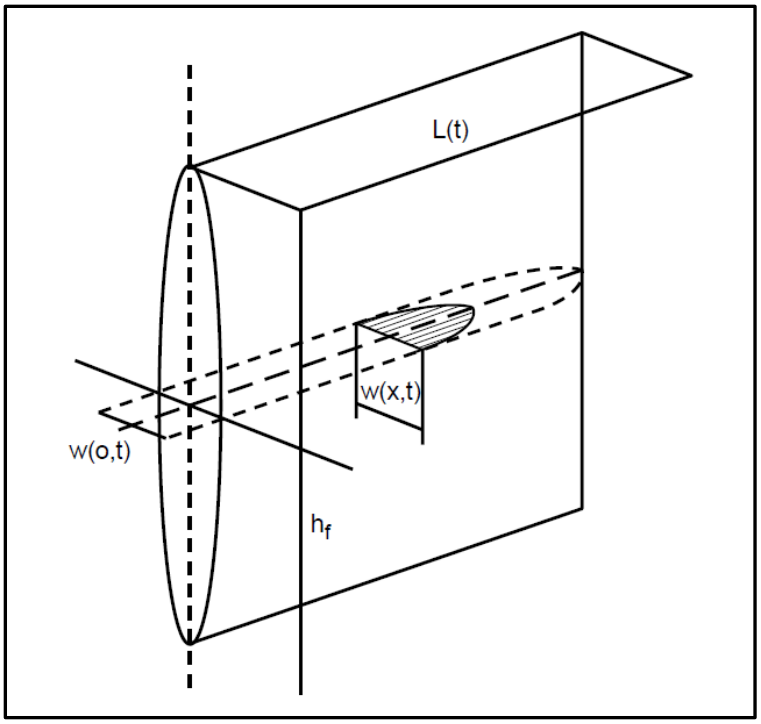

Figure 5.1: Schematic view of PKN model (Economides and Nolte 1989).

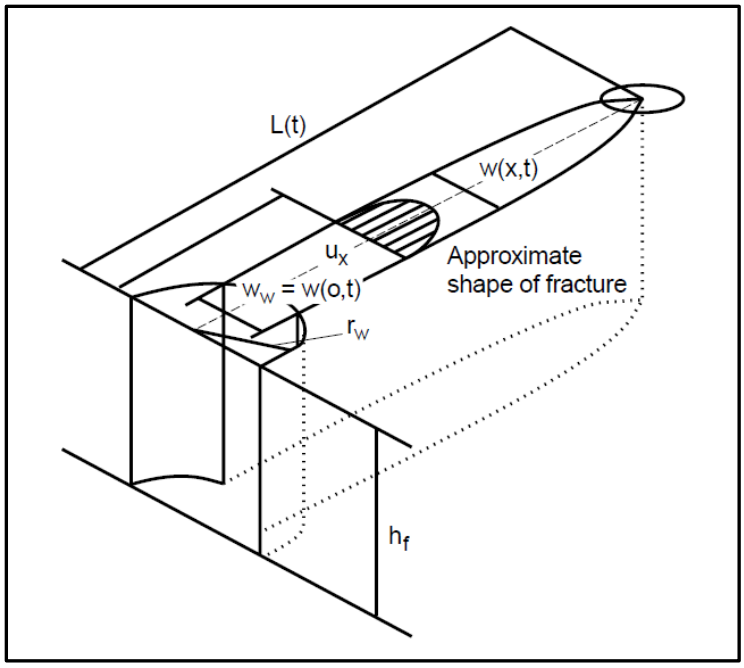

Figure 5.2: Schematic view of KGD model (Economides and Nolte 1989).

PKN model usually holds true when the fracture length is much greater than fracture height. KGD model, on the other hand, is valid when the fracture height is much greater than fracture length.

Radial model as shown in **Fig 5.3**, is mainly applied to the fracture which grows unconfinedly from a point source, which means there is no barrier constraining the fracture height growth.

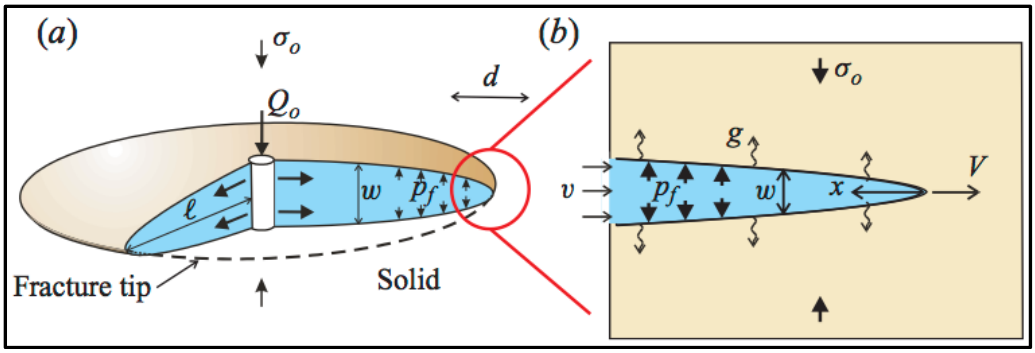

Figure 5.3: Schematic view of radial model (Bunger et al. 2013).

However, in the real-field data, the pressure curve hardly follows the above three theoretical fracture propagation models. The field DFIT data usually shows the combinations of different fracture propagation models or modified basic fracture propagation models.

The common method to determine the fracture propagation pattern is log-log net pressure versus time plot as shown in **Fig. 5.4**. At the beginning, the pressure decreases for a short time before the fracture is confined by the barrier, which usually can be described as radial model or KGD model. After the fracture touches the barriers, the pressure increases following the PKN model. The pressure may reach a constant level due to the accelerated near-wellbore fluid loss, which may indicate a T shaped fracture. Subsequently, an increase in pressure indicates the restricted extension while a decrease in pressure indicates the uncontrolled height growth. The specific log-log slope range to detect the fracture propagation pattern is shown in Table 5.1.

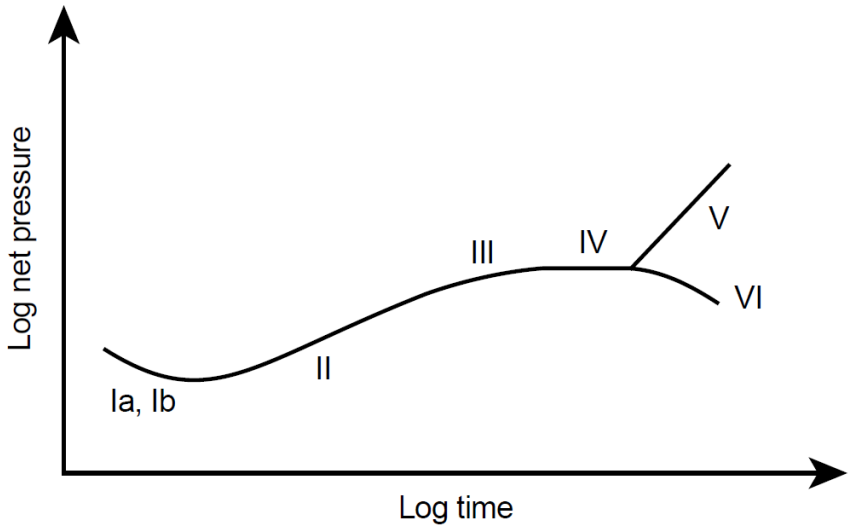

Figure 5.4: Log-log plot of pressure behavior during the injection stage (Economides and Nolte 1989).

Propagation Type	Log-Log Slope	Interpretation
Ia	–⅙ to –⅕	KGD (Eq. 9-36)
Ib	–⅛ to –⅕	Radial (Eq. 9-37)
II	⅙ to ¼	PKN (Eq. 9-35)
III	Reduced from II	Controlled height growth Stress-sensitive fissure
IV	0	Height growth through pinch point Fissure dilation T-shaped fracture
V	≥1	Restricted extension
VI	Negative following IV	Uncontrolled height growth
Note: n = 0.5		

Table 5.1 Fracture propagation model detection with log-log slope (Economides and Nolte 1989).

Sometimes, even with the log-log net pressure versus time plot, the fracture propagation pattern still remains unclear. A new volume balance based workflow for fracture model detection is developed by Wang et al. (2017). With the assumption of power law fracture growth, negligible spurt loss, constant fracture surface after shut-in and Carter's leak-off model, a simple equation for the pressure decline can be expressed as:

$$p_f\left(\Delta t_D\right) = ISIP - \frac{\pi r_p C_L S_f \sqrt{t_p}}{2} G\left(\Delta t_D\right), \tag{5.1}$$

where p_f is the fracture pressure at dimensionless time Δt_D. $ISIP$ is the instantaneous shut-in pressure. t_p is the total pumping time. S_f is the fracture stiffness. Fracture stiffness can be calculated based on the fracture propagation model as shown in Table. C_L is the leak-off coefficient. r_p is ratio of the permeable fracture surface area to total fracture surface area. In this study, r_p is assumed to be 1.

The square root of time function can also be employed to calculate fracture stiffness as

$$p_f\left(\Delta t_D\right) = ISIP - 4S_f\left(ISIP - P_0\right)\sqrt{\frac{k\phi c_t \Delta t}{\pi \mu_f}}, \tag{5.2}$$

where P_0 is the net pressure at *ISIP* and μ_f denotes fluid viscosity.

Fracture Geometry	PKN	KGD	Radial
S_f	$\frac{2E'}{\pi h_f}$	$\frac{E'}{\pi x_f}$	$\frac{3\pi E'}{16R_f}$

Table 5.2: Fracture stiffness with different fracture propagation models (Wang et al. 2017).

The G-function time is defined as

$$G\left(\Delta t_D\right)=\frac{4}{\pi}\left[g\left(\Delta t_D\right)-g(0)\right], \tag{5.3}$$

where g-function time can be approximated by

$$g\left(\Delta t_D\right)=\begin{cases}(1+\Delta t_D)\sin^{-1}(1+\Delta t_D)^{-0.5}+\Delta t_D{}^{0.5}, & \eta\to 0\\ \frac{4}{3}\left[(1+\Delta t_D)^{1.5}-\Delta t_D{}^{1.5}\right], & \eta\to 1\end{cases}. \tag{5.4}$$

Therefore, from the pressure decline curve, the declining slope can be measured. With the gradient, fracture stiffness can be calculated with Eq. 5.1. With Table 5.2, the other volumetric parameter can be calculated. Consequently, the fracture volume for different fracture propagation models can be obtained. Since the injection efficiency for mini fracture is usually high, the fracture volume can be approximated to the injection volume. The calculated injection volume is then compared with the actual injection rate. The fracture model with closest match with the real injection rate will be selected as the actual fracture propagation model.

5.1.2 Closure Point Selection

The G-function plot is mainly applied to detect the closure point as shown in **Fig. 5.5**. For the $G\frac{dP}{dG}$ versus G plot, there is an obvious linear increasing behavior at the start. Subsequently, the pressure transient behavior deviates from the linear correlation and reaches the peak pressure value. After that, pressure begins to fall off.

The Holistic method (Barree et al. 2007) to pick the closure point is to select the deviation point from the linear behavior near the peak pressure as shown in Fig. 5.5. The corresponding pressure and time at that point are the closure pressure and closure time. The closure pressure and time are further used to calculate the leak-off coefficient for fracture design. Theoretically, the closure pressure is not the minimum stress of reservoir rock. But it is a good approximation to minimum reservoir rock stress.

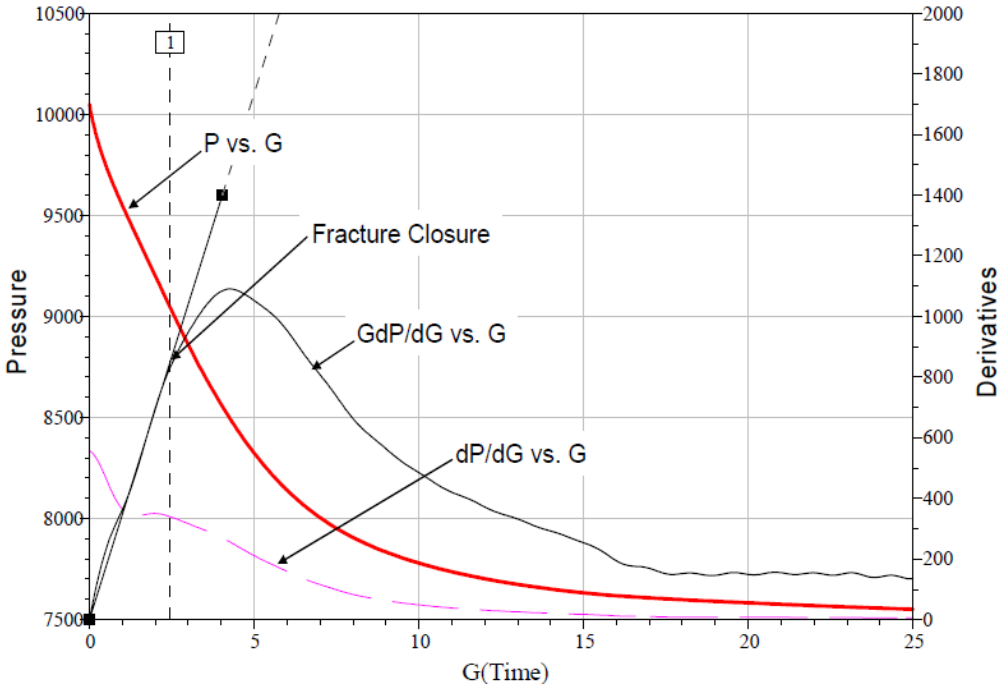

Figure 5.5: Holistic closure point detection (Barree et al. 2007).

However, in recent years, there are different opinions towards how to select the closure point in $G\frac{dP}{dG}$ versus G plot. McClure et al. (2014) developed a geomechanics based fracture propagation simulation software CFRAC to simulate the mini fracture initiation and propagation. The result shows that the closure point should be picked at the early deviation point from the linear behavior instead of the deviation point near the peak. For example, **Fig. 5.6** (a) shows a typical G function plot. With Holistic method, the closure point should be around 5 in G function time. However, McClure zoomed in the early pressure transient behavior as shown in Fig. 5.6 (b) and picked the closure point around 2 in G function time.

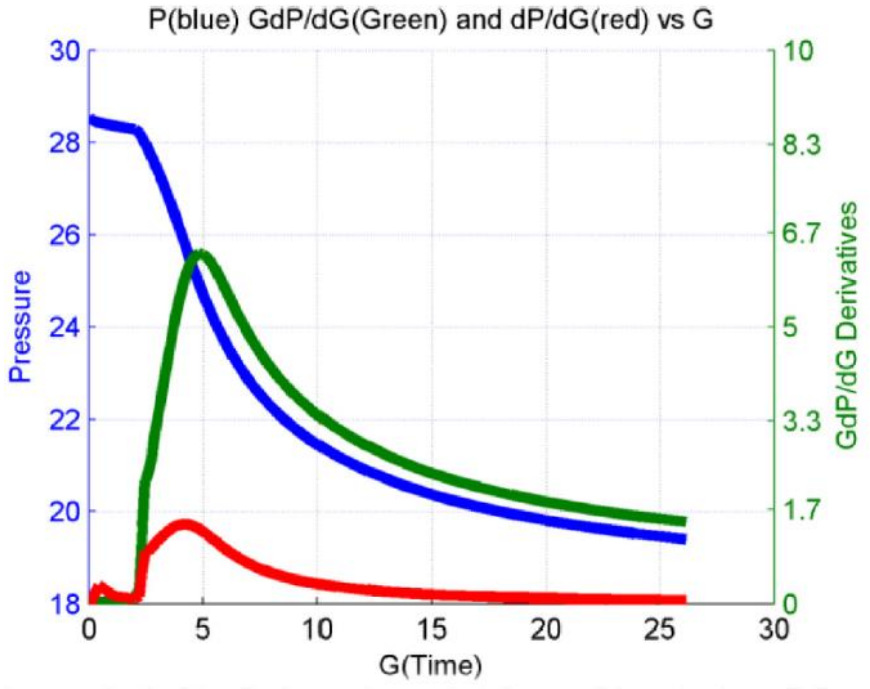

(a) Original G function plot

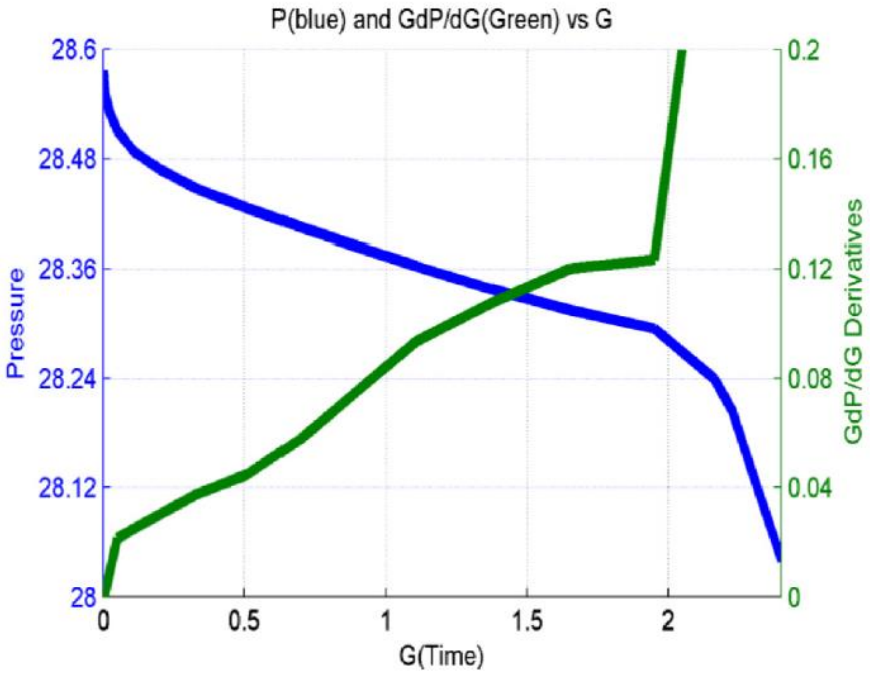

(b) Early time zoom in G function plot

Figure 5.6: McClure closure point pick illustration (McClure et al. 2014).

Wang et al. (2017) suggested that the deviation point at early time indicates the lower bound of closure point while the deviation point near the peak indicates the upper bound of closure point. The average of the lower bound and upper bound is suggested to be used for leak-off coefficient calculation.

However, there is no solid evidence to prove which method is correct. In this study, we will use the Wang's method, which picks the average deviation point as the closure point.

After the closure time and closure pressure are determined, the leak-off coefficient can be calculated as

$$C_L = \frac{p^* \beta_s}{r_p \sqrt{t_p E'}} \begin{cases} h_f, & \text{PKN} \\ 2L, & \text{KGD} \\ (32\pi / 3\pi^2)R, & \text{Radial} \end{cases} \tag{5.5}$$

where β_s is the ratio of average net pressure in the fracture to net pressure at the wellbore at the end of the pumping. p^* denotes the modified pressure slope based on the fracture propagation model.

The fluid efficiency is determined by

$$\eta = \frac{G^*}{2\kappa + G^*} \tag{5.6}$$

where G^* is the ratio of shut-in net pressure to modified pressure p^*. κ is spurt loss coefficient.

5.2 After Closure Analysis

5.2.1 Flow Regime Detection

The transient behavior of a vertical fracture with finite conductivity mainly includes three flow regimes: linear flow, bilinear flow, and pseudo-radial flow as shown in **Fig. 5.7**. At the beginning, the system has the fracture linear flow. After a transition flow period, the bilinear flow may or may not exist. Finally, the the system enters the radial flow.

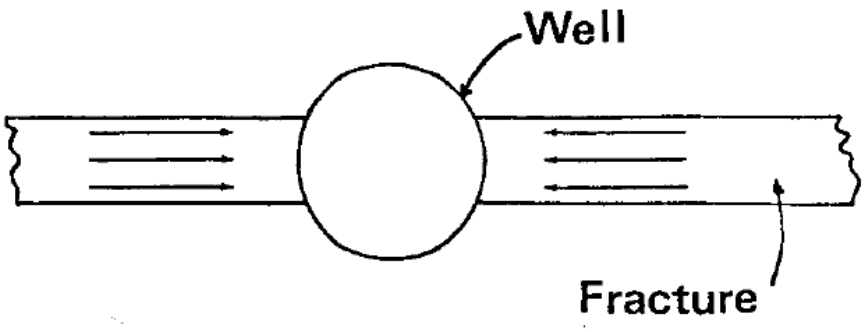

(a) Linear flow regime

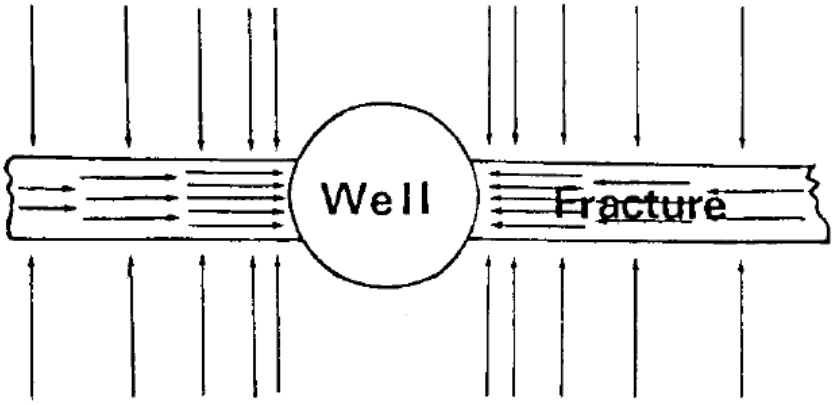

(b) Bilinear flow regime

Figure 5.7: Three after closure fracture flow regimes (Cinco-Ley et al. 1981).

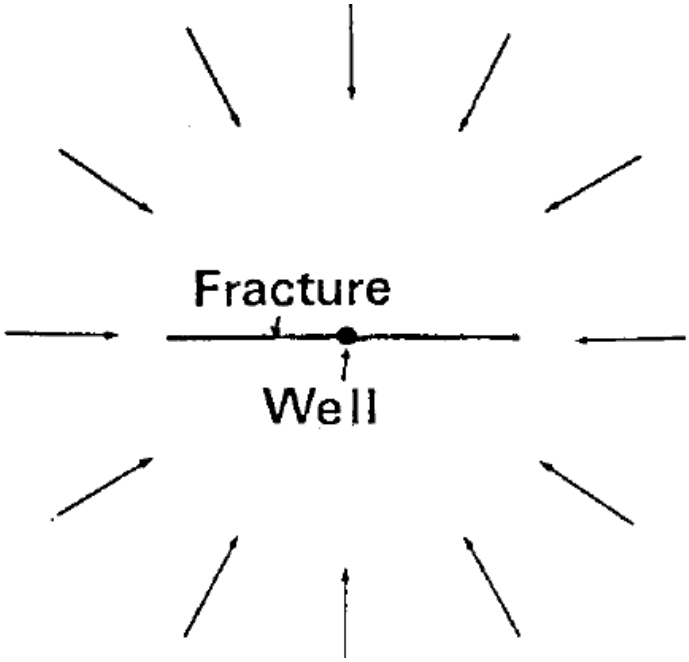

(c) Radial flow regime

Figure 5.7: Three after closure fracture flow regimes (Cinco-Ley et al. 1981).

There are mainly two methods to distinguish the flow regimes after fracture closure. Soliman and Cinco-ley used the slope of the log-log pressure versus time plot to detect the flow regimes. The mechanism behind this method is that different flow regimes have different formulation of pressure declining governing equation. The gradient for linear, bilinear, and radial flow are -0.5, -0.75, and -1, respectively.

Another method for the flow regime identification is to use diagnostic log-log plot of pressure difference based on $\{F_L(\mathrm{t}/\mathrm{t}_c)\}^{-2}$. $\{F_L(\mathrm{t}/\mathrm{t}_c)\}$ can be calculated as

$$F_L(\mathrm{t}/\mathrm{t}_c) = \frac{2}{\pi}\sin^{-1}\left(\sqrt{\frac{t_c}{t}}\right). \tag{5.6}$$

In diagnostic log-log plot, the straight line with a half slope indicates linear flow while the straight line with a unity slope indicates radial flow as shown in **Fig. 5.8**. In this study, we will use $\{F_L(t/t_c)\}$ function to detect the flow regime and further calculated the reservoir parameters.

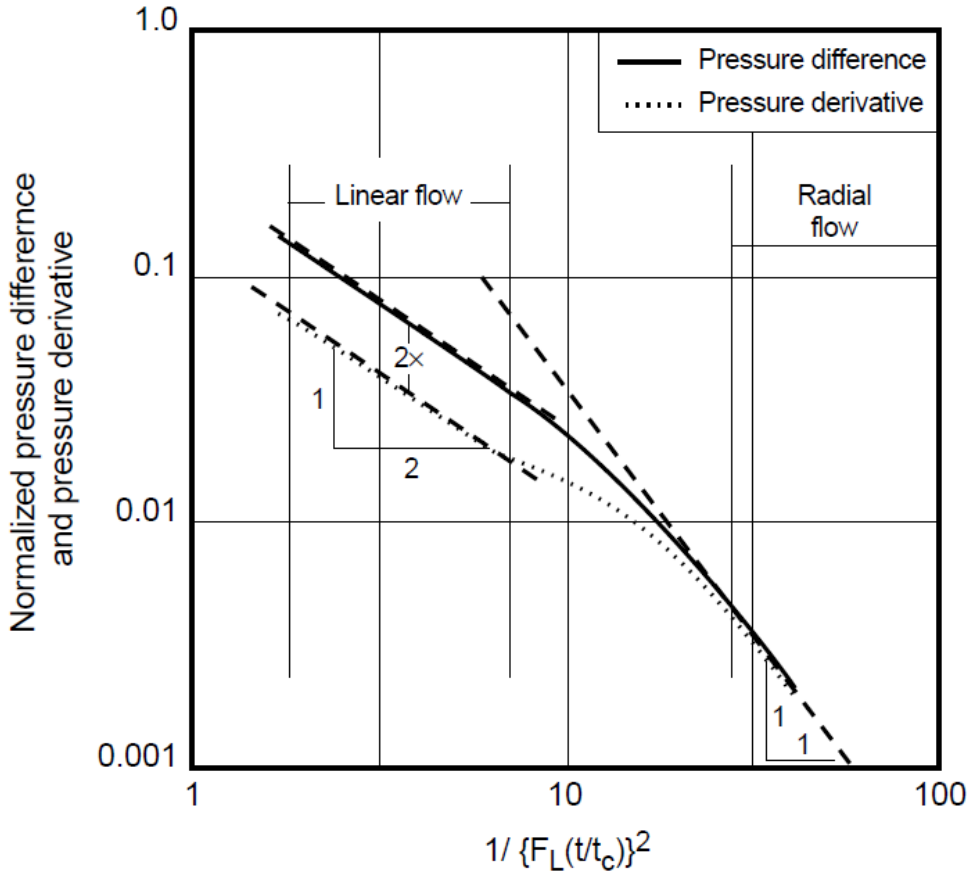

Figure 5.8: Flow regime detection with $F_L(t/t_c)$ function.

5.2.2 Reservoir Parameters Determination

For the radial flow analysis, the key parameters, initial reservoir pore pressure and reservoir transmissibility can be obtained.

Initial reservoir pore pressure can be identified with pressure versus $\{F_L(t/t_c)\}^2$ plot. The linear behavior section in the plot is extended to the pressure axial. The intersection point indicates the initial reservoir pore pressure as shown in **Fig. 5.9**. In this case, the initial reservoir pore pressure is 3736 psi.

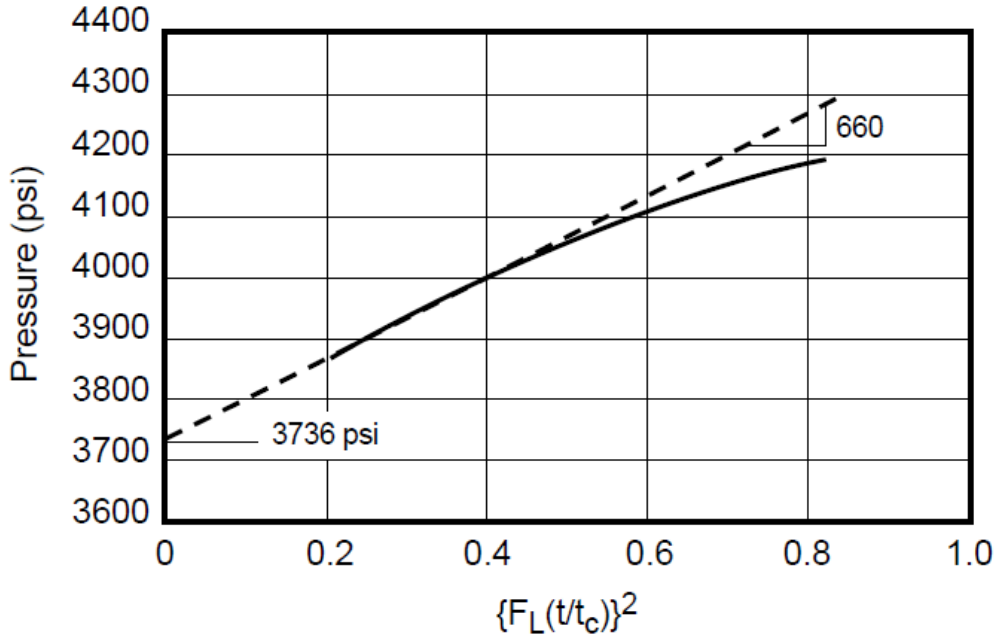

Figure 5.9: Radial flow permeability and initial pore pressure calculation.

The slope of linear section can be used to calculate the reservoir transmissibility:

$$\frac{kh}{\mu} = 2.5\times10^5 \frac{V_i}{t_c}\frac{1}{m_{rf}}, \tag{5.7}$$

where V_i denotes the injected fracturing fluid volume. m_{rf} denotes the slope of linear section.

For the linear flow analysis, the key reservoir parameter spurt and fracture length can be estimated.

The spurt can be calculated with:

$$\kappa = 1 + \frac{4}{\pi}\left[1.118\times10^{-3}\frac{m_{lf}}{C_L}\sqrt{\frac{k\phi c_t}{\mu}} - 1\right]\sqrt{\frac{t_c}{t_p}}, \tag{5.8}$$

where m_{lf} is the slope of linear flow $\left\{F_L(\mathrm{t}/\mathrm{t}_c)\right\}$ function plot.

The fracture length can be obtained with:

$$L = 2.37\times10^{-3}\frac{1}{f_{aL}}\sqrt{\frac{kt_c}{\phi\mu c_t}}\frac{m_{rf}}{m_{lf}}, \tag{5.9}$$

where f_{aL} is apparent fracture half length:

$$f_{aL} = \frac{g_0}{1-\eta}\left[\frac{\kappa}{g_0(\kappa-1)+2\sqrt{t_c/t_p}}\right]. \tag{5.10}$$

5.3 DFIT Field Data Interpretation- Marcellus Shale DFIT Analysis

The field DFIT data we analyzed in this session is a shale gas well in Marcellus shale formation. The length of horizontal well is 2853 ft with true vertical depth of 7120 ft. The estimated reservoir pressure is 4300 psi. The formation thickness is 137 ft in total. The formation is subdivided into honey hole and upper-lower formation. The porosity for honey hole is 0.138 while the porosity for the upper-lower formation is 0.09. The detailed parameters are listed in Table 5.3.

Parameters	**Value**	
TVD	7120	ft
Well length	2853	ft
Porosity (Honey hole)	0.138	
Porosity (Upper lower)	0.09	
Reservoir temperature	130	°F
Thickness (Honey hole)	43	ft
Thickness (Upper lower)	94	ft
Initial gas saturation	0.9	

Table 5.3: Input parameters for Marcellus shale case study.

The injected fluid for initiate mini fracture is 9.9 pound per gallon slick water. The slick water is injected for 10 minutes with pumping rate of 10 barrels per minute. The overall pressure transient behavior is shown in **Fig. 5.10.** In order to generate a mini fracture, the injection time and injection rate are constricted compared to the long term shut-in. The total shut-in time is 300 hrs.

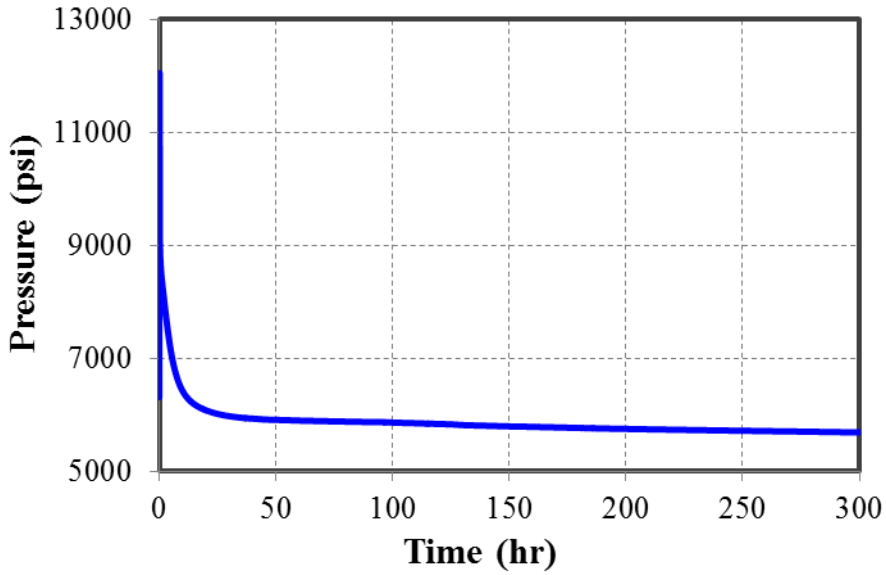

Figure 5.10: Pressure profile during before closure and after closure.

The diagnostic $G\frac{dP}{dG}$ versus G plot is employed to identify the closure point as shown in **Fig. 5.11**. Two deviation points from linear behavior are observed. The early time deviation is marked by green line while the late time deviation is marked by red line. With McClure's method, the closure point should be around 5 G function time; With Holistic method, the closure point should be around 10 G function time. In this study, we adopt the Wang's method to pick the average of upper bound and lower bound as 7.5 G function time. The exact closure time and pressure are 147 mins and 8084 psi.

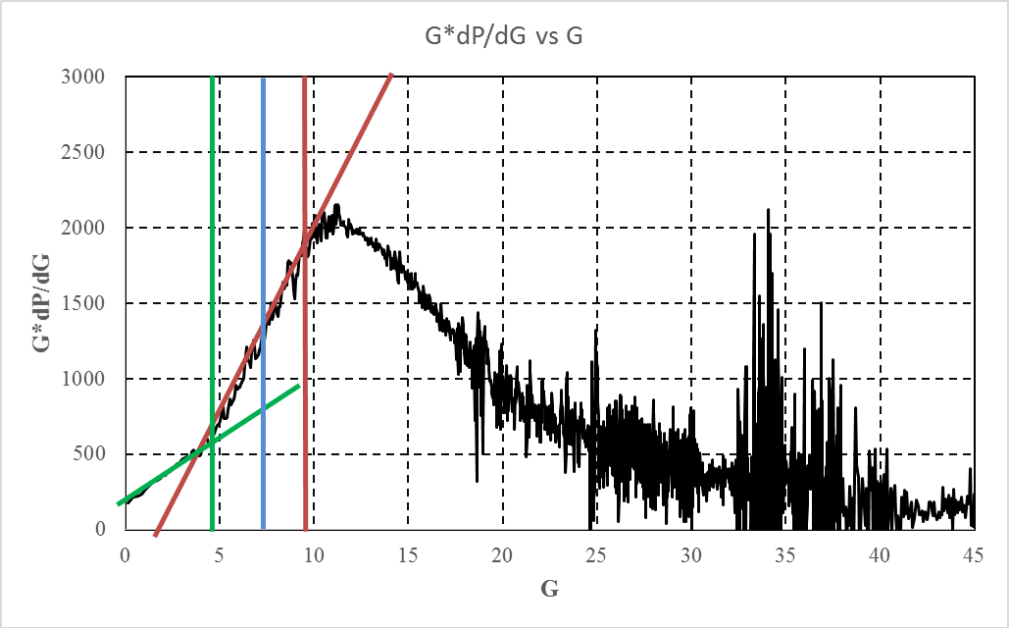

Figure 5.11: Before closure analysis for closure point detection.

For the after closure analysis, the diagnostic log-log net pressure versus $\{F_L(t/t_c)\}^{-2}$ was first employed to detect the flow regime after fracture closure as shown in **Fig. 5.12**. The early linear and bilinear flow behavior only last a very short time. There would be relatively large error with linear flow regime analysis. However, the straight line section with unity slope can be clearly observed in the log-log plot, which clearly indicates the system has entered the radial flow regime. The radial flow regime analysis was conducted for the after closure analysis.

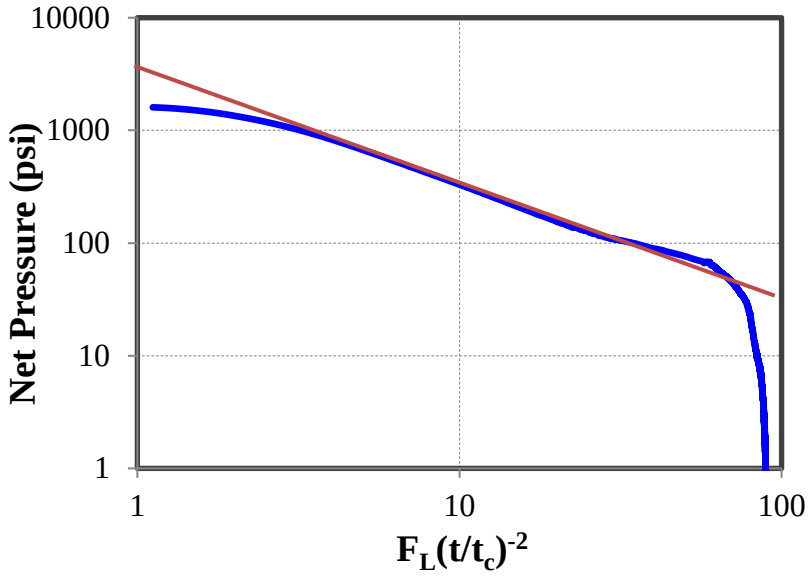

Figure 5.12: Flow regime detection for the Marcellus shale after closure analysis.

For the radial flow regime analysis, the BHP versus $\{F_L(t/t_c)\}^2$ plot was used to pinpoint the initial pore pressure and calculate the reservoir transmissibility. The early linear behavior indicates the radial flow regime. The intersection of pressure axial and early linear behavior trend line represents the initial reservoir pore pressure of 5000 psi. The slope of trend line is measured as 3333 psi. The closure time is 2.4 hrs from the before closure analysis. The transmissibility can be obtained as

$$\frac{kh}{\mu} = 2.5\times10^5 \frac{V_i}{t_c}\frac{1}{m_{rf}} = 2.5\times10^5 \frac{100}{2.4\times60}\frac{1}{3333} = 52 md\bullet ft/cp. \qquad (5.11)$$

From fluid properties analysis, the viscosity of the hydrocarbon phase is determined as 0.03 cp. Consequently, the permeability of the reservoir matrix is 0.011 md.

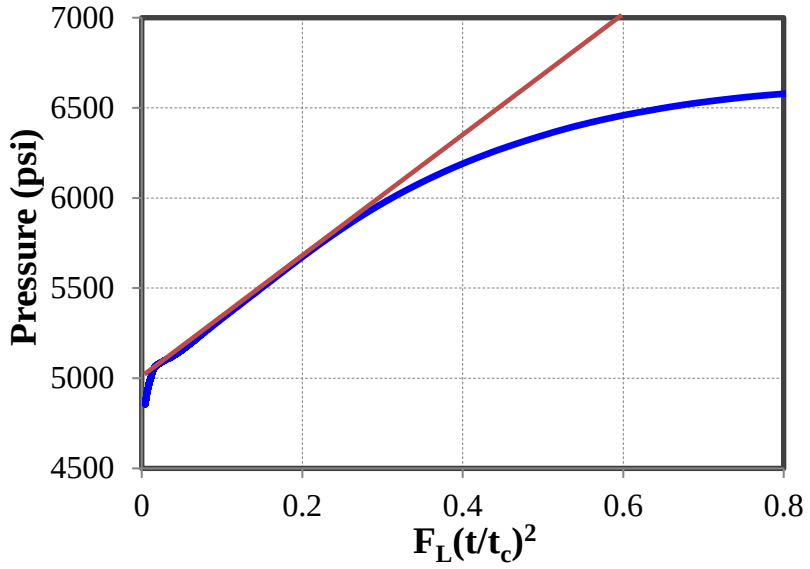

Figure 5.13: Initial pore pressure and reservoir permeability for the Marcellus shale after closure analysis.

To perform the before closure analysis, the fracture propagation model should be first determined. We focus on the pressure behavior during the injection stage as shown in **Fig. 5.14**.

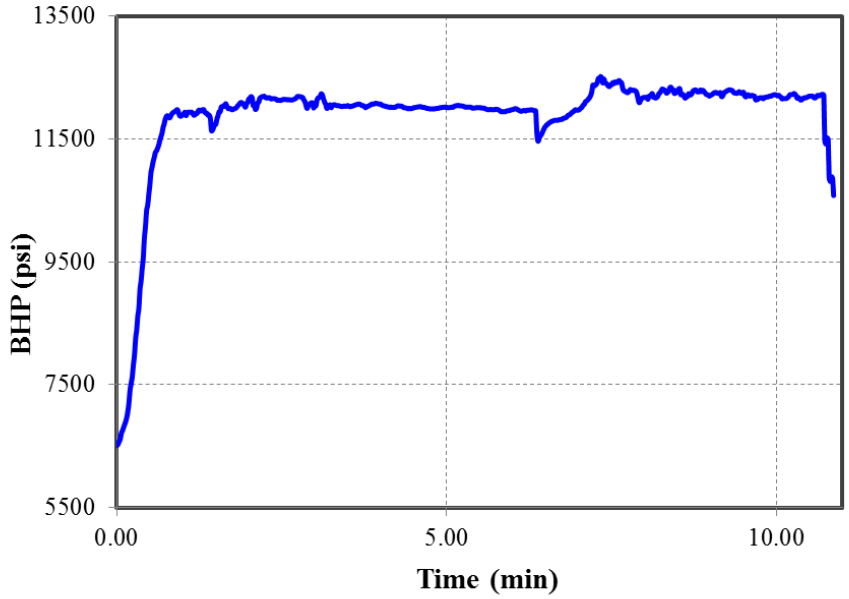

Figure 5.14: Injection stage pressure profile with Cartesian coordinate system.

Subsequently, the log-log plot of injection stage pressure is constructed as shown in **Fig. 5.15**. However, the fracture propagation model is hard to distinguish with the log-log slope method. The early-time pressure increases in a very short time. There is not a stable period for us to diagnose the fracture propagation pattern. The late time flat slope may not necessarily indicate a T shaped fracture since the injection rate is low and injection time is short. Therefore, we need to adopt the volume balance method to identify the fracture propagation model for this case.

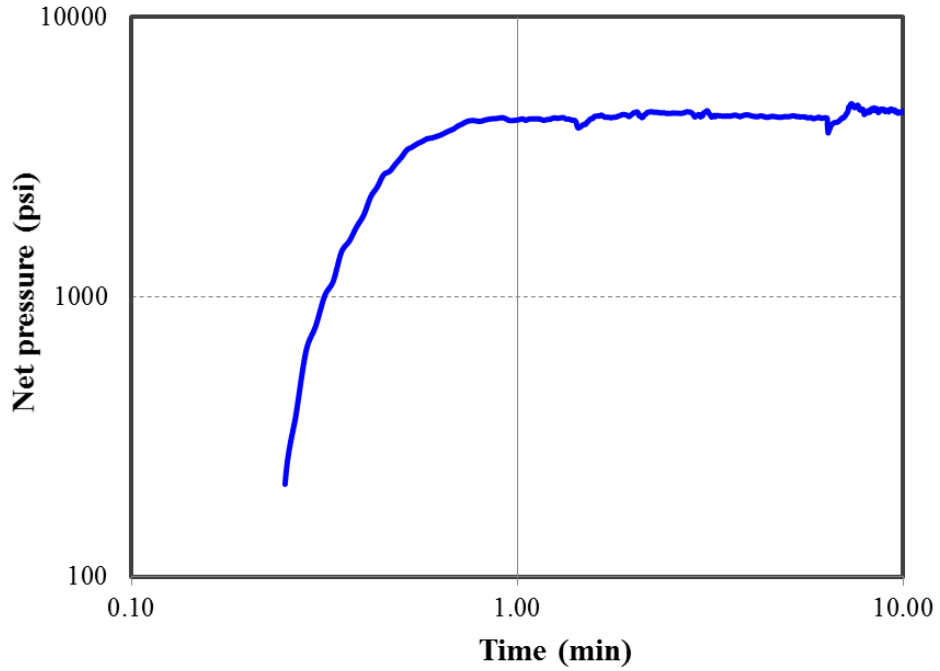

Figure 5.15: Injection stage pressure profile with log-log coordinate system

Eq. 5.2 is employed to detect the fracture propagation pattern. Therefore, shut-in pressure profile with the square root of time was constructed as shown in **Fig. 5.16**. The slope of the pressure linear behavior is around 1000 psi/sqrt(hr). With the slope, the fracture stiffness is calculated as 29348 psi/ft with Eq 5.2. Fracture width is then calculated as 0.052 ft.

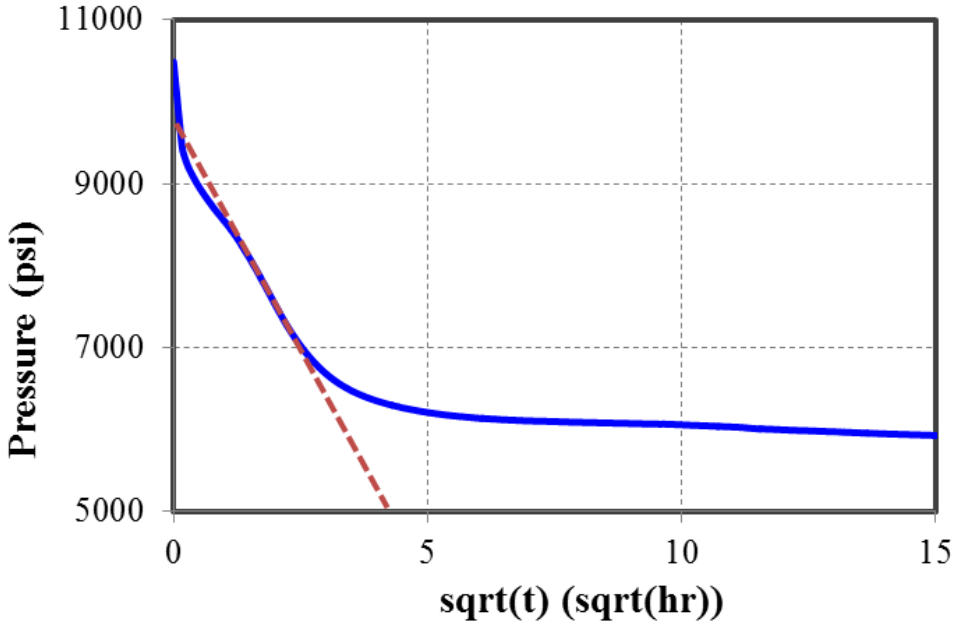

Figure 5.16: Volume balance based fracture propagation model detection.

Using Table 5.3, the volumetric parameter for each fracture propagation model can be calculated as follows:

Fracture Model	Volume
PKN	102 bbl
KGD	80 bbl
Radial	108 bbl

Table 5.4: Volume balance with different fracture propagation model.

The actual injection volume is 100 bbl. It seems that the PKN model is more suitable candidate for the fracture propagation pattern. However, the injection efficiency should be taken into consideration. The common injection efficiency for the shale gas

reservoir is between 70% and 80%. The injection efficiency is related to the fracture propagation pattern. In this case, the KGD model is a more reasonable candidate for the fracture propagation model. The specific injection efficiency will be calculated with KGD model to confirm our assumption.

Subsequently, in order to calculate the injection efficiency and leak-off coefficient, we need to calculate the p^*. p^* for KGD model is the G-function pressure slope at $\frac{P_{net}}{P_{net,si}} = \frac{3}{4}$. In this case, p^* is equal to the slope at 9000 psi as shown in **Fig. 5.17**. The p^* for this case is 180 psi.

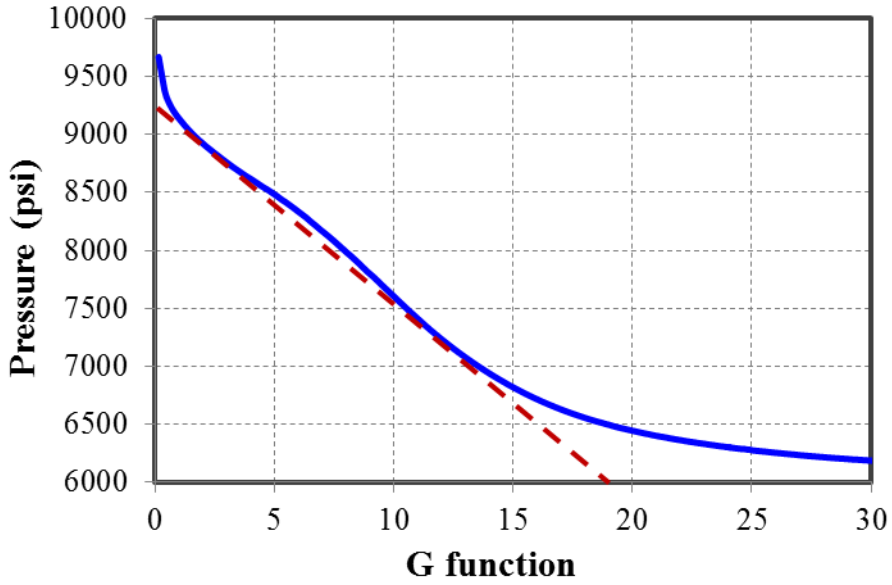

Figure 5.17: p^* calculation with G function time.

The corrected G can be calculated as

$$G^* = \frac{P_{net,si}}{p^*} = \frac{9172 - 8084}{180} = 6. \tag{5.12}$$

The injection efficiency can be obtained with:

$$\eta = \frac{G^*}{2\kappa + G^*} = \frac{6}{2+6} = 75\%. \tag{5.13}$$

The calculated injection efficiency confirms our previous assumption. The actual fracture volume should be around 75 bbl. Consequently, the KGD is the best candidate for this DFIT test. The stiffness calculation and other volume balance calculation parameters are sensitive to the Young's modulus, Poisson's ratio, and fluid properties. The more understanding in these parameters will enhance our confidence in our fracture propagation pattern determination.

Finally, the fluid leak-off coefficient can be obtained with:

$$C_L = \frac{2p^*\beta_s L}{r_p\sqrt{t_p E'}} = \frac{2\times 180\times 1\times 30}{1\times\sqrt{10}\times 3048297} = 1.12\times 10^{-3}\ ft/\min^{0.5}. \tag{5.14}$$

5.4 Summary

- The assumptions and geometry of PKN, KGD, and radial fracture propagation model are introduced. The fracture propagation pattern detection method including log-log plot and volume balance are explained.
- The three different opinions on the closure point selection are illustrated. The holistic method picks the near peak deviation point. McClure's method

picks the early deviation point. Wang's method picks the average between the early and late deviation points.

- The leak-off coefficient and injection efficiency can be calculated with the before closure analysis.
- The three flow regimes, linear, bilinear, and radial flow, are illustrated. $F_L(t/t_c)$ plot is employed to identify the flow regime.
- Initial pore pressure and reservoir matrix permeability can be obtained with after closure analysis.
- A Marcellus shale gas field DFIT data is analyzed to test our workflow.

Chapter 6: Summary, Conclusions, and Recommendations

In this chapter, the summary and conclusions for this work are presented followed by the recommendations for the future work.

6.1 Summary and Conclusions

We now present the summary and conclusions of this research:

1. Many fracture diagnostic technologies including DFIT, DTS, DAS, microseismic, and tracer flow back, have been developed for the unconventional reservoirs. The reasons of growing acceptance of fracture diagnosis lies in the hydraulic fracturing monitoring and parameter characterization for the fracture design and reservoir simulation for the complex fracture network.
2. The downhole temperature and acoustic energy could affect the strain status of the fiber optics. The peak value of Rayleigh, Brillouin, and Raman is related to the strain of the fiber optics. Therefore, the temperature and acoustic energy could be inferred with the signal processing tool.
3. There are three ways to install the downhole fiber optics, namely, temporary, semi-permanent, and permanent installation. The permanent installation DTS data is hard to deal with since thermal coupling effect should be considered in this case.
4. Through the qualitative analysis of filed DTS data, the effectiveness of the staged fracturing is evaluated. The performance of each cluster can be monitored. The coincidence between DTS and DAS data interpretation could strengthen our confidence in the conclusions.
5. A new comprehensive DTS data interpretation model is developed. Our model can handle the reservoir, fracture, and wellbore domain.

6. The reservoir model is an IMPEC compositional model. The wellbore model is a fully implicit model. The governing equation and solution scheme are given.
7. The coupling scheme is iteration based coupling method. For the pressure filed, reservoir and wellbore interacts with each other through flowing bottom pressure, reservoir pressure, and productivity index. Reservoir will provide the ambient temperature and reservoir inflow temperature for the wellbore.
8. Reservoir model was verified with CMG while wellbore model is verified with OLGA.
9. A series of sensitivity analysis were conducted to analyze the impacts of reservoir matrix permeability, fracture conductivity, reservoir rock thermal conductivity, and heat transfer coefficient on the temperature profile along the wellbore.
10. An equal spacing five fracture case is constructed to study the thermal mixing effect. The impact of fracture geometry, fracture properties, and fracture spacing on the temperature profile along the wellbore is analyzed through a complex five fracture case.
11. DFIT data analysis is classified into two major parts, before closure analysis and after closure analysis. The before closure analysis is related to the geomechanics; the after closure analysis is related to the well testing.
12. Three common fracture propagation models, PKN, KGD, and radial model, are introduced. The two methods, log-log plot and volume balance methods, to detect the fracture propagation patterns are illustrated.
13. The three different opinions on the closure point selection are illustrated. The holistic method picks the near peak deviation point. McClure's method picks the early deviation point. Wang's method picks the average between the early and late deviation points.

14. The three flow regimes, linear, bilinear, and radial flow regime, are explained. The $F_L(t/t_c)$ function can be used to identify flow regime.
15. Leak-off coefficient and injection efficiency can be obtained with before closure analysis while initial reservoir pore pressure and reservoir matrix permeability can be obtained with after closure analysis.
16. A Marcellus shale gas DFIT data is analyzed with our workflow. The log-log plot fails to identify the fracture propagation geometry. The volume based method pinpoints the KGD fracture propagation patterns. The leak-off coefficient, injection efficiency, matrix permeability, and initial pore pressure are successfully calculated.

6.2 Recommendations for Future Work

1. Extend our comprehensive model to the injection stage. The simulation of injection stage could obtain the temperature distribution in the reservoir domain. This would provide valuable initial condition for the warm-back stage simulation or production stage simulation.
2. Apply our comprehensive model to the warm-back stage. Usually, the warm-back stage would provide the most valuable information compared to injection stage and production stage since the temperature change is more obvious compared to other two stages.
3. Implement the thermal embedded discrete fracture model (EDFM) to capture the complex fracture geometry. The impact of complexity of the fracture network on the temperature profiling along the wellbore could be analyzed.

4. Construct a history matching tool for the post DTS data interpretation. Through the inverse problem, the key fracture design parameters such as fracture conductivity and reservoir matrix permeability can be obtained.
5. The inverse problem can be further extended to more complex situations. We could employ the forward model with thermal EDFM to obtain the complexity of the fracture network with history matching tool.
6. Estimate fracturing fluid lateral expansion or stimulated reservoir volume. Since the later travelling distance of fracturing fluid along the casing direction could affect the temperature along the wellbore, the SRV may be obtained through the history matching.
7. Develop a DAS signal processing and visualization tool. The successful visualization of DAS data could provide valuable information for the DTS data interpretation such as the initial guess or parameter constrains for the inverse problem.
8. Simplify the current model and construct a real-time history matching tool.
9. Develop a semi-analytical model for the DFIT after closure analysis, which may enable the analysis of the impacts of fracture geometry and natural fracture connection on the DFIT pressure transient behavior.
10. Integrate different fracture diagnostic tools to obtain a more optimal solution.

Nomenclature

t	Time
W_i	Accumulation term
$\vec{F}_i$	Flux term
R_i	Source term
ϕ	Porosity
V_b	Bulk volume
V_t	Total volume
V_p	Pore volume
N_p	Number of phases
S	Fluid phase saturation
ξ	Molar density
x	Mole fraction of component in phase
$\vec{u}$	Phase velocity
$\vec{\vec{k}}$	Permeability tensor
k_r	Relative permeability
μ	Phase viscosity
D	Depth
γ	Specific gravity
p	Pressure
p_{cj}	Capillary pressure between phase j and reference phase.
q	Molar injection or production rate
N_c	Number of hydrocarbon components
V_P^0	Pore volume at reference pressure
c_f	Formation compressibility
$\vec{V}_t$	Partial molar volume
w_f	Fracture aperture
k_f	Fracture permeability
L	Length of the fracture segment

$\dot{\Psi}_{ik}$	Molar influxes of component k in oil and gas phases
C_0	Profile parameter in drift flux model
$\overline{h}_i$	Enthalpy of phase i per unit mass
$\overline{H}_i$	Phase i enthalpy influxes per unit well grid block volume
C_{pj}	Heat capacity of phase j
η_j	Joule Thompson coefficient of phase j
U^T	Sum of internal energy of rock and total fluid per bulk volume
λ^T	Effective conductive coefficient
h_j	Phase molar enthalpy
ζ_j	Phase fluid density
ζ_r	Rock density
u_j	Internal energy of phase j
u_r	Internal energy of the rock
$\dot{Q}_L$	Heat loss
q_H	Enthalpy of the injection fluid
α_o	Volume fractions of oil
α_g	Volume fractions of gas
α_w	Volume fractions of water
u_{sg}	Superficial velocity for gas
D	Wellbore diameter
J	Volumetric average velocity of the bulk
V_d	Drift velocity
C_0	Drift flux profile parameter
u_m	Mixture average velocity
$\overline{h}_o$	Oil enthalpies per unit mass
$\overline{h}_g$	Gas enthalpies per unit mass
$\overline{h}_w$	Water enthalpies per unit mass
S	Entropy
$\dot{H}_o$	Oil enthalpy influxes per unit well grid block volume
$\dot{H}_g$	Gas enthalpy influxes per unit well grid block volume

$\dot{H}_w$	Water enthalpy influxes per unit well grid block volume
C_{pj}	Heat Capacity
η_j	Joule Thomson coefficient
$\dot{\Psi}_{ok}$	Molar influxes of component k in oil phase
$\dot{\Psi}_{gk}$	Molar influxes of component k in gas phase
Γ_g	Interphase mass transfer term between oil and gas
$\dot{\Psi}_o$	Mass influx terms of oil
$\dot{\Psi}_g$	Mass influx terms of gas
$\dot{\Psi}_w$	Mass influx terms of water
p_f	Fracture pressure
Δt_D	Dimensionless time for DFIT
t_p	Total pumping time
S_f	Fracture stiffness
r_p	Ratio of the permeable fracture surface area to total fracture surface area
C_L	Leak-off coefficient
G	G time function
g	g time function
η	Injection efficiency
β_s	Average net pressure in the fracture to net pressure at the wellbore at the end of the pumping.
κ	Spurt loss
$F_L(t/t_c)$	Linear time function
m_{lf}	Slope of linear after closure analysis plot
m_{rf}	Slope of radial after closure analysis plot
f_{aL}	Apparent fracture half length
L	Fracture length
P_0	Net pressure at ISIP
μ_f	Fluid viscosity

SI Metric Conversion Factors

ft × 3.048 e-01 = m

ft^3	×	2.832	e-02	=	m^3
cp	×	1.0	e-03	=	Pa·s
psi	×	6.895	e+00	=	kPa
md	×	1e-15	e+00	=	m^2

Subscript

p	Phase
j	Index of fluid phases
i	Index of fluid component
R_i	Source term
ϕ	Porosity
V_b	Bulk volume
N_p	Number of phases

Acronyms

DTS	Distributed Temperature Sensing
DAS	Distributed Acoustic Sensing
DSS	Distributed Strain Sensing
DFIT	Diagnostic Fracture Injection Test
SAGD	Steam Assisted Gravity Drainage
EOS	Equation of State
IMPEC	Implicit Pressure and Explicit Compositions
JT	Joule Thomson Effect
ISIP	Instantaneous shut-in pressure

References

Barree, R. D. 1998. Applications of Pre-Frac Injection/ Falloff Tests in Fissured Reservoir-Field Examples. Presented at SPE Rocky Mountain Regional/Low Permeability Reservoirs Symposium, Denver, Colorado, 5-8 April. SPE-39932-MS.

Barree, R. D. and Mukherjee, H. 1996. Determination of Pressure Dependent Leakoff and Its Effect on Fracture Geometry. Presented at SPE Annual Technical Conference and Exhibition, Denver, Colorado, 6-9 October, Denver, Colorado. SPE-36424-MS.

Barree, R. D., Barree, V. L., and Craig, D. P. 2007. Holistic Fracture Diagnostics. Presented at Rocky Mountain Oil & Gas Technology Symposium, Denver, Colorado, 16-18 April. SPE-107877-MS.

Barree, R. D., Barree, V. L., and Craig, D. P. 2009. Holistic Fracture Diagnostics: Consistent Interpretation of Prefrac Injection Tests Using Multiple Analysis Methods. *SPE Production & Operations* **24** (3). SPE-107877-PA.

Barree, R. D., Barree, V. L., and Craig, D. P. 2015. Diagnostic Fracture Injection Tests: Common Mistakes, Misfires, and Misdiagnoses. *SPE Production & Operations* **30** (2). SPE-169539-PA.

Bendiksen, K. H., Maines, D., Moe, R., and Nuland, S. 1991. The Dynamic Two-Fluid Model OLGA: Theory and Application. *SPE Production Engineering* **6** (2). SPE-19451-PA.

Bhatnagar, A. 2016. Overcoming Challenges in Fracture Stimulation through Advanced Fracture Diagnostics. Presented at SPE Asia Pacific Hydraulic Fracturing Conference, Beijing, China, 24-26 August. SPE-181802-MS.

Birkholzer J., and Karasaki K. 1996. FMGN, RENUMN, POLY, TRIPOLY: Suite of Programs for Calculating and Analyzing Flow and Transport in Fracture Networks Embedded in Porous Matrix Blocks, Lawrence Berkeley National Laboratory, Berkeley, CA.

Bunger, A. P., McLennan, J., and Jeffrey, R. 2013. *Effective and Sustainable Hydraulic Fracturing*. InTech. ISBN 978-953-51-1137-5.

Cannon, R. T. and Aminzadeh, F. 2013. Distributed Acoustic Sensing: State of the Art. Prsented at SPE Digital Energy Conference, The Woodlands, Texas, 5-7 March. SPE-163688-MA.

Carter, R.D. 1957.Derivation of the General Equation for Estimating the Extent of the Fractured Area," Appendix I of "Optimum Fluid Characteristics for Fracture Extension, Drilling and Production Practice, G.C. Howard and C.R. Fast, New York, New York, USA, American Petroleum Institute, 261–269.

Chang, Y. 1990. Development and Application of An Equation of State Compositional Simulator, Dissertation, The University of Texas at Austin.

Chen, Y., Ramos, R. T., Hartog, A. H., Greenaway, R., Powell, G., and Taylor, D. 2008. Accurate Single-Ended Distributed Temperature Sensing. Presented at SPE Annual Technical Conference and Exhibition, Denver, Colorado, 21-24 September. SPE-116655-MS.

Cinco-Ley, H., and Samaniego, F. 1981. Transient Pressure Analysis for Fractured Wells. *Journal of Petroleum* Technology. SPE-7490-PA.

Cipolla, C. L., Mack, M. G. Maxwell, S. C., and Downie, R. C. 2011. A Practical Guide to Interpreting Microseismic Measurements. Presented at North American Unconventional Gas Conference and Exhibition, The Woodlands, Texas, 14-16 June. SPE-144067-MS.

Cipolla, C.L., Fitzpatrick, T., Williams, M.J. et al. 2011. Seismic-to-Simulation for Unconventional Reservoir Development. Presented at the SPE Reservoir Characterization and Simulation Conference and Exhibition, Abu Dhabi, 9–11 October. SPE-146876-MS.

Cipolla, C.L., Lolon, E.P., Erdle, J.C. et al. 2010. Reservoir Modeling in Shale-Gas Reservoirs. SPE Res Eval & Eng 13 (4): 638-653. SPE-125530-PA.

Cotte, F. P., Doughty C., and Birkholzer, J. 2010. Modeling Single Well Injection-withdrawal (SWIW) Tests for Characterization of Complex Fracture-matrix Systems. Lawrence Berkeley National Laboratory, Berkeley, CA.

Craig, D. 2014. New Type Curve Analysis Removes Limitations of Conventional After-Closure Analysis of DFIT Data. Presented at SPE Unconventional Resource Conference, The Woodlands, Texas 1-3 April. SPE-168988-MS.

Cramer, D. D. and Nguyen, D. H. 2013. Diagnostic Fracture Injection Testing Tactics in Unconventional Reservoirs. Presented at SPE Hydraulic Fracturing Technology Conference, The Woodland, Texas, 4-6 February. SPE-163863-MS.

Cui, J., Zhu, D., and Jin, M. 2016. Diagnosis of Production Performance After Multistage Fracture Stimulation in Horizontal Wells by Downhole Temperature Measurements. *SPE Production & Operations* **31** (4). SPE-170874-PA.

Darabi, H. 2014. Development of a Non-Isothermal Compositional Reservoir Simulator to Model Asphaltene Precipitation, Flocculation, and Deposition and Remediation, Dissertation, The University of Texas at Austin.

Denney, D. 2012. Interpreting Microseismic Measurements: Practical Guide. *Journal of Petroleum Technology* **64** (3). SPE-0312-0105-JPT.

Denniel, S., Perrin, J. and Henry, A. F. 2004. Review of Flow Assurance Solution for Deepwater Fields. Presented at Offshore Technology Conference, Houston, Texas, 3-6 May. OTC-16686-MS.

Dickenson, P., Brants-Menard, S., Telsey, M., Stanbridge, A., Wilson, C., Akin, J., Roman, N., Anifowoshe, W., Yates, M., Carney, B. J., Costello, I., Hewitt, J., and Warner, R. 2016. Real-Time Interactive Remote Display of DTS and DAS Data for Well Treatment Optimization. Presented at SPE Intelligent Energy International Conference and Exhibition, Aberdeen, Scotland, 6-8 September. SPE-181065-MS.

Economides, M. J., and Nolte, K. G. 1989. *Reservoir Stimulation*. Prentice Hall.

Edmister, W. C. and Lee, B. I. 1984. *Applied Hydrocarbon Thermodynamics*. Vol. 1 (2nd ed.). Gulf Publishing. ISBN 0-87201-855-5.

Far, M.E., Sayers, C.M., Thomsen, L. et al. 2013. Seismic Characterization of Naturally Fractured Reservoirs Using Amplitude versus Offset and Azimuth Analysis. *Geophysical Prospecting* **61** (2): 427–47.

Fisher, M.K., Heinze, J.R., Harris, C.D. et al. 2004. Optimizing Horizontal Completion Techniques in the Barnett Shale Using Microseismic Fracture Mapping. Presented at the SPE Annual Technical Conference and Exhibition, Houston, Texas, 26-29 September. SPE-90051-MS.

Foo, D. B., Krislock, J., Meador, T. J., and Cheng, T. 2014. Horizontal Well Injection Profiling Using Distributed Temperature Sensing. Presented at SPE/CSUR Unconventional Resources Conference, Calgary, Alberta, Canada, 30 September–2 October. SPE-171586-MS.

GEM, CMG: Version 2011 *User's Guide*. Computer Modeling Group Ltd., Calgary, Alberta, Canada.

Ghergut, M. I., Behrens, M. H., Sauter, M. M. 2014. Tracer-based Quantification of Individual Frac Discharge in Single-well Multiple-frac Backflow: Sensitivity Study. *Energy Procedia* **59** 235-242.

Grayson, S., Gonzalez, Y., England, K., Bidyk, R. and Pitts, S. F. 2015. Monitoring Acid Stimulation Treatments in Naturally Fractured Reservoirs with Slickline Distributed Temperature Sensing. Presented at SPE/ICo TA Coiled Tubing & Well Intervention Conference & Exhibition, The Woodlands, Texas, 24-25, March. SPE-173640-MS.

Hajibeygi, H., Karvounis, D. and Jenny, P. 2011. A Hierarchical Fracture Model for the Iterative Multiscale Finite Volume Method. *J. Comput.Phys*. **230** (24): 8729-8743.

Haustveit, K. Dahlgren, K., Greenwood, H., Peryam, T., Kennedy, B., and Dawson, M. 2017. New Age Fracture Mapping Diagnostic Tools- A STACK Case Study. Presented at SPE Hydraulic Fracturing Technology Conference and Exhibition, The Woodlands, Texas, 24-26 January, SPE-184862-MS.

Holley, E. H., Molenaar, M. M., Fidan, E., and Banack, B. 2013. Interpreting Uncemented Multistage Hydraulic-Fracturing Completion Effectiveness by Use of Fiber-Optic DTS Injection Data. *SPE Drilling & Completion* **28** (3). SPE-153131-PA.

Holley, E. H., Zimmer, U., Mayerhofer, M. J., and Samson, E. 2010. Integrated Analysis Combining Microseismic Mapping and Fiber Optic Distributed Temperature Sensing (DTS). Presented at Canadian Unconventional Resources and International Petroleum Conference, Calgary, Alberta, Canada, 19-21 October. SPE-136565-MS.

Hoteit, H. and Firoozabadi, A. 2006. Compositional Modeling of Discrete-Fractured Media Without Transfer Functions by the Discontinuous Galerkin and Mixed Methods. *SPE J.* **11** (3): 341-352. SPE-90277-PA.

Hui, M.-H., Mallison, B. T., Fyrozjaee, M. H. et al. 2013. The Upscaling of Discrete Fracture Models for Faster, Coarse-Scale Simulations of IOR and EOR Processes for Fractured Reservoirs. Presented at the SPE Annual Technical Conference and Exhibition New Orleans, Louisiana, 30 September-2 October. SPE-166075-MS.

Ishii M. 2005. One-Dimensional Drift-flux Model and Constitutive Equations for Relative Motion between Phases in Various Two-Phase Regimes," *International Journal of Heat and Mass Transfer* **48** (6): 1222-1223.

Karimi-Fard, M. and Firoozabadi, A. 2003. Numerical Simulation of Water Injection in Fractured Media using the Discrete-Fractured Model and theGalerkin Method. *SPE Res Eval & Eng* **6** (2): 117-126. SPE-83633-PA.

Khristianovich, S.A. and Zheltov, Y.P. 1955. Formation of Vertical Fractures by Means of Highly Viscous Liquid. *Proc., Fourth World Pet. Congress*, Rome **2**, 579–586.

Khristianovich, S.A., Zheltov, Y.P., Barenblatt, G.I. and Maximovich, G.K. 1959. Theoretical Principles of Hydraulic Fracturing of Oil Strata, *Proc., Fifth World Petroleum Congress*, New York.

Kumar, A., Singh, A. P., and Samuel, R. 2012. Field Application of an Analytical Model for Estimating the Downhole Temperatures due to Wellbore Friction. Presented at IADC/SPE Asia Pacific Drilling Technology Conference and Exhibition, Tianjin, China, 9-11 July. SPE-156307-MS.

Lamei, H., and Soliman, M. Y. 2014. New Before Closure Analysis Model for Unconventional Reservoirs. Presented at SPE/EAGE European Unconventional Resources Conference and Exhibition, Vienna, Austria, 25-27 February. SPE-167790-MS.

Lee, S.H., Lough, M.F. and Jensen, C.L. 2001. Hierarchical Modeling of Flow in Naturally Fractured Formations with Multiple Length Scales. *Water Resour. Res.* **37** (3): 443–455.

Li, L. and Lee, S.H. 2008. Efficient Field-Scale Simulation of Black Oil in a Naturally Fractured Reservoir Through Discrete Fracture Networks and Homogenized Media. SPE *Res Eval & Eng* **11** (4): 750–758. SPE-103901-PA.

Li, L., Jiang, H., Li, J., Wu, K., Meng, F., and Chen, Z. 2017. Modeling Tracer Flowback in Tight Oil Reservoirs with Complex Fracture Networks. *Journal of Petroleum Science and Engineering* **157**.

Liu, S. Valko, P. P., Mcketta, S., and Liu, X. 2016. Micoseismic Closure Window Better Characterizes Hydraulic Fracture Geometry. Presented at SPE Hydraulic Fracturing Technology Conference, The Woodlands, Texas, 9-11 February. SPE-179116-MS.

Lohrenz, J., Bray, B. G., and Clark, C. R. 1964. Calculating Viscosities of Reservoir Fluids from Their Compositions. *Journal of Petroleum Technology* **16** (10): 1171-1176. SPE-915-PA.

Martinez, R., Hill, A. D, and Zhu, D. 2014. Diagnosis of Fracture Flow Conditions with Acoustic Sensing. Presented at SPE Hydraulic Fracturing Technology Conference, The Woodlands, Texas, 4-6 February. SPE-168601-MS.

Martinez, R., Hill, A. D., and Zhu, D. 2014. Diagnosis of Fracture Flow Conditions with Acoustic Sensing. Presented at SPE Hydraulic Fracturing Technology Conference, The Woodlands, 4-6 February. SPE-168601-MS.

Maxwell, S. C., Cho, D. Pope, T. L., Jones, M., Cipolla, C. L. Mack, M. G., Henery, F., Norton, M. and Leonard, J. A. 2011, Presented at SPE Hydraulic Fracturing Technology Conference, The Woodlands, Texas, 24-26 January. SPE-140449-MS.

Maxwell, S. C., Urbancic, T. I., Steinsberger, N., & Zinno et al. 2002. Microseismic Imaging of Hydraulic Fracture Complexity in the Barnett Shale. Presented at the SPE Annual Technical Conference and Exhibition, San Antonio, Texas, 29 September-2 October. SPE-77440-MS.

McClure, M., Blyton, C., Jung, H., and Sharma, M. 2014. The Effect of Changing Fracture Compliance on Pressure Transient Behavior during Diagnostic Fracture Injection Tests. Presented at SPE Annual Technical Conference and Exhibition, Amsterdam, The Netherlands, 27-29 October. SPE-170956-MS.

Medina, E., Sierra, J., Garcia, A., Gleaves, J., and Mendez, J. 2015. Optim 173686ization of Matrix Acidizing with Fluids Diversion in Real-Time Using Distributed Temperature Sensing and Coiled Tubing. Presented at SPE/ICoTA Coiled Tubing & Well Intervention Conference & Exhibition, The Woodlands, Texas, 24-25 March. SPE-173686-MS.

Mehra, R. K., Heidemann, R. A., and Aziz, K. 1983. An Accelerated Successive Substitution Algorithm. The Canadian Journal of Chemical Engineering **61** (4): 590-596.

Molenaar, M. M., Hill, D., Webster, P., Fidan, E., and Birch, B. 2012. First Downhole Application of Distributed Acoustic Sensing for Hydraulic Fracturing Monitoring and Diagnostics. SPE *Drilling & Completion* **27** (01). SPE-140561-PA.

Nelson, R. A. 1985. Geologic Analysis of Naturally Fractured Reservoirs. Gulf Publishing Company.

Nolte, K. G. 1979. Determination of Fracture Parameters from Fracturing Pressure Decline. Presented at SPE Annual Technical Conference and Exhibition, Las Vegas, Nevada, 23-26 September. SPE-8341-MS.

Nolte, K. G., 1986. A General Analysis of Fracturing Pressure Decline with Application to Three Models. *SPE Formation Evaluation*, **1** (06). SPE-12941-PA.

Nolte, K. G., Maniere, J. L, Owens, K. A. 1997. After-closure Analysis of Fracture Calibration Tests. Presented at SPE Annual Technical Conference and Exhibition, San Antonio, Texas, 5-8 October. SPE-38676-MS.

Nordgren, R. P. 1972. Propagation of a Vertical Hydraulic Fracture. *SPE J.* **12** (04). SPE-3009-PA.

Peng, D. Y., and Robinson, D. B. 1976. A New Two-Constant Equation of State. Industrial and Engineering Chemistry Fundamentals **15**: 59-64.

Perkins, T. K. and Kern, L. R. 1961. Width of Hydraulic Fracture. *Journal of Petroleum Technology* **13** (09). SPE-89-PA.

Perkins, T. K., & Kern, L. R. (1961, September 1). Widths of Hydraulic Fractures. Society of Petroleum Engineers. doi:10.2118/89-PA.

Perry, R. H., and Green, D. W. 1984. Perry's Chemical Engineers' Handbook. McGraw-Hill. ISBN 0-07-049479-7.

Perschke, D. R., Chang, Y., Pope, G. A., and Sepehrnoori, K. 1989. Comparison of Phase Behavior Algorithms For An Equation-Of-State Compositional Simulator. SPE-19443-MS.

Pinnacle Fiber Optics Sensing Technology Brochure 2012. http://www.halliburton.com/public/pinnacle/contents/Brochures/web/fiber-optics.pdf.

RELAP5-3D. 2012. Code Manual Volume IV: Models and Correlations". INEEL-EXT-98-00834, Revision 4.0.

Roy, B. N. 2002. *Fundamentals of Classical and Statistical Thermodynamics*. John Wiley & Sons. ISBN 0-470-84313-6.

Sakiyama, N., Fujii, K., Pimenov, V., Parshin, A., Yamamoto, K., and Wright, J. F. 2013. Fluid-Level Monitoring Using a Distributed Temperature Sensing System During a Methane Hydrate Production Test. Presented at International Petroleum Technology Conference, Beijing, China,26-28 March. IPTC-16769-MS.

Shirdel, M., 2013. Development of a Coupled Wellbore-Reservoir Compositional Simulator for Damage Prediction and Remediation, Dissertation, The University of Texas at Austin.

Shoham, O. 2005. Mechanistic Modelling of Gas-Liquid Two-Phase Flow in Pipes. Society of Petroleum Engineering.

Soliman, M. Y. 1986, Technique for Considering Fluid Compressibility and Temperature Changes in Mini-Frac Analysis. Presented at SPE Annual Technical Conference and Exhibition, New Orleans, Louisiana, 5-8 October. SPE-15370-MS.

Soliman, M. Y., Craig, D. P., Bartko, K. M., Rahim, Z., Adams, D. M. 2005. Post-closure Analysis to Determine Formation Permeability, Reservoir Pressure, Residual Fracture Properties. Presented at SPE Middle East Oil and Gas Show and Conference, Kingdom of Bahrain, 12-15 March. SPE-93419-MS.

Soliman, M. Y., Poulsen, D. K. and Kuhlman, R. D. 1990. General Minifrac Analysis for Heterogeneous Formation Including Spurt Loss. Presented at SPE Annual Technical Conference and Exhibition, New Orleans, Louisiana, 23-26 September.SPE-20705-MS.

Sookprasong, P.A., Hurt, R. S., and Gill, C. C. 2014. Downhole Monitoring of Multicluster, Multistage Horizontal Well Fracturing with Fiber Optic Distributed Acoustic Sensing (DAS) and Distributed Temperature Sensing (DTS). Presented at International Petroleum Technology Conference, Kuala Lumpur, Malaysia, 10-12 December. IPTC-17972-MS.

Talebi, S., Young, R. P., Vandamme, L., and McGaughey, W. J. 1991. Presented at The 32nd U.S. Symposium on Rock Mechanics, Norman, Oklahoma, 10-12 July. ARMA-91-461.

Tsang, C. F. 2010. Insight from Simulations of Single-well Injection-withdrawal Tracer Tests on Simple and Complex Fractures. Lawrence Berkeley National Laboratory, Berkeley, CA.

U.S. Energy Information Administration. 2012. Global Shale Gas Basins. http://blog. thomsonreuters.com/index.php/global-shale-gas-basins-graphic-of-the-day.

U.S. Energy Information Administration. 2013a. Technically Recoverable Shale Oil and Shale Gas Resources: An Assessment of 137 Shale formations in 41 Countries outside the United States. http://www.eia.gov/analysis/studies/worldshalegas/.

U.S. Energy Information Administration. 2017. Natural Gas Explained. https://www.eia.gov/energyexplained/index.cfm?page=natural_gas_where.

Wang, H., and Sharma, M. M. 2017. New Variable Compliance Method for Estimating In-Situ Stress and Leak-off from DFIT Data. Presented at SPE Annual Technical Conference and Exhibition, San Antonio, Texas, 9-11 October. SPE-187348-MS.

Wang, X., and Bussear, T. R. 2011. Real Time Horizontal Well Monitoring Using Distributed Temperature Sensing (DTS) Technology. Presented at OTC Brasil, Rio de Janeiro, Brazil, 4-6 October. SPE-22293-MS.

Wang, Z., 2012. The Uses of Distributed Temperature Survey (DTS) Data, Dissertation, Stanford University.

Xu, Y., Fiho, J.S, Yu, W., and Sepehrnoori, K. 2017. Discrete-Fracture Modelling of Complex Hydraulic-Fracture Geometries in Reservoir Simulators. SPE Reservoir Evaluation & Engineering. SPE-183647-PA.

Xu, Y., Yu, W., and Sepehrnoori, K. 2017. Modeling Dynamic Behavior of Complex Fractures in Conventional Reservoir Simulator. Presented at SPE/AAPG/SEG Unconventional Resources Technology Conference, Austin, Texas, 24-26 July. URTEC-2670513-MS.

Yu, W., Xu, Y., Weijermars, R., Wu, K., and Sepehrnoori, K. 2017. Impact of Well Interference on Shale Oil Production Performance: A Numerical Model for Analyzing Pressure Response of Fracture Hits with Complex Geometries. Presented at SPE Hydraulic Fracturing Technology Conference and Exhibition, The Woodlands, Texas, 24-26 January. SPE-184825-MS.

Zaini, F. and Keough, D. 2017. Downhole Remote Monitoring System for SAGD Observation Wells through Fiber Optic DTS. Presented at SPE Canada Heavy Oil Technical Conference, Calgary, Alberta, Canada, 15-16 February. SPE-185006-MS.

Zemansky, M. W. 1968. Heat and Thermodynamics. McGraw-Hill Higher Education.

Zeng, L., Ke, S, and Liu, Y. 2010. Fracture Research Method in Low Permeability Reservoir. Petroleum Industry Press.